

**School of Chemical and Petroleum Engineering
Department of Chemical Engineering**

**Investigation of Microstructural and Carbon Deposition Effects in
SOFC Anodes Through Modelling and Experiments**

Shambhu Singh Rathore


**This thesis is presented for the Degree of
Doctor of Philosophy
of
Curtin University**

December 2017

Declaration

To the best of my knowledge and belief this thesis contains no material previously published by any other person except where due acknowledgement has been made.

This thesis contains no material which has been accepted for the award of any other degree or diploma in any university.

Signature: 

Date: 18-12-2017

Acknowledgements

First, I would like to thank Curtin University for giving me the opportunity of undertaking my PhD. I want to express my deepest gratitude to my supervisors, Prof. Moses O. Tade, Prof. Zongping Shao and Dr. Periasamy Vijay for their advice, encouragement, support and insight throughout this research thesis. I gratefully acknowledge the Department of Chemical Engineering, Curtin University for providing scholarship during my PhD. I would also like to thank our Head of School, Prof. Vishnu Pareek and the Head of Department, Prof. Hongwei Wu for their support and providing the facilities during my PhD.

I would like to express my thanks to Prof. Meng Ni and his research group for their support and insightful discussions during my research attachment program at Hong Kong Polytechnic University.

I am heartily thankful to Dr. Milin Shah for his insightful suggestions and support for my research work using CFD simulation studies. I would also like to express my sincere thanks to Dr. Andrew Squelch from Western Australia School of Mines for his suggestions and comments on image analysis techniques. I would like to extend my thanks to the staff of John de Laeter Center for their help in the microscopic imaging. I am grateful to Dr. Wei Wang, Dr. Chao Su and Yu Liu for their astute observation and critical comments on the experimental work. I would also like to extend my thanks to research colleagues Paulo Sérgio Barros Julião, Xiaomin Xu, Liupeng, and Yijun Zhong.

I would also appreciate the technical staff of Chemical Engineering for their kind administrative and technical assistance to carry out my laboratory work. I am grateful to Jason Wright, Anja Werner, Roshanak Doroushi, Ann Carroll, Tammy Atkins, Surudee Bunpitakgate, Lemlem Selemon and Randall Ng for their support.

I am very fortunate to have the company of my friends around me. I would like to thank Dr. Yogesh Shinde, Vaibhav Agrawal and Deepak Dwivedi for their constant support and sharing their knowledge about various concepts through this journey. I would like to express my special thanks to Dr. Mamta Pareek and Mihir Pareek, who

have never let me miss my home back in India and always being a source of love and encouragement. I again say thanks to all those who have shared this journey with me.

Finally, I would like to express my gratitude to my grandparents and my parents who have worked so hard to help me achieve my goals. Their support in all my endeavours, their encouragement to pursue my dreams, and their endless love and care has always given me strength and belief.

I dedicate this thesis to all of my family members for their help, support, encouragement and patience during the years of my study.

Abstract

Solid Oxide Fuel Cells (SOFCs) are considered as one of the most promising technologies for the energy conversion because of their high efficiency, fuel flexibility and environmental friendliness. However, this technology still faces many challenges for commercialisation due to performance degradation and structural degradation of the SOFC components. SOFC electrodes should be optimised for the gaseous species transport, electron and ion transport, and chemical and electrochemical active sites. This necessitates the microstructural investigations to study the effects of controllable microstructural parameters (volume fraction, particle size, size ratio and porosity) on the electrode properties and performance. In this thesis, propose improved current image segmentation methods to extract quantitative information from electrode specimen images. In the Ni-YSZ (Nickel-Yttria Stabilised Zirconia) anode, the nickel particle size effect on the anode microstructure and microstructural properties have been investigated.

Microstructural properties are also estimated using analytical modelling approach based on percolation theory. This microstructure model is extended to consider the effect of anode degradation phenomena such as nickel coarsening and carbon poisoning on the microstructural properties. This model provides the insights for the microstructural parameters that should be used for optimising microstructural properties and degradation tolerance.

Finally, Computational Fluid Dynamics (CFD) studies have been performed for multicomponent mass transport in the anode microstructure. All possible dominant chemical reactions in the anode and electrochemical reactions are considered in the model to investigate the effect of anode microstructural parameters (such as anode porosity, gas-solid interface area) on the species transport and carbon deposition. With the increasing advancement of micro and nano-fabrication techniques for electrodes, such microstructural investigation will guide us in micro-engineering the SOFC electrodes for obtaining better mass, electron and ion transport and higher volume densities of active sites for the chemical and electrochemical reactions.

Publications from this Thesis

Peer reviewed journals

Shambhu Singh Rathore, Deepak Dwivedi, Periasamy Vijay, Moses O. Tadé, Zongping Shao (2017). Microstructural investigation in Solid Oxide Fuel Cell Electrodes - a review. *Journal of Power Sources* (to be submitted, January 2018).

Shambhu Singh Rathore, Periasamy Vijay, Moses O. Tadé, Zongping Shao (2017). Microstructural characterisation of Ni-YSZ SOFC anode. *Fuel Cells* (to be submitted, March 2018).

Table of contents

Acknowledgements		i
Abstract		iii
Publications		iv
Nomenclature		ix
List of Figures		xv
List of Tables		xix
Chapter-1	Introduction	1
	1.1 Background and motivation	1
	1.2 Contributions of the Thesis	4
	1.3 Thesis structure	4
Chapter-2	Literature review	7
	2.1 Microstructural investigation in Solid Oxide Fuel Cell electrode	7
	2.1.1 Introduction	7
	2.1.2 Microstructural modelling using analytical methods	10
	2.1.3 Microstructural modelling using numerical methods	17
	2.1.4 Microstructural investigation from 2D images	23
	2.1.4.1 Image analysis and stereology	23
	2.1.4.2 3D reconstruction of electrode from 2D images	28
	2.1.5 Experimental 3D reconstruction of electrodes	30
	2.1.5.1 3D reconstruction using FIB-SEM	31

	2.1.5.2	3D reconstruction using x-ray tomography	40
	2.1.6	Future outlook and conclusions	43
2.2		Carbon poisoning in SOFC anode	44
2.3		Anode performance modelling	49
Chapter-3		Microstructural characterisation of Ni-YSZ anode	51
3.1		Introduction	51
3.2		Experimental methods	53
	3.2.1	Anode substrate preparation	53
	3.2.2	Imaging specimen preparation	55
	3.2.3	Imaging of anode specimen	55
3.3		Quantitative analysis	59
	3.3.1	Image segmentation	59
	3.3.2	Image analysis and stereology	63
		3.3.2.1 Volume fraction	64
		3.3.2.2 Surface area	64
		3.3.2.3 Triple phase boundary	65
		3.3.2.4 Particle size	65
3.4		Results and discussion	68
3.5		Conclusions	76
Chapter-4		Anode microstructural modelling considering structural degradation	77
4.1		Introduction	77
4.2		Model development	78
	4.2.1	Microstructural modelling	78

4.2.2	Microstructural modelling with structural degradation	81
4.2.2.1	Microstructural modelling with nickel coarsening	81
4.2.2.2	Microstructural modelling with carbon poisoning	84
4.3	Results and discussion	87
4.3.1	Anode microstructural properties	87
4.3.2	Anode microstructural properties with nickel coarsening	89
4.3.3	Anode microstructural properties with carbon poisoning	93
4.4	Conclusions	93
Chapter-5	Modelling of multicomponent mass transport and carbon deposition in SOFC anodes	95
5.1	Introduction	95
5.2	Model development	95
5.2.1	Mass transport model	96
5.2.2	Chemical model	97
5.2.3	Electrochemical model	99
5.3	Model geometry	99
5.4	Numerical approach	101
5.5	Boundary conditions	101
5.6	Results and discussion	102
5.7	Conclusions	107
Chapter-6	Conclusion and future work	108
6.1	Conclusions	108

6.2	Recommendations for future work	110
	References	111
	Appendices	122
	Appendix A	128
	Appendix B	131
	Appendix C	132
	Appendix D	133

Nomenclature

Acronyms

AFC	Alkaline Fuel Cell
BCC	Body Centered Cubic
BSC	Back Scattered Coefficient
BSCF	Barium-Strontium-Cobalt-Ferro
BSE	Back Scattered Electrons
CFD	Computational Fluid Dynamics
CGO	Gadolinium Doped Ceria
CT	Computed Tomography
DEM	Discrete Element Method
DMFC	Direct Methanol Fuel Cell
EDBS	Energy Dispersive Back Scattered
EDS	Energy Dispersive X-Ray Spectroscopy
EIS	Electrochemical Impedance Spectroscopy
EMPT	Effective Medium Percolation Theory
ESB	Energy Selective Backscattered
EXAFS	Extended X-ray Absorption Fine Structure
FCC	Face Centered Cubic
FEGSEM	Field Emission Gun Electron Microscope
FEM	Finite Element Method
FIB-SEM	Focused Ion Beam Scanning Electron Microscopy
FTIR	Four Transformed Infrared Spectroscopy
HCl	Hydrochloric Acid
HRTEM	High Resolution Transmission Electron Microscopy
HT	High Temperature
IARC	International Agency for Research on Cancer
IT	Intermediate Temperature
LBM	Lattice Boltzmann Method

LSCF	Lanthanum Strontium Cobalt Ferrite
LSM	Lanthanum Strontium Manganite
LT	Low Temperature
LV	Low Voltage
MCFC	Molten Carbonate Fuel Cell
MDR	Methane Dry Reforming
MRLD	Microstructure Induced Load Distribution
MSR	Methane Steam Reforming
Ni	Nickel
NiO	Nickel Oxide
PAFC	Phosphoric Acid Fuel Cell
PCFC	Protonic Ceramic Fuel Cell
PEM	Polymer Exchange Membrane
PVC	Poly Vinyl Chloride
RPP	Random Particle Packing
SAFC	Sulfuric Acid Fuel Cell
SE	Secondary Electron
SEI	Secondary Electron Imaging
SEM	Scanning Electron Microscopy
SOFC	Solid Oxide Fuel Cell
TPB	Triple Phase Boundary
TPO	Temperature Programmed Oxidation
TPR	Temperature Programmed Reduction
TWS	Trainable Weka Segmentation
TXM	Transmission X-ray Microscopy
WEKA	Waikato Environment for Knowledge Analysis
WGS	Water-Gas Shift
XANES	X-ray Near Edge Spectroscopy
XCT	X-ray Computed Tomography
XNT	X-ray Nano Tomography

XRD	X-Ray Diffraction
YSZ	Yttria Stabilized Zirconia
1-D	One Dimensional
2-D	Two Dimensional
3-D	Three Dimensional

Symbols

a_{ij}	Interface area between i and j phase particle (m^2)
A_A	Area fraction of a phase of interest
A_{TPB}	Triple phase boundary area per unit volume of electrode ($m^2 m^{-3}$)
d	Diameter of a particle
\tilde{D}^{eff}	Normalized effective diffusivity
D_{ij}	Binary mass diffusivity (m^2/sec)
F	Faraday constant
I	Current density (A/m^2)
J_i	Diffusion flux of species i ($kg/m^2 \cdot sec$)
k_s	Growth constant for nickel particle while coarsening (h^{-1})
K_n	Knudsen number
L	Length of a line (m)
L_A	Total length of perimeter of phase of interest per unit area of sample image (m^{-1})
L_L	Fraction of length of lines hitting the phase of interest divided by the total length of lines placed on the image
L_{TPB}	Triple phase boundary length per unit volume of electrode ($m m^{-3}$)
M_i	Molar mass of species i ($kg/kg\text{-mole}$)
n_c	Critical number fraction for percolation in the packing
n_i	Number fraction of i phase particles
n_j	Number fraction of j phase particles
n_t	Total number of particle per unit volume (m^{-3})
N_{ij}	Average contact number of j phase particles with i phase particle when $n_i \approx 0$
N_{ii}	Average contact number of i phase particles when only i phase particles in packing

N_{jj}	Average contact number of j phase particles when only j phase particles in packing
P	Pressure (Pa)
P_A	Triple phase boundary points per unit area of image (m^{-2})
P_i	Percolation probability of i phase particles
P_j	Percolation probability of j phase particles
P_L	Number of intersection points with feature lines or curves per unit length of a probe line (m^{-1})
P_P	Number of points hitting the phase of interest divided by the total number of points placed on the image
r_i	Radius of i phase particle (m)
r_j	Radius of j phase particle (m)
r_{pore}	Radius of pore (m)
r_{Ni}^o	Initial radius of nickel particle (m)
$r_{Ni}(t)$	Radius of nickel particle at time “t” (m)
r_{Ni_c}	Radius of nickel particle after carbon deposition (m)
r_{Ni}^{max}	Maximum radius of nickel particle obtained after coarsening (m)
r_{pore}	Average pore radius (m)
R_{el}	Resistance between two electron conducting particles (ohm)
R_{ion}	Resistance between two ion conducting particles (ohm)
R_i	Chemical reaction rate for production and consumption of species i
t	Time (hour)
T	Temperature (K)
S_j	Surface area fraction of j phase particles
S_{ij}^V	Interface surface area between i and j phase particles per unit volume of electrode ($m^2 m^{-3}$)
S_V	Surface area of a phase per unit volume ($m^2 m^{-3}$)
V_V	Volume fraction of a phase of interest in 3D volume
V_i	Molar volume of species i (m^3/mol)
X_j	Mole fraction of i species
Y_i	Mass fraction of i species
Z	Average coordination number of a particle
Z_{ij}	Average coordination number of i phase particles in contact with j phase particles
Z_{ji}	Average coordination number of j phase particles in contact with i phase particles

Z_{ii}	Average coordination number of i phase particles in contact with i phase particles
Z_{jj}	Average coordination number of j phase particles in contact with j phase particles
Z_j	Average coordination number of j phase particles in contact with both i and j phase particles
Z_i	Average coordination number of i phase particles in contact with both i and j phase particles
α	Size ratio of j phase particle with i phase particle
ε_o	Initial anode porosity
ε	Porosity in anode
Υ	skewness
σ_0	Pure conductivity of material (S/m)
σ_{eff}	Effective conductivity of material (S/m)
σ_{Ni_c}	Effective conductivity of electron conducting particle after carbon deposition (S/m)
$\tilde{\sigma}_j^{eff}$	Normalised effective conductivity of j phase particles
ρ_{Ni}	Resistivity of nickel particle (ohm-m)
ρ_c	Resistive of carbon particle (ohm-m)
ρ	Mass density of gas mixture (kg/m ³)
τ	Tortuosity of a phase
v	Velocity term for convective transport
θ	Contact angle between i phase and j phase particle
ψ_j	Volume fraction of j phase particles in electrode
ψ_i	Volume fraction of i phase particles in electrode
ψ_c	Volume fraction of carbon in anode
ψ_{Ni_o}	Initial volume fraction of nickel particles
ψ_{Ni_c}	Volume fraction of electron conducting phase after carbon deposition
ψ_{YSZ_o}	Initial volume fraction of YSZ particles
ψ_{YSZ}	Volume fraction of YSZ particles

Subscripts

el	Electron conducting particle
ion	Ion conducting particle

<i>IM</i>	Intercept method
<i>Ni</i>	Nickel particle
<i>YSZ</i>	YSZ particle
<i>Ni_c</i>	Nickel particle covered with carbon

List of Figures

Figure no.	Figure title	Page no.
1.1	Schematic of thesis structure and organisation	6
2.1	Microstructural investigation methods	9
2.2	Schematic of a SOFC electrode showing three types of particle clusters	10
2.3	Three dimensional representation of electrode geometry made of monodisperse particles	17
2.4	Equivalent circuit between two electron conducting sites (a) two ion conducting sites (b) and, between an electron conducting and an ion conducting site (c)	19
2.5	Histogram of grey scale value of Ni-YSZ cermet	26
2.6	Schematic representation of steps involved in 3-D reconstruction of the electrode.	31
2.7	Schematic of dual beam FIB-SEM arrangement	32
2.8	Schematic of XNT (X-ray nano tomography)	40
3.1	Workflow diagram	52
3.2	Anode substrate before reduction (a), after reduction (b)	54
3.3	Different types of electrons generation during interaction of incident electron beam with matter	56
3.4	Interaction volume of electron beam with different atomic number materials	56

3.5	Background X-ray generation during atom-electron beam interaction	58
3.6	Characteristic X-ray generation from an atom during interaction with electron beam	58
3.7	Low voltage secondary electron image (a), histogram of secondary electron image (b), low voltage inlense BSE image (c), histogram of inlense BSE image (d), high voltage BSE image of sample (e), histogram of high voltage BSE image (f)	61
3.8	EDS map of Ni-YSZ anode substrate (a), high voltage BSE image (b), overlaid BSE image on EDS map (c), greyscale image of superimposed image (d) histogram of superimposed greyscale image (e)	62
3.9	Greyscale image (a), segmented image obtained using Otsu's thresholding method (b), segmented image obtained using TWS (c)	63
3.10	Some possible combinations of TPB pixels (a), not a TPB point (b)	65
3.11	Thickness diagram for pore phase in a sample (a) and, size distribution of pore size (b) in sample	66
3.12	Five microstructures S1 to S5 resulted from different Ni particle size	67
3.13	Volume fraction for Ni in microstructure S1 to S5 (a), Volume fraction for YSZ in microstructure S1 to S5 (b) and, Volume fraction for Pore in microstructures S1 to S5 (c)	71
3.14	Nickel Feret diameter (a), Nickel equivalent diameter (b) and, Nickel local thickness (c) for microstructures S1 to S5	72

3.15	YSZ local thickness (a) and, Pore local thickness (b) for microstructures S1 to S5	73
3.16	Size ratio of YSZ to nickel particle for microstructures S1 to S5	73
3.17	Ni-YSZ interface area (a), Ni-Pore interface area (b) and, YSZ-Pore interface area (c) for microstructures S1 to S5	74
3.18	Triple phase boundary length for microstructures S1 to S5	75
4.1	Nickel particle surface areas covered by Nickel and YSZ; and exposed to pore	81
4.2	Carbon distribution over nickel particles	84
4.3	Schematic of anode where nickel particles are covered by carbon	84
4.4	Triple phase boundary length variation with volume fraction (a), Triple boundary area variation with volume fraction and size of particles (b), with volume fraction and size ratio of particles (c), with porosity(d), with particle size (e)	88
4.5	Nickel-pore interface area variation with particle size (a), with nickel volume fraction (b)	89
4.6	nickel coarsening effect on TPB area (a), Ni-pore area (b), pore size (c), tortuosity (d), effective conductivity of e ⁻ conducting (e) and, ion conducting phase (f)	91
4.7	Carbon effect ($\epsilon_o=0.23$) on TPB area(a), pore size(b),effective conductivity of electron conducting phase(c), ion conducting phase(d) and, tortuosity (e)	92

5.1	Model anode geometry with 30% porosity (a), 40% porosity (Microstructure 1) (b) and, 50% porosity (c)	100
5.2	Three different microstructures with constant porosity (40%) and increasing gas-solid interface area microstructure 2, microstructure 3, microstructure 4	100
5.3	Model geometry to represent anode microstructure and boundary conditions	101
5.4	Molar fraction distribution of H ₂ (a), CO (b), CO ₂ (c), CH ₄ (d), and H ₂ O (e) in porous anode along the anode thickness	103
5.5	Average mole fraction of H ₂ , CO, CH ₄ , H ₂ O, CO ₂ in porous anode with chemical reactions and electro-chemical oxidation of H ₂ at anode-electrolyte interface	104
5.6	Average mole fraction of H ₂ (a), CO (b), CO ₂ (c), CH ₄ (d), H ₂ O (e) and average carbon deposition rate along the anode thickness	105
5.7	Average mole fraction of H ₂ (a), CO (b), CO ₂ (c), CH ₄ (d), H ₂ O (e) and average carbon deposition rate (f) along the anode thickness	106

List of Tables

Table no.	Table title	Page no.
1.1	Fuel Cell Classification	1
1.2	Solid Oxide Fuel Cell Classification	3
3.1	Steps for polishing procedure	55
3.2	Volume and weight fraction of individual phases in Ni-YSZ anode substrate	68

Chapter 1

Introduction

1.1 Background and Motivation

Fossil fuels have been used as the main energy source since the beginning of industrial revolution. The increase in fossil fuel consumption leads to the fast depletion of natural reserves and negatively impacts the environment. Traditionally, heat engine, gas turbine, steam turbine and similar devices are used to generate electricity from fossil fuels. The ever-increasing demand for energy and environmental challenges require the development of alternative fuel sources and energy system. In this regard, many researchers around the world are focusing on the development of efficient energy storage and energy conversion devices.

Table 1.1 Fuel Cell Classification (1)

Fuel Cell	Electrolyte	Operating temperature (°C)	Fuel
PEMFC (Proton Exchange Membrane)	Proton exchange membrane	50~80	Methanol or hydrogen
SAFC (Sulphuric Acid Fuel Cell)	Sulphuric acid	80~90	Alcohol or less pure hydrogen
AFC (Alkaline Fuel Cell)	Potassium hydroxide	50~200	Pure hydrogen or hydrazine
DMFC (Direct Methanol Fuel Cell)	Polymer	60~200	Methanol
PAFC (Phosphoric Acid Fuel Cell)	Phosphoric acid	160~210	Hydrogen
MCFC (Molten Carbonate Fuel Cell)	Molten salt	630~650	Hydrogen, natural gas, propane
PCFC (Protonic Ceramic Fuel Cell)	Barium cerium oxide membrane	600~700	Hydrocarbons, hydrogen
SOFC (Solid Oxide Fuel Cell)	YSZ/SDC	600~1000	Hydrogen, natural gas or propane

Fuel cells are the energy conversion devices that convert chemical energy directly into electrical energy by a single step electrochemical conversion through the chemical and electrochemical reactions. A fuel cell consists of an anode and a cathode separated by an electrolyte. Fuel cells are classified on the basis of electrolyte used, operating temperature and type of fuel used. Fuel cell classification is illustrated in Table 1.1

The focus of this thesis is on the SOFC, whose high efficiency and fuel flexibility makes it a promising device. SOFC use ceramics as the electrolyte and operates at high temperatures 600-1000 °C facilitated by the limited ion conductivity of the electrolyte. This fuel flexibility in the SOFC arises due to the oxide ion movement through the electrolyte. This allows in principle, to directly electro-oxidize the hydrocarbon fuels instead of chemical oxidation in the combustion process of hydrocarbon fuels (2). The SOFC technology is being developed for a broad range of applications such as heat and power generation in residential and industrial sectors, transport applications, especially naval transport, and oxygen production. The state of art materials for SOFC are: anode layer is made of Ni-YSZ (Nickel- Yttria Stabilised Zirconia) cermet, cathode is made of LSM-YSZ (Lanthanum Strontium Manganite- Yttria Stabilised Zirconia) and, electrolyte is made of YSZ (Yttria Stabilised Zirconia). The state of art SOFC materials are the result of engineering optimisation that takes into account the manufacturing challenges, performance requirements and the cost. To generate electricity in the fuel cell, oxygen molecules diffuse through the cathode towards electrolyte due to the concentration gradient. These molecules get converted into oxide ions by the electrochemical reduction at the active sites of the cathode. The oxide ion diffuses through the electrode towards anode; the electrodes are porous composites for the diffusion of reactants but electrolyte is dense and does not conduct any oxidant or fuel molecule. The oxide ion reacts at the triple phase boundary surface at the anode with fuel molecules. Active surface area for electrochemical reaction involves Triple Phase Boundary (TPB) of YSZ particles through which oxide ion transports, pores in the anode for reactant diffusion and nickel particles for the electron conduction. SOFC can be classified on the basis of their operating temperature, cell and stack design, support structure, flow configuration and fuel reforming as described in Table 1.2.

Along with the numerous advantages of SOFC, there are several challenges in SOFC commercialisation due to the high material cost, fuel availability and storage, durability under start-stop cycle, rapid performance degradation and lower volumetric power density compared to batteries and combustion engines. SOFC performance greatly depends upon the microstructure of the electrodes. Electrochemical active area, interface surface area, porosity, the charge and mass transport phenomena are the main characterisation properties for SOFC electrode performance. Electrode microstructures are highly tortuous and complex three-dimensional networks of electron, ion and gaseous species transport paths. Therefore, better understanding of the interplay between microstructural parameters, microstructural properties, and effective transport properties of electron, ion and gaseous species will help to optimise the electrode performance.

Table 1.2 Solid Oxide Fuel Cell Classification

Classification Criteria	SOFC Classification
Operating Temperature	Low –Temperature (LT)-SOFC (500°C – 650°C), Intermediate Temperature (IT)-SOFC (650°C – 800°C), High-Temperature (HT)-SOFC (800°C – 100 0°C)
Manufacturing Design	Planar SOFC, Tubular SOFC, Segmented-in-series SOFC, and Monolithic SOFC
Cell Support	Anode supported, Cathode supported, Electrolyte supported, or interconnect supported cell.
Flow Configuration	co-flow, counter-flow, cross-flow
Fuel Reforming	External reforming, Internal reforming

There is a requirement of 50000 hours of operational time and degradation rate of less than one percent per thousand hours for the commercialisation purpose (3). The main reason for the performance degradation of SOFC comes through the material degradation of SOFC components. SOFC electrode performance degradation arises due to the reason of catalyst poisoning in the electrodes and structural stresses induced in the electrodes at high operating temperatures. Therefore, the investigation

of structural degradation on microstructural properties will further help to micro-engineer the electrodes for the optimised performance. The effect of electrode microstructural parameters on performance and the effect of degradation phenomena such as carbon deposition and nickel coarsening on the anode performance are critical areas of research towards the performance improvement and commercialisation of SOFC.

1.2 Contributions of the Thesis

The main contributions of this research thesis are summarised as follows.

- Investigation of the effect of nickel particle size on microstructural properties using the image analysis and stereological techniques. We proposed EDS maps combined with BSE imaging to segment the Ni-YSZ anode image into its constituent phases and the application of machine learning tools for image segmentation in Ni-YSZ anode.
- Developed a microstructure model to evaluate the microstructural properties with the co-ordination number and percolation probability expressions suggested by Bertei et al. (4) and compare the results with the earlier developed model by Chen et al. (5). We have further extended our model to investigate the effect of structure degradation effects such as nickel coarsening and carbon deposition phenomena during cell operation on microstructural properties.
- Utilisation of CFD (Computational Fluid Dynamics) techniques to investigate anode microstructure (porosity and gas-solid interface area) effect on the reactant and product species distribution, species transport and, carbon deposition in the anode.

1.3 Thesis Structure

This research thesis consists of six chapters. In the second chapter on comprehensive literature review, we briefly discuss the state of art in the mathematical and experimental techniques used to evaluate the microstructural properties of electrodes, the limitations and strengths of these techniques, applications and recent developments in these techniques. We suggest areas of improvement in the present techniques to evaluate microstructural properties and also suggest new methods to evaluate these properties.

In the third chapter, the nickel particle size effect on the anode microstructural properties is studied using the microscopic images. Improvements over imaging techniques have been suggested for image segmentation and also the application of machine learning tools have been suggested for image analysis.

Chapter four details the development of microstructure model to evaluate microstructural properties using analytical approach. The microstructure model is further extended to investigate the effect of microstructure degradation due to nickel coarsening and carbon poisoning on the microstructural properties.

In Chapter five, the effect of anode microstructural properties such as porosity and gas-solid interface area on the species transport and species distribution has been investigated using a CFD approach.

In the last chapter, the conclusions derived from this thesis are discussed with recommendations for future research.

Thereafter, a list of relevant references is provided. All these references are cited in the literature and main chapters.

Finally, this thesis ends with appendices, which details the flowchart for the MATLAB code used for image analysis and to extract quantitative microstructural information from the specimen images. Flowcharts for the chemical reaction rate codes are also provided which were used during CFD modelling in chapter five.

Figure 1.1 gives the schematic of thesis structure and organisation.

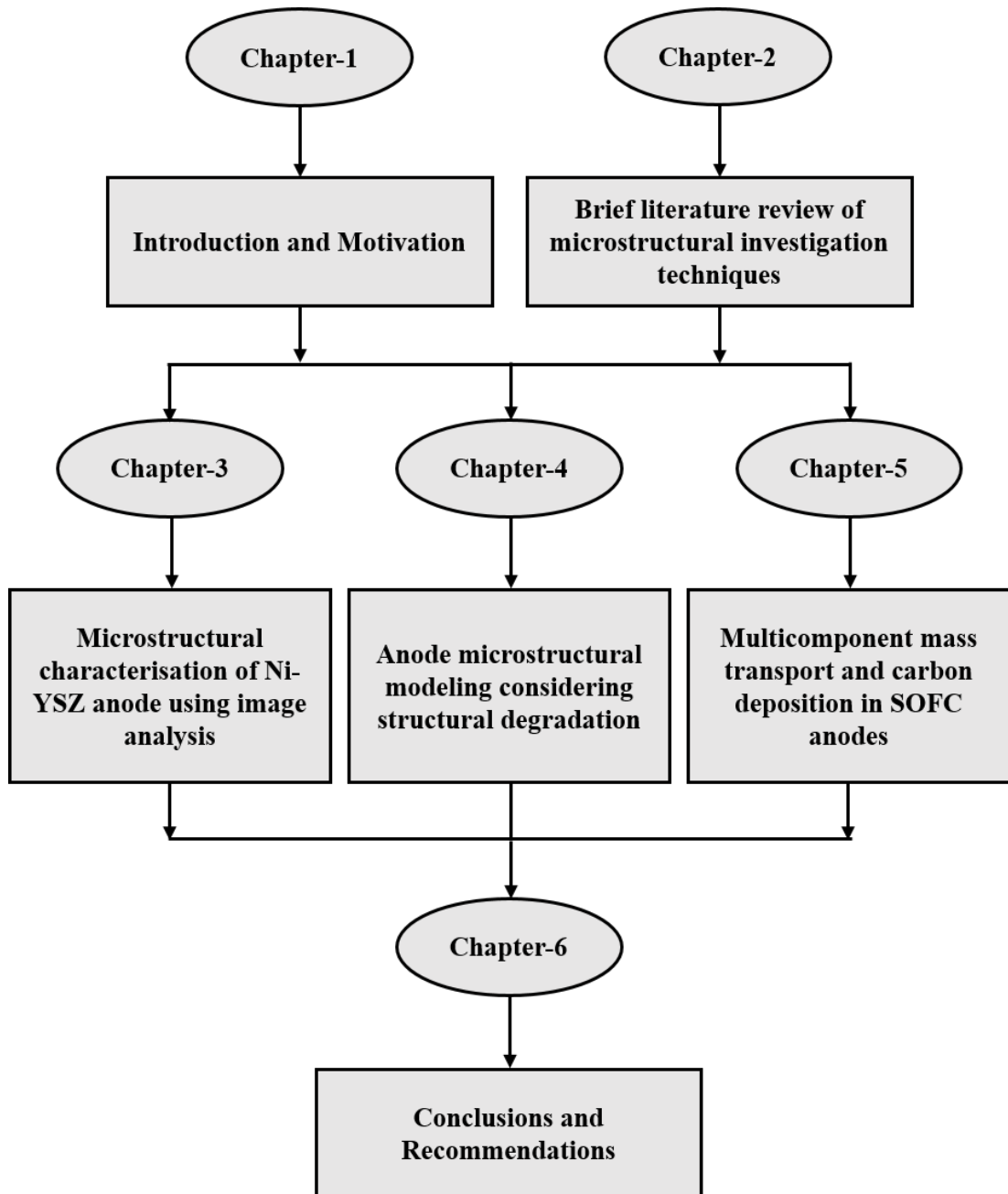


Figure 1.1 Schematic of thesis structure and organisation

Chapter 2

Literature review

2.1 Microstructural investigation in Solid Oxide Fuel Cell Electrodes

2.1.1 Introduction

SOFCs are becoming one of the main contenders in the fight for eco-friendly future energy conversion devices because of their low emission rates, high electrical generation efficiency, fuel flexibility and potential for low operating cost (6). For this reason, research has increasingly started focusing on the improvement of the performance of SOFCs, which is measured as the magnitude of power density generated. Among the SOFC components, namely, the electrodes and the electrolyte, the electrolyte performance is governed by the conductivity and thickness of the electrolyte and the cermet electrode performance is determined by the sum of various polarisations associated with the rates of charge transfer at the *electronic conductor-ionic conductor-gas* three phase boundaries, the effective conductivity of electronic and ionic conductors and the rates of transport of gases through the porous electrode.

The porous composite electrodes involve three phases. The ion conducting phase (typically YSZ), is used in both the anode and cathode) must be a good oxygen ion O^{2-} conductor, with very little electronic conduction. The electron-conducting phase typically nickel in the anode and LSM in the cathode, must have good electronic conduction, with very little ionic conduction. The pore phase must facilitate gas transport. Charge-transfer reactions proceed at the three-phase boundaries that are formed at the intersections of the three phases.

There is a need to develop predictive models that can assist in optimising the cell's architecture as SOFC electrode performance depends greatly upon the microstructure of the composite electrodes. These microstructural properties include TPB length, phase volume, individual phase surface area and interface areas, phase connectivity and conductivity, and phase tortuosity.

TPB is defined as the region where all the three phases are present to support the electrochemical reaction. For a site to be an active TPB site there should be continuous availability of electron, ions and reactants to it. There must be a path

available from the source (or sink) to the reaction site. Thus, electronic, ionic and pore phases must percolate through the structure of electrode and one end should be connected to the source (or sink) boundary.

There have been several microstructural modelling approaches (as shown in Figure 2.1) developed to investigate the relation between the microstructure and its performance. These methods to investigate microstructural properties are namely analytical methods, 3-D reconstruction using numerical methods, 2-D image analysis and stereology, 3-D reconstruction of electrodes using 2-D Images and, 3-D reconstruction of electrodes using experimental methods. A thorough review of all these methods is presented in this thesis. Reviews covering one or few of these techniques are available in the literature (7-10) but due to the utmost importance of electrode microstructural optimisation in SOFC performance, these techniques require an extensive comparative analysis. In the analytical methods, one approach is based on the random packing of spherical particles and the use of coordination number principles and percolation theory to develop relations for microstructural parameters and properties (5, 11-22). In the numerical methods, electrodes are reconstructed by packing the electron conducting particles and ion conducting particles in a 3-D domain either randomly or in an ordered manner (8, 23-35), and further properties are calculated. Most of these models are based on the assumption of microscopic homogeneity of composite electrode particles.

Image analysis and stereological analysis to evaluate microstructural properties involves the imaging of samples and the application of stereology techniques to extract 3-dimensional quantitative information from the 2-dimensional images (36-41). Reconstruction of the electrodes using experimental methods are time and cost intensive but gives a real representation of electrode structure and the most reliable investigation of electrode properties and electrochemical performance (42-63).

These microstructural modelling approaches provide the unique opportunity to assist with the design and development of electrodes for the next generation solid oxide fuel cells. These techniques enhance our ability to understand the connections between functional and degradation behaviour and their impact on the cell performance.

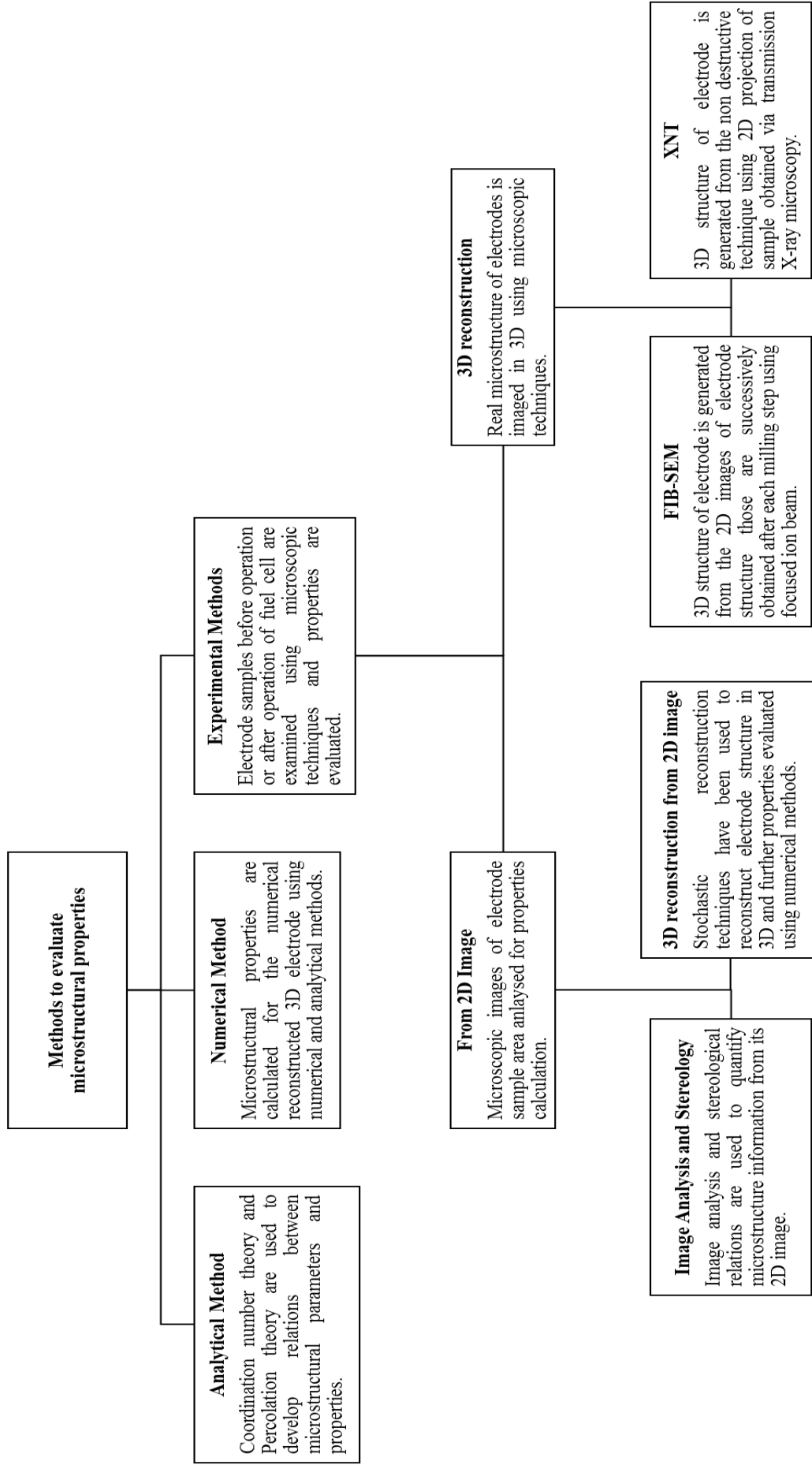


Figure 2.1: Microstructural investigation methods

2.1.2 Microstructural modelling using analytical methods

Analytical methods are simpler and quicker in evaluating the microstructural properties, but have limited scope. These methods utilise the rationalised simplification of the actual microstructure for property calculation. These approaches cannot mimic the actual microstructure of electrodes and give an average value of properties over the domain. Coordination number theory and percolation theory are used to evaluate the structural properties from the electrode structure represented by the random packing of spherical particles as its constituents. The electrode is assumed to be composed of spherical particles of its constituent phases. Particles of particular nature should percolate through the electrode to transport the corresponding ions or electrons in the electrode. There is a threshold concentration for particular kinds of particles to form a percolated network across the electrode. Three types of networks that can exist namely (14), A, B and C as shown in Figure 2.2.

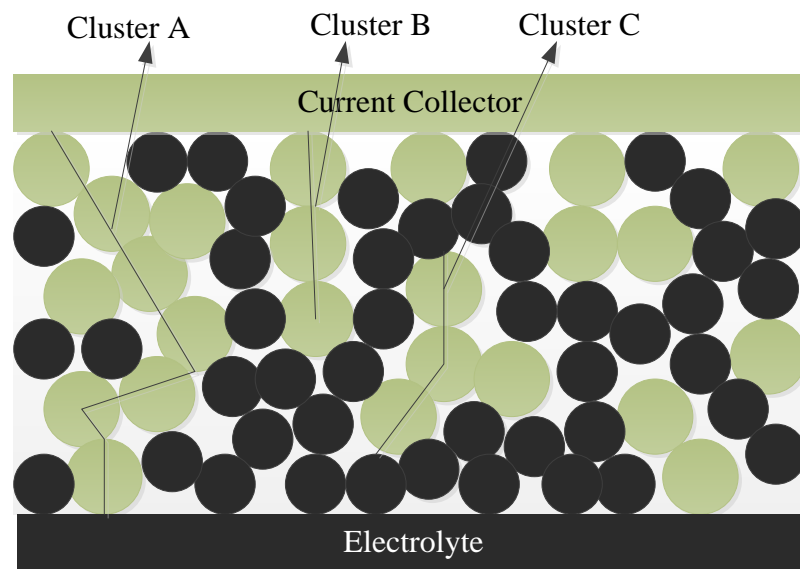


Figure 2.2: Schematic of a SOFC electrode showing three types of particle clusters.

In this electrode schematic, Cluster A is the continuous network of electron conducting particles connecting both ends of electrode, Cluster B is shorter network connecting current collector to the limited thickness of electrode and Cluster C is the isolated network of electron conducting particles that will not be able to transport any electrons in the electrodes resulting in inactive area for the electrochemical reaction.

There is also a threshold volume fraction for ionic or electronic conducting particles above which they will form only A-type of clusters. Percolation threshold value is significantly affected by the particle size ratio of the two different kinds of electrode constituent particles and by the thickness of the electrode.

There are two theories to calculate the co-ordination number in binary random packing of spheres. One is proposed by Bouvard and Lange (11), where the co-ordination number between two particles is given by equation (2.1) and equation (2.2)

$$Z_{ij} = n_j \frac{Z_i Z_j}{Z} \quad (2.1)$$

Where,

$$Z_i = 3 + \frac{Z - 3}{n_i + (1 - n_i)\alpha^2}$$

$$Z_j = 3 + \frac{(Z - 3)\alpha^2}{n_i + (1 - n_i)\alpha^2}$$

$$Z = n_i Z_i + n_j Z_j$$

And,

$$Z_{ii} = \frac{n_i}{Z} \left(3 + \frac{Z - 3}{n_i + (1 - n_i)\alpha^2} \right)^2 \quad (2.2)$$

Where Z is the average co-ordination number and it is equal to six (11), Z_i is the average coordination number of the i phase (electron conducting) particle, and Z_j is average coordination number of the j phase (ionic conducting) particle, α is size ratio r_j/r_i , Z_{ij} is the average number of j phase particles in contact with any i phase particle, Z_{ii} is the average number of i phase particles that are in contact with any i phase particle and n_i , n_j are the number fraction of the i phase and the j phase particles.

The second theory for the coordination number calculation is proposed by Suzuki & Oshima (16) for binary composite where the co-ordination number between two particles Z_{ij} (equation 2.3) is proportional to surface area fraction of one type of particles and N_{ij} (the average contact number of all j phase particles with i phase particle in a particular idealised mixture where the number fraction of i phase particle is nearly zero and overall coordination number of this mixture is same as any other composition mixture).

$$Z_{ij} = S_j N_{ij} \quad (2.3)$$

Where,

$$N_{ij} = \frac{0.5(2 - \sqrt{3})N_{ii}(r_i/r_j + 1)}{1 + r_i/r_j - (r_i/r_j (r_i/r_j + 2))^{0.5}}$$

$$Z_{ii} = \frac{Z n_i}{n_i + (1 - n_i)\alpha^2}$$

$$Z = n_i Z_i + n_j Z_j \quad (2.4)$$

Where, Z is average coordination number in random pack of mono-size spheres (11) and calculated using equation (2.4). Bouvard and Lange (11) model satisfies the contact number conservation principle whereas this theory does not satisfy. Contact number conservation principle is given as equation (2.5):

$$n_j Z_{ji} = n_i Z_{ij} \quad (2.5)$$

Chen et al. (5) further modified the model given Suzuki and Oshima (16) to satisfy the contact number conservation principle, where coordination number between two particles given by equation (2.3) where N_{ij} is given as equation (2.6)

$$N_{ij} = \frac{Z}{2} \left(1 + \frac{r_i^2}{r_j^2} \right) \quad (2.6)$$

Where Z is average coordination number and considered to be equal to six. This expression was further generalised for poly-dispersed distribution of particle sizes (5) and validated with simulated results reported by Suzuki and Oshima (16). These expressions for co-ordination numbers were further used for microstructural properties evaluation.

Bertei et al. (4) have compared all earlier developed co-ordination number relationships with simulation results of random packing of particles and found that the Suzuki and Oshima (16) results are well matched with simulation results for size ratio greater than one (equation 2.7), however for smaller particle size ratio less than one, they derived a new relationship (equation 2.8) based on coordination number theory by Suzuki and Oshima and contact number conservation principle.

$$N_{ij} = \frac{0.5(2 - \sqrt{3})N_{ii}(r_i/r_j + 1)}{1 + r_i/r_j - (r_i/r_j (r_i/r_j + 2))^{0.5}} \quad (2.7)$$

$$N_{ji} = \frac{0.5(2 - \sqrt{3})N_{jj}(r_i/r_j + 1)}{(1 + r_i/r_j - (r_i/r_j(r_i/r_j + 2))^{0.5}) r_i/r_j^2} \quad (2.8)$$

And, the overall coordination number is calculated using equation (2.4).

To evaluate the mass transport properties, electronic and ionic transport properties in the electrode, percolation probability is calculated for the pore, electronic phase and ionic phase in electrode. Bouvard and Lange gave an expression (equation 2.9) for the same using simulated results as

$$P_i = \left(1 - \left(\frac{4 - Z_{ii}}{2}\right)^{2.5}\right)^{0.4} \quad (2.9)$$

Kuo and Gupta (12) also derived percolation threshold values and found that the above expression proposed by Bouvard and Lange (11) agrees well with experimental data for $\alpha > 1$ for the Z_{ii} expression given by Bouvard and Lange (11), but it agrees well for experimental data in the range of $0.154 < \alpha < 6.464$ for the coordination number model proposed by Suzuki and Oshima (16, 64, 65). The above expression gives percolation threshold at $Z_{ii} = 2$. Kuo and Gupta (12) estimated the critical coordination number $Z_{ii} = 1.764$ in the monosize binary mixture system corresponding to critical volume fraction for conductivity percolation. Chan and Xia (13) further modified the percolation probability expression (equation 2.10) from the Bouvard and Lange(11) simulation results to satisfy the estimated critical coordination number

$$P_i = \left(1 - \left(\frac{4.236 - Z_{ii}}{2.472}\right)^{2.5}\right)^{0.4} \quad (2.10)$$

Where, P_i , is the percolation probability of i phase.

Bertei et al. (4) derived a new expression for percolation probability (equation 2.11), which was derived from nonlinear least square regression on simulated results from Bouvard and Lange (11) for percolation in particle packing.

$$P_i = 1 - \left(\frac{4.236 - Z_{ii}}{2.472}\right)^{3.7} \quad (2.11)$$

Costamagna et al (14) proposed an expression for electrochemical active area (equation 2.12) that is proportional to number of contact points between electronic

and ionic conducting phase multiplied by the probability that a particle belongs to the A-cluster:

$$A_{TPB} = \pi K r_i^2 n_t n_i P_i P_j Z_{ij} \quad (2.12)$$

Where,
$$K = \sin^2 \frac{\theta}{2}$$

Where, A_{TPB} is the triple phase boundary area, phase material i is the phase considered having the smaller particle size, θ is the contact angle between two types of particle and, n_t is the total number of particles. Costamagna et al. (14) used the Bouvard and Lange (11) model to calculate percolation probability and coordination number values (Z_{ij}), whereas Suzuki and Oshima (16) models were used to calculate the threshold volume fraction. Few other authors have used active triple phase boundary length in the electrochemical model (7) (66). Sunde et al. (7) gave an expression for the triple phase boundary length (equation 2.13) in unit volume of electrode using the percolation theory and coordination number theory in the random packing of spherical particles.

$$L_{TPB} = 2\pi r_i \sin \frac{\theta}{2} n_t n_i P_i P_j Z_{ij} \quad (2.13)$$

Chen et al. (19) further used explained above theories to give a TPB expression (equation 2.14) for the poly-dispersed particle size variation for electronic and ionic conducting phases.

$$L_{TPB,eff}^V = \sum_{i=1}^k \sum_{j=1}^l l_{el_i-io_j} n_{el_i}^V Z_{el_i-io_j} P_{el} P_{io} \quad (2.14)$$

where $L_{TPB,eff}^V$ is the effective triple phase boundary length, $n_{el_i}^V$ is the number per unit volume of electron conducting particles in size class i , P_{el} and P_{io} are the percolation probability of electronic and ionic phase particles, respectively. The $l_{el_i-io_j}$ contact perimeter between electron conducting and ion conducting particles, same as evaluated in case of binary particles but now this expression is able to consider a range of particle size.

Gokhale et al. (67) have developed an expression (equation 2.15) for the triple phase boundary based on stereological relations, and it considers the effect of particle shape, size, size distribution and skewness on the TPB.

$$L_{TPB} = \frac{\pi}{4} F_1(\alpha) F_2(\theta_P) F_3(K) F_4(CV, Y) \frac{1}{\langle d_i \rangle \langle d_j \rangle} \quad (2.15)$$

Where, $\langle d_i \rangle$ and $\langle d_j \rangle$ are the average size of individual phase particles, $F_1(\alpha)$ considers the effect of volume fraction of solid phase components, $F_2(\theta_P)$ considers the porosity effect, $F_3(K)$ considers the shape effect of particles and $F_4(CV, Y)$ counts for contribution of size distribution variation CV and skewness Y . This expression is more generalised and doesn't require the calculation of coordination number in the electrode, however percolation effect was not considered in this expression.

Costamagna et al. (14) gave an expression for the effective conductivity of electronic or ionic phase in electrode based on the percolation theory (68) and percolation threshold values (12). The effective conductivity of the electrode is given as (equation 2.16) (14)

$$\sigma_{eff} = K \sigma_0 (n - n_c)^\mu \quad (2.16)$$

Where σ_0 is the conductivity of the pure material, n is the number fraction of the ionic or electronic conducting particles, number fraction of particles can be related with volume fractions of components also, and, n_c is the critical number fraction in the packing i.e, the percolation threshold number fraction below which the packing will be insulating.

$$K = \frac{\gamma}{(1 - n_c)^\mu}$$

μ is a universal exponent and is equal to 2 for three dimensions, γ is the adjustable parameter here to consider the effect of neck formation between particles on the effective conductivity and 0.5 is the most commonly value used for γ (69). Nam and Jeon (15) further gave another expression (equation 2.17) for effective conductivity of a particular phase based on percolation probability in random pack of spherical particles as:

$$\sigma_{eff} = \sigma_0 ((1 - \varepsilon) P \phi)^\mu \quad (2.17)$$

Where σ_0 is the conductivity for pure material, ε is the porosity, ϕ is the volume fraction, P is the percolation probability and, μ is a Bruggeman factor considering the distribution of a phase in space or domain, $\mu = 1.5$.

And, the average pore radius (equation 2.18) in the electrode is given as (5, 15, 21, 69):

$$r_g = \frac{2}{3} \left(\frac{1}{1 - \psi_g} \right) \left(\frac{1}{\psi_{el}/r_{el} + \psi_{io}/r_{io}} \right) \quad (2.18)$$

Where, ψ_g , ψ_{el} , ψ_{io} are the volume fractions of pore phase, electronic phase and ionic phases, respectively. Several authors used the mean particle radius as the pore radius of the electrode.(13, 66, 70)

Several correlations are given for the electrode tortuosity in the literature that are derived by analytical or numerical methods for the porous media and it was found to be mainly dependent on the porosity. Farhad and Hamdullahpur (21) gave the expression for tortuosity (equation 2.19) dependent on microstructural parameters as:

$$\tau \approx \frac{\varepsilon}{\frac{\pi}{4} d_{pores}^2 n_t^{2/3}} \quad (2.19)$$

Where τ is the tortuosity of electrode, d_{pores} is the diameter of pores and, $\frac{N_{pores}}{WL}$ are the number of pores per unit area of porous electrode. These expressions for porosity and tortuosity helped to calculate these properties from the microstructural parameters instead of numerical simulation or experimental investigations. Researchers have also used the tortuosity values from the experimental investigations for the electrode performance studies (13, 15, 22).

Chen et al. (18) further verified the evaluated microstructural properties with the experimental data reported by Wilson et al. (71) and Iwai et al. (52) using experimental reconstruction techniques. Chen et al. (19) showed good agreement for the calculated effective properties of electrodes composed of poly-dispersed particles with the results reported by Kenney et al. (23) based on random packing of particles. Chen et al. (72) used an earlier developed model to determine the effective properties for electrode composed of mixed electronic and ion conducting particles.

The above analytical approach gives the average properties of electrodes and does not consider the local distribution of properties in the electrode domain. This has been also used to study the transient behaviour of electrode properties, Sharma and Basu (73) have investigated the effect of nickel particle coarsening on anode

microstructural properties during cell operation using percolation theory and coordination number theory in random packing of spherical particles.

2.1.3 Microstructural modelling using numerical methods

3-D reconstruction of the porous electrode microstructure does not give the actual microstructure of the electrode but it can be the closest way to represent the actual structure. It offers the capability to consider the randomness of the microstructure. The reconstruction can be further used for the calculation of effective transport properties, multiphysics simulations and for electrochemical performance estimation. In this method, the electrode constituent particles are dropped in 2D or 3D domain in a random manner or in an arranged manner (Figure 2.3). The particles in the domain are further flattened to imitate the sintering phenomenon in actual electrodes. There are usually three kinds of particle packing arrangement as described below:

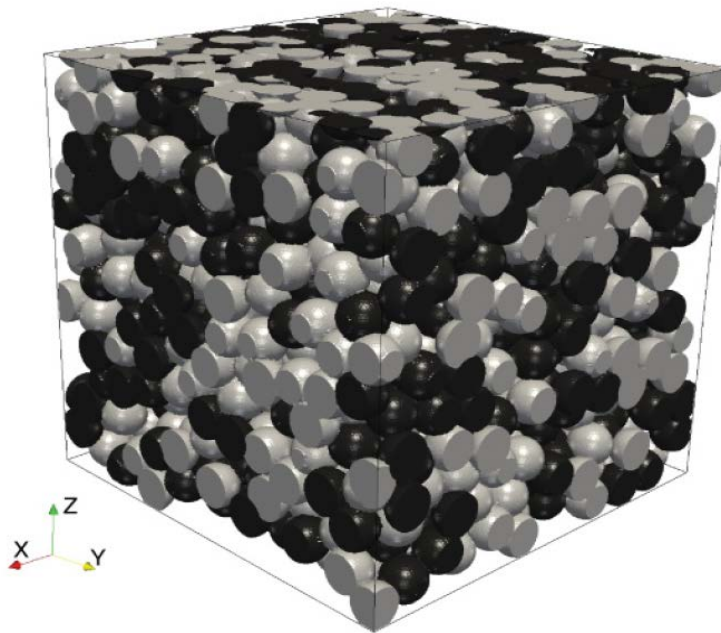


Figure 2.3. Three-dimensional representation of electrode geometry made of monodisperse particles. Particle in light grey and dark grey are the two kinds of particles in the structure. Reprinted with permission from ref (74). Copyright 2011 American Physical Society.

Random particle packing: (23, 26, 34, 35, 74) In this approach, the particles are randomly placed in unstructured agglomerates. Particles are added one at a time in the domain using different constraints. Usually, each particle is placed in such a way that it is in contact with three different particles. Desired

volume fraction of individual component is enforced by assigning a weighted probability to the particle selection before the particle is dropped.

Structured particle packing: In this approach, the particles are arranged at specific points in the domain depending on the type of lattice (FCC (Face Centered Cubic) lattice, BCC (Body Centered Cubic) lattice etc.).(25, 32) In this arrangement, the contact points of the particles are pre-determined and known. The only random variable is the type of particle.

DEM (Discrete Element Method) packing (8, 29): DEM is a numerical method for predicting the evolution of particle trajectories accounting for the inter-particle collisions and the effect of other relevant forces. Martin et al. (28) used DEM methodology for the compact packing of particles considering the plastic deformations at the particle contact and the rearrangement of the particles. Sanyal et al. (8) also used DEM approach for the reconstruction of the electrode including the sintering phenomenon in anode.

These reconstructed electrode microstructure are used to investigate the effect of structural parameters on microstructural properties and electrode performance. For the random packing, structured packing and DEM packing of the electrode particle, the properties were found to be dependent on the packing parameters (domain size, number of particles in packing and type of packing) and initial conditions given for the arrangement for the particles in the structure (29). Abbaspour et al. (34) found the packing density of random particle arrangement as 60% which was more than simple cubic lattice packing but less than FCC and BCC packing. Sanyal et al. (8) found the packing density of 68% for DEM packing and 53% for random packing of particles. Abbaspour et al. (34) have found the TPB value to be dependent on the number of particles in a layer, and found that after 700 particles in a layer, the deviation for the TPB value was in reasonable limit. Kenney et al. (23) have suggested the optimum size of 3D domain depending upon the size of particles considered for reconstruction. Sanyal et al. (8) have calculated the coordination number for the DEM packing; which was 6.7 and found to be consistent with Bouvard and Lange (11). He has also calculated the percolation probability for the DEM and RPP (Random Particle Packing), found to be consistent with percolation theory results. Yasutaka et al. (29)

results showed deviation from Sanyal et al. (8) for DEM packing, they found coordination number between 7 and 9, which results in overestimation of other microstructural properties also.

Effective conductivity of electrode has been evaluated by Resistor Network Modelling approach by Sunde (25, 26) and Abel et al. (32). In this modelling approach, each particle in the electrode is connected to its nearest particles through a resistance bond. In this way, a network of resistance bonds is formed between the different sites (a site can be occupied by an electron conducting particle, ion conducting particle or pore). Equivalent resistance between any two sites can be given as shown in Figure (2.4) where R_{el} is resistance between two electron conducting sites, R_{ion} is resistance between two ion conducting site and R_i is the two grain resistance of electrochemical reaction.

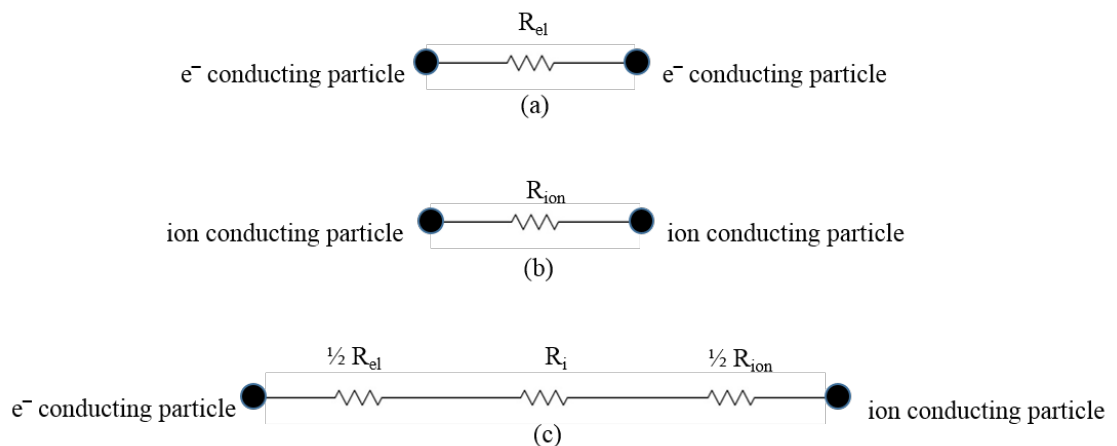


Figure 2.4. Equivalent circuit between two electron conducting sites (a) two ion conducting sites (b) and, between an electron conducting and an ion conducting site (c)

Sunde has evaluated effective conductivity using this approach in structural particle packing at sites of 3-D cubic lattice (25) and in the random packing of particles (26). Sunde has considered electron and ion conducting particles for the packing of electrode microstructure and assumed percolation of pores to the contact sites between electron and ion conducting particles. Abel et al. (32) have further considered pores also as a particle for the electrode microstructure generation using structural packing at sites of FCC lattice, since to be active for electrochemical reaction there should be percolation of fuel to the reaction site.

Sunde (25) has found the abrupt increase in conductivity at 30% volume fraction of electron conduction particles. Results have been found to be good in comparison with the experimental data of Dees et al. (30). Sunde (26) found the effective properties of the electrode are influenced by the algorithm used to generate random packing of particles. The percolation threshold for conductivity was found to be dependent on the size ratio of the particles and he concluded that the loss of conductivity due to sintering can be explained by the increase in the size of particles and hence the threshold value. They used Random resistor network modelling to evaluate the distribution of current through the anode and evaluated the optimal thickness of electrode depending on the active reaction area and ionic resistance of the electrode. The percolation threshold volume fraction for each phase was in the range of 0.2 to 0.5.

Sanyal et al. (8) have used the fully resolved modelling approach where he discretised the 3D numerically reconstructed electrode at sub-particle scale and solved the transport equations to calculate effective conductivities. Charge conservation equation has been solved for the particle network of electron and ion conducting phase to determine effective conductivities of phases. His results have been found to be consistent with the results reported by Iwai et al. (52) and Wang et al. (75), although his results have shown deviation from effective conductivities values calculated using percolation theory where the Bruggeman factor value of 1.5 (15) is used to represent the tortuosity of phase. Sanyal et al. (8) reported that resolved particle model results are consistent with percolation theory results if Bruggeman factor value of 3.5 is used there.

Effective conductivity of phases in the electrode and effective diffusivity for the gaseous component in the pores have been also calculated by simulating Brownian movements of tracers in the corresponding phases (74, 76, 77). This is done by using random walk Monte Carlo simulation based on mean square displacement method. A tracer (an electron or an ion or a gas molecule) is generated randomly in the phase of interest (electron conducting phase, ion conducting phase or pore) and moved randomly until it collides with different phase particle or to the external surface of the phase in which it is generated and reflects back. The distance covered before the collision of the particle is known as the free path of particle. Random walk Monte Carlo method involves the random generation of initial tracer position, random

trajectory, random free path and random reflected trajectory of the tracer. Bertei et al. (77) gave an expression (equation 2.20) for the normalised effective conductivity in the electrode microstructure constructed by random packing of constituent particles.

$$\tilde{\sigma}_j^{eff} = \frac{\langle R^2 \rangle \psi_j \gamma_j}{2Kn^{eq} \bar{d}_j s} \quad (2.20)$$

Where ψ_j and γ_j represent the volume fraction and the percolation fraction of phase j respectively and \bar{d}_j represents mean particle diameter of phase j , R^2 is mean square displacement of thousands of tracers, s is the distance covered by the tracers and Kn^{eq} is equivalent Knudsen number defined as the ratio of mean free path and the mean particle diameter \bar{d}_j , since Knudsen diffusion is not relevant for charge diffusion in solid phases.

They have also calculated the normalised effective diffusivity (equation 2.21) as,

$$\tilde{D}^{eff} = \frac{D^{eff}}{D_b} = \frac{\langle R^2 \rangle \psi_g \gamma_g}{2Kn d_{pore} s} \quad (2.21)$$

Where, R^2 is mean square displacement of thousands of tracers, s is the distance covered by the tracers, ψ_g packing porosity, γ_g is the pore percolation fraction and Kn is Knudsen number. Bertei et al. (77) verified the random walk simulation method with the FEM simulation results and found good agreement in the results. They evaluated the mean pore size and it is found to increase with porosity in the structure. They further evaluated the percolation of solid phases, and the triple phase boundary for the electrode.

Berson et al. (74) have also calculated effective diffusivity using random walk Monte Carlo method for the reconstructed electrode from random packing of constituent particles. Their results have been found in good agreement with well-known Bruggeman equation $D_e/D_b = \epsilon^{1.5}$ (where D_e is effective gas diffusivity and D_b is the diffusivity of gas in non-porous medium) (78) for the porosities greater than 40%, because Bruggeman equation is derived for the porosities much larger than electrode. Authors proposed a new relation for the electrode porosities of less than 40% and greater than pore percolation threshold as: $D_e/D_b = 1.6 \epsilon^2$.

TPB length value has been calculated for these 3D reconstructed electrodes using analytical methods (23, 29) and numerical methods (8, 23, 35). In analytical approach, TPB and internal surface areas were calculated from the known coordinates of the particles, their size and geometry using relations similar to the ones as explained in analytical methods section 2.1.2. In numerical method approach, three-dimensional grid is applied over the structure and the edges of interest are counted.

Abbaspour et al. (34) found the TPB length to be inversely proportional to the square of the particle diameter and the interfacial surface area was inversely proportional to particle diameter. The effect of composition and electrode thickness was studied on the TPB length. The results have been justified with an experimental study of Ruud et al. (79) for the LSM-YSZ cathode. The TPB length was found to be not affected beyond some critical thickness of the electrode although the polarisation resistance may change due to mass transfer limitations. The effect of electrode composition and thickness was also studied on the isolated clusters of particles. The effect of particle size ratio and composition is studied on TPB length which found consistent with results based on percolation theory.

Golbert et al. (35) also studied the effect of particle size on performance. The performance increase was observed with the increase in the triple phase boundary as a result of decrease in the constituent particle size.

Sanyal et al. (8) showed that the TPB value calculation from DEM packing of structure exhibited sound agreement with TPB values evaluated using analytical methods based on percolation theory (without considering the effect of percolation of phases). However, on considering the effect of percolation, the TPB values show narrower distribution as compared to the percolation model with smaller value for maximum TPB value. The total TPB value for the RPP is comparatively smaller compared to DEM packing and the maximum effective TPB value is considerably lower than the percolation theory based modelling results.

Kenney et al. (23) studied the effect of particle size distribution on TPB length, as the distribution increased the peak value of TPB length decreased because of the influence of larger particles and decrease of the percentage of percolated particles. The TPB length curve became asymmetric as the particle size ratio increased. TPB

results from this model were of the same order as were reported by first experimental study by Wilson et al. (42). The value of TPB length was maximised for the small particles with narrower size distribution. They further studied the pore size distribution which was found to be 2.5 times smaller than was assumed in the literature. 90% of pores were found to be smaller than 300 nm which implies that the transport of components is in the transitional regime, where the mean free path of hydrogen is around 500-600 nm for the temperature range of 750-850 °C and around 340-370 nm for oxygen in the temperature range of 750-850 °C.

Yasutaka et al. (29) verified this properties calculation results with the experimental data from Wilson et al. (80). The TPB values was found to be approximately the same order of $4.2 \mu\text{m}/\mu\text{m}^3$ (42) as found experimentally by Wilson et al. (42) and was verified with percolation models results reported by Janardhanan et al. (81) The trend of the TPB variation with particle size for the modelling results was inconsistent with the experimental results from Wilson et al. (44). Yasutaka et al. (29), considered the effect of pore radii on the TPB and found good consistency with the experimental data for the pore radii = 0.22 μm , radius of electron conducting particle equal to 1 μm and the radii of ionic conducting particle equal to 0.5 μm ; which was approximated to the experimentally studied structure with radius of Ni particle as 2 μm .

2.1.4 Microstructural investigations from 2D images

2.1.4.1 Image analysis and stereology

Previously illustrated methods delineated about the microstructural properties derived using analytical methods and numerical methods, where electrode microstructures are approximated as packing of ion and electron conducting particles, (5, 8, 23, 29, 35, 82, 83). It is worth to mention that earlier described analytical and numerical based methods are based on microstructure approximations, studies are carrying out to depict the microstructural properties from the 2D images of electrodes (such as optical or scanning electron microscopic images). It must be noted that the microscopically derived microstructures of electrode materials, represents actual images of materials whereas analytical and numerical methods delineate the microstructures with errors that were occurred due to the approximation taken during the microstructure construction. Since the imaging methods capture the

actual microstructure, the calculated properties will be accurate unlike the analytical and numerical methods that are based on simplifying assumptions. Microscopically derived microstructural features can be used to extract various microscopic details such as the interface area between the particles, triple boundaries between the particles as well as between the phases etc. Readers must be cautious that X-ray diffraction (XRD) is the technique used to quantify the phases formed in the materials (it is beyond the scope of this review article and interested readers can find information elsewhere) but scanning electron images (along with the energy dispersive X-ray spectroscopy (EDS)) can also be useful in illustrating qualitative information about phases (region of material which is chemically same and physically distinct) and therefore a thorough analysis must be carried out which should address the probably associated errors which may get involved with the microstructures of electrodes.

Detailed microstructural image analysis involves certain steps which include sample preparation, sample imaging and segmentation of the image, which leads to the quantification of microstructural properties such as triple phase boundaries, particles surface area etc. Fuel cells must be kept inside the vacuum (desiccator) in order to avoid the microstructural changes due to atmospheric effect (such as moisture, temperature etc). It is worth to note that surface diffusion of moisture, oxygen etc. may affect the surface morphological features (84), for an example, diffusion of moisture may affect the original porosity and image analysis of this exposed sample may lead to wrong results. Sometimes polishing of samples may cause inclusion of carbon from the typical SiC grinding papers, used in polishing, on the surface morphological feature. Localised morphological changes may occur due to the heating caused during the polishing. This problem can be avoided by using coolant (water is the most common coolant) during polishing steps but this may further lead us to water insertion into the morphology of fuel cell electrode material. This field has been less addressed yet and needs extensive examination, demands extra care during polishing of the sample for précised microstructural analysis because smooth polished surface of specimens is required to minimise the variation of colour in one particular phase in image and to get sufficient contrast between different phases.

Various imaging techniques such as optical microscopic imaging (37, 85), secondary electron microscopic imaging (SEI) (36, 39, 40), back scattered electron imaging (38,

41) (sometimes with SEI) (36) are used to explicate the detailed microstructural investigations. Selection of imaging techniques depends upon the complexities associated with sample such as sample type, shape and stability (material's atmospheric and beam stability). Sometimes specific demand of images (such as image contrast for phase quantification etc.) may need special imaging techniques. BSE imaging technique is the most common technique employed for this purpose. There is a trade-off between the resolution and image size to clearly identify the smallest object in image and also to represent the particle size distribution of components in the sample. For an example, it is mandatory for the microscopist to optimise the magnification for better resolution and in order to achieve the best image, optimisation of the operating condition such as working distance, operating voltage and current etc. are also required. Some modern field emission gun electron microscopes (FESEM or FEGSEM) consist of a range of detectors such as in-lens apart from the conventional electron gun detector. The modern in-lens detector allows efficient collection of electrons and works effectively in low voltage and small working distance etc. In-lens detector allows the microscopist to collect images with the best contrast which is a prerequisite condition for image processing. It is worth to mention that in-lens detector allows us to collect images with good lateral resolution. Variation of work function (energy required to remove electron from material/solid to vacuum) can easily be noticed in the images collected with in-lens detector whereas conventional detector collects topographic images.

Optical microscopic method is most simple imaging technique among the various available imaging techniques as illustrated earlier and has been utilised for Ni-YSZ anode specimen. Work carried out by Simwonis et al. (85), Lee et al. 2002 (36) and Lee et al. 2005 (37) are sound examples of the application of this technique in image processing. Nickel particles exhibit high backscattering (of light) phenomenon whereas insufficient differences in grey intensity for the YSZ and pores (present inherently in electrode materials) is noteworthy, as shown in Figure (2.5).

Lee et al. (36) have compared the information obtained from two different imaging techniques, known as optical and SEM (Scanning Electron Microscopy). Readers must notice that because of the higher refractivity value of Ni compared to YSZ and pore, it is possible to separate Ni from others (pore and YSZ). Pores and YSZ are not differentiated through optical techniques and therefore other imaging methods are

required. This research also highlighted the limitation of optical microscopic technique as far as its application in Ni-YSZ anode is concerned. The pores are separated using SEM imaging. Finally, Nickel is etched out from the sample using HCl (Hydrochloric Acid) to obtain the YSZ phase information. Thus, all the three phases are obtained in different images.

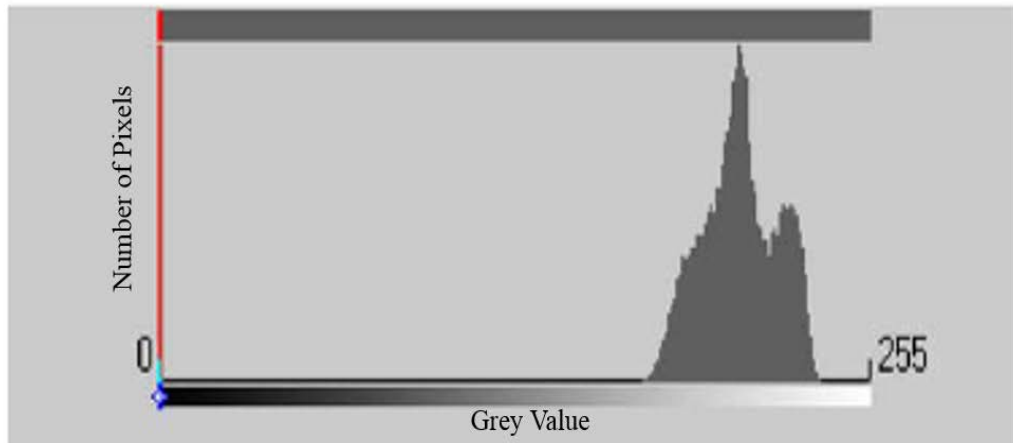


Figure 2.5. Histogram of grey scale value of Ni-YSZ cermet (grey values, 0=black, 255=white). Reprinted with permission from Lee et al. (37). Copyright 2011

Elsevier.

Thyden et al. (39) used low voltage SEM to get the information about constituent phases such as pores, Ni and YSZ. Back scattered coefficient (BSC) is independent of acceleration voltage for voltages greater than 5, but it is found to be dependent on acceleration voltage in the range of 1 to 5 KV. So the lateral SE (Secondary Electron) detector is used to get the contrast between Ni and YSZ, with an acceleration voltage of 1 KV and a working distance of 10 mm. They used in-lens detector to get the contrast between the percolating and non-percolating Nickel phase. Charge contrast has been used to differentiate the different electron conductive phases. The phase contrast was found to decrease with increasing acceleration voltage. Faes et al. (40) also recorded images with similar operating parameters for imaging as used by Thyden et al. (39). High voltage BSE-SEM (Back Scattered Electron-Scanning Electron Microscopy) (around 20 kV) have been used by Monchan et al. (38) and Lanzini et al. (41) to get the contrast between Ni, YSZ and pore in anode sample. High voltage BSE-SEM imaging technique allows electron to penetrate in polishing residue and increases the contrast between phases. It should be noted that this technique poses challenge to overcome low-resolution

problem commonly occurs in BSE imaging due to larger interaction volume of high energy electrons in sample. As discussed earlier, optical images do not intrigue the distinction between microscopic factors such as pores, phases and elemental fraction. It is difficult to get the contrast between phases (including element and pores) through optical imaging technique which exhibits a tolerance limit of 30% in phase separation whereas low voltage secondary electron imaging provides good contrast between Ni and YSZ in anode sample. As described earlier, SEM needs finely polished samples for microscopic and morphological examination.

Image processing operations are performed using assorted commercial and in-house image processing software. Image analysis and stereological relations are used to extract the quantitative information such as (interphase lines between two phases, area fraction of individual phases, triple phase points) from the 2D images and to convert it to 3D structural information (Interface areas, triple phase boundary length, volume fraction of individual phases and pore etc.) (40).

It is noteworthy that stereology is the study of three-dimensional objects by the interpretation of two-dimensional images of the objects. The key to understanding the stereological measurement is the relationship between a three-dimensional structure and two-dimensional section through it. A section plane that intersects the volume shows an area; an intersection with a surface generates a line; and an intersection with a linear structure shows points. Measuring and counting these events provide raw data to estimate the three-dimensional structures.

The above methodologies have been used for microstructural investigation of electrodes including the effect of microstructural parameters on properties and the change in properties after cell operation. Simwonis et al. (85) investigated the electrode degradation and change in its microstructural parameters and properties after 4000 hours of operation. They studied the change in conductivity, particle size and distribution of phases after operation due to coarsening of nickel particles in anode. Lee et al. (36) have found that the overall microstructure change is governed by the nickel coarsening in anode during heat treatment. Lee et al. (36) investigated the effect of compact pressure during anode substrate preparation on the contiguity of individual phases, the nickel and YSZ contiguity is found to increase and the pore contiguity to decrease with the application of compacting pressure. Faes et al. (40)

also studied the anode microstructural evolution with operation time and gave expressions for change in triple phase boundary length due to nickel coarsening. They have found the triple phase boundary length for Ni-YSZ anode of $1.85 \mu\text{m}/\mu\text{m}^3$ which was of the same order as reported by experimental 3-D construction results from Wilson et al. (42).

2.1.4.2 3D reconstruction of electrode from 2D images

2D images are useful but fails to enrich the information about various required microscopic morphological information such as shape (whether spherical, irregular shapes etc.) and size of particles in 3D space and the quantitative microstructural parameters within the 3D confined space. 2D images contain information about the brightness of points and therefore known as intensity images. Readers must note that the discrete element of digital 2D images is a pixel (which is nothing but the information of brightness of smallest piece in image), whereas for 3D images volumetric pixel which is also known as voxel, are used for image processing. Every voxel contains information about discrete brightness values in the confined space and this confined space can be defined as matrix containing information about resolution of SEM image (used for image processing, commonly represented as X*Y) and about the number of images (Z) which get stacked for making 3D structures. Information about the brightness (of grey image) can easily be represented in the form of a histogram. Histogram is nothing but a plot of number of pixels or voxels for each grey images. 8 bits are generally assigned for each pixel. Each bit can store binary information meaning that $2^8 = 256$ combinations of binary variables are available to represent 256 levels of grey components in the pixel. The reduction in bit size reduces the image quality (reducing the number of grey components that can be represented) and affects the information which one may get through image processing. In this segment, the information related to 3D reconstruction and the techniques are been used to get these images for Ni-YSZ electrode materials are presented. An interesting aspect of image processing is that it is employable with coloured images as well because they can be discretised into red, green and blue colour and can be changed into grey images through application of equation(2.22) (86):

$$\text{Grey} = 30\% \text{ Red} + 59\% \text{ Green} + 11\% \text{ Blue} \quad (2.22)$$

Stochastic reconstruction gives the 3D reconstructed image of electrode from 2D image without intensive measurement and processing steps which often get used in experimental 3D reconstruction of electrodes. Suzue et al. (87) used stochastic reconstruction method to generate the 3-D structure of anode from a 2D image. This study utilised the reconstructed image in obtaining the information about anodic over potential of electrode by using Lattice Boltzmann Method (LBM). Weighted average filter's usefulness in obtaining the sharpen grain boundaries was echoed from this study. It is worth to mention that iterative scheme applied by Suzue et al [83], was developed by Yeong and Torquato et al. (88) by assuming the porous media as isotropic. In order to reduce the computation time, integration was only performed for two principle axes. It is conspicuous that the reconstruction was performed until 50 Monte Carlo steps by keeping the cost function constant.

Schemes based on Gaussian filtering are failed to remove the associated errors, particularly for multiphase media and therefore not recommended for Ni-YSZ anode cermets. It must be noteworthy that reconstructed images validity can be checked through linear path function which needs information about number of line segment (of specific length) in specific phase and number of total pixel. The materials with porosity often associate a problem as far as image processing is concerned because elucidation of phases with pores consist the problem of representation of these phases with the pores which is often considered as solid structure floating in space and therefore it needs further treatment for resolving the problem of physically impossible structures' reconstruction (89). Anodic microstructures were reconstructed for three different anode samples, sintered at three different temperatures such as 1300 °C, 1340 °C and, 1400 °C. It was postulated through study that electronic conductivity and ionic conductivity of solid phases increase with increasing sintering temperature. The tortuosity factor was also increased with sintering temperature. The obtained results were commensurate with the experimental data. Increment in TPB density with increasing sintering temperature was perceived and was in the range of 2.4-2.8 $\mu/\mu\text{m}^3$. It was found akin with FIB-SEM (Focused Ion Beam-Scanning Electron Microscopy) results, reported by Wilson et al. (4.8 $\mu/\mu\text{m}^3$) (42).

Lanzini et al. (41) reconstructed the 3-D phase structure of anode using Truncated - Gaussian methods from the 2-D images of phases and spatial correlation function.

One point and two point statistical techniques were used to describe the microstructural properties. SEM and optical images were used for image analysis by using in-house code and software called- CHIMERA (good in managing large sets of images). Images were made free through defects by using various adjustment techniques such as noise filtering, contrast enhancing etc. Image processing made possible to detect various phases including Ni and helped in developing mechanistic insights related to the fuel cell degradation process, often occurs due to Ni agglomeration process.

During the reconstruction, relevant statistical information of the electrode morphology and topology are conserved. Simultaneous reconstruction of three phases could not be possible in this study because of the application of Truncated-Gaussian Method which is applicable for binary phases whereas in Ni-YSZ consists three phases. It is always possible to reconstruct one phase at once by keeping other phases in the background and compiling these all three phases' reconstructed images into 3D space makes TPB calculation of electrode. These structures can be used to determine fluid-dynamic quantities such as tortuosity using the LBM simulation.

2.1.5 Experimental 3-D reconstruction of electrodes

In earlier segments, modelling and simulation techniques for 3D image reconstructions are delineated in detail. Experimental 3-D reconstruction of the electrodes provides dependable and trustworthy information about the actual microstructure present into the anodic material with chances of least probable errors association. This information can further be used in multiphysics simulations. FIB-SEM (dual beam/single beam) and XNT (X-Ray Nano tomography) are prominent methods used for experimental 3D reconstruction. Considering the fact that these methods are time consuming and expensive, these techniques are not been extensively utilised however application of these techniques allow direct examination of the microstructural properties. Although 2D images are capable to examine tortuosity but it may only be accurate for materials consist of isotropic microstructures. 2D images cannot be competent enough in investigating the connectivity of phases, also cannot be utilised in revealing the facts about specific phases' and TPB's connectivity with gas and ion transport. Complexity in sample preparation, tedious procedures of imaging and post-processing of images are among

the few drawbacks of these techniques which are challenges for contemporary imaging science and technology.

2.1.5.1 3D Reconstruction using FIB-SEM

FIB-SEM is a prominent technique which often gets employed for 3D reconstruction of electrode materials. This technique involves the successive SEM imaging of the sample surface after each milling step (performed using FIB). These successively obtained images are aligned and stacked to provide a 3-D structure. The sequence of 3D structure making by FIB-SEM is elucidated in Figure (2.6). The thickness of the slice milled using FIB, limits the depth resolution. The phases, in the obtained images, can be differentiable using different kinds of detectors such as secondary electron detector, EDDBS (Energy Dispersive Back Scattered) detector etc. which are located in predefined positions (see Figure (2.7)). Generated 3-D structure images through FIB-SEM can be used to extract the quantitative microscopic information whose application can further be extended for physical modelling to study the performance of the solid oxide fuel cells. 3D reconstructed images generated using FIB-SEM are comparable with numerical modelling and 2D image stereology results (23, 40, 42).

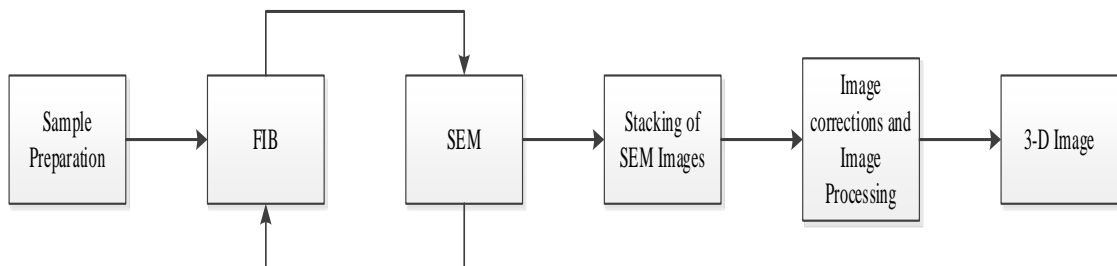


Figure 2.6. Schematic representation of steps involved in 3-D reconstruction of the electrode

The FIB-SEM technique was utilised in SOFC research by Wilson et al. (42) for reconstructing 3D images for Ni-YSZ anode sample having dimensions of $6 \times 5 \times 3 \mu\text{m}^3$ and microstructural properties were evaluated from 3D reconstructed images. The volume percentage of Ni:YSZ were 32 and 68 percentage, respectively, which was akin with initial volume fraction of Ni:YSZ (35.04 and 64.96 %, respectively). Quantification of interface/surface area can be used in revealing fundamental insights about electrochemical and chemical reaction. TPB, as described earlier in this review

as an important factor in deciding electrode performance (including other factors such as phase connectivity, tortuosity and surface area etc.), was directly measured for the first time by 3D structure made by FIB-SEM. Experimentally observed TPB value was $4.28 \mu\text{m}/\mu\text{m}^3$ and further in-depth analysis suggested that 63% of the total TPB was interconnected. This study proposed a method called finite element modelling in analysis of FIB-SEM generated 3D structure and utilised this technique for the rudimentarily evaluation of tortuosity factor which is difficult to be calculated using the stereology technique (for 2D images) because tortuosity calculation principally depends on the analysis of method and place of interconnection of phases in 3D. This study established FIB-SEM as a revolutionary experimental technique for estimating the properties and electrochemical performance of SOFCs. In 2009, Wilson et al. (44) used FIB-SEM 3D reconstruction for the cathode material of fuel cell and reconstructed the 3D structure of LSM-YSZ cathode in order to extract the quantitative microstructural information. The volume fractions of phases in the solid phase were 47.9% LSM and 52.1% YSZ (by volume) and evidently akin to initial solid volume fractions (47.6% LSM and 52.4% YSZ). The agreement in results established FIB-SEM technique equally promising and one of the highly accurate experimental technique for cathode materials' 3D reconstruction as it was for anode materials, postulated earlier in this review.

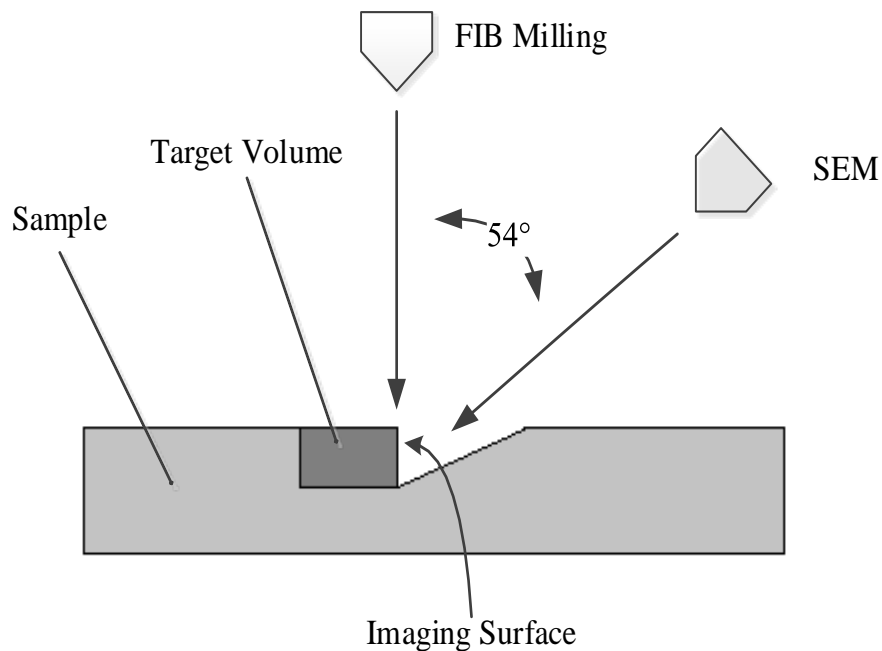


Figure 2.7. Schematic of dual beam FIB-SEM arrangement

However, sample preparation methods, inaccurate FIB operating conditions and procedure inaccuracy in image processing etc. are the sources of errors which one should take care while indulging with data analysis. TPB density of $7.35 \mu\text{m}/\mu\text{m}^3$ was discerned out for 3D image of LSM YSZ and commensurate well with TPB density (1.7 to $6.5 \mu\text{m}/\mu\text{m}^3$) depicted using stereological analysis of 2D images (90) (91). Inactiveness of 28 % of TPB was evidently witnessed including 15% of unknown activity and 57% active TPB, resulted $4.20 \mu\text{m}/\mu\text{m}^3$ active TPB density. It is also possible to examine ion transfer resistance for YSZ using the microstructural parameters (may get through 3D reconstructed image from FIB-SEM) as particularised by Tanner et al. (92) through electrochemical model which was later compared with experimental results obtained using EIS (Electrochemical Impedance Spectroscopy). Finite difference technique was used in solving transport equation and postulated the enriching performance of device by using composite electrode under high intrinsic charge transfer condition. It is noteworthy that deciding rate limiting step could be a rudimentary assumption to proceed with which may later be associated with additional assumption such as ohmic nature, offering legible resistance etc. This study proposed a new way forward for further in-depth analysis.

Another cathode material which was characterised by FIB-SEM 3D reconstruction was LSCF (Lanthanum strontium cobalt ferrite) as studied by Ruger et al. (45). surface exchange coefficient, chemical diffusion coefficient and oxygen ion equilibrium concentration are among the few material's properties which were taken into account in modelling which was done through COMSOL Multiphysics including without adjustable parameters. Physical properties such as gas diffusion, bulk diffusion, surface exchange etc. were incorporated under the constant temperature and pressure

After establishing the importance of FIB-SEM 3D reconstruction for cathode materials, authors wish to portray study which was performed with secondary electron detector. Iwai et al. (52), quantified the microstructural properties for the Ni-YSZ anode using FIB-SEM by incorporating phase contrast imaging through SE detector. The reconstructed volume of the samples was $18.6 \times 8.432 \times 6.2 \mu\text{m}^3$. The volume fraction of phases obtained from 3D structure was in good agreement with the initial volume fraction of Nickel and YSZ. However, the variation in results was about $\pm 5\%$ due to smaller sample size. Using large sample size may lead to low

resolution. TPB length was compared with two different measurement techniques named volume expansion method and centroid method. Readers must note that the comparison among various methods of TPB measurement is not explicitly addressed and it may be considered as a future research area. It is noteworthy that thermal expansion coefficient of anodic material with respect to electrolyte and therefore volumetric expansion method for TPB is competent to elucidate real-time phenomenon. It has been highlighted in this review that TPB is the active sites for electrochemical reactions and which may further be affected by porosity, grain diameter, etc which influence the cell performance and durability. Readers are encouraged to utilise other contemporary methods in evaluation of these parameters for an example, XRD based Rietveld analysis method may be an alternative to predict grain size of phases (provided phases are crystalline in nature). In this study, TPB value was 2.487 μm from the volume expansion method and 2.556 μm from the centroid method, which were almost similar. It is noteworthy that the TPB values obtained using these methods were quite different in comparison to the values obtained by Wilson et al. (42) and Shearing et al. (46) but were in good agreement with the stereology analysis (for 2D images). Tortuosity factor (for all phases) was also examined using random walk method and Monte Carlo Method The tortuosity factor for the pore phases evaluated by Iwai et al. (52) was in good agreement with the results obtained by Wilson et al. (42).

A lot of effort has been made by instrumental scientist regarding improving the quality of data generated for 3D image reconstruction using FIB-SEM. Shearing et al. (46) proposed a modified efficient method for maximising the quality of raw data obtained by ex-situ reconstruction. Method involves lifting out a sample from the anode structure using FIB which was further addressed with milling followed by imaging. Reconstructed sample volume was $6.67 \times 9.39 \times 1.2 \mu\text{m}^3$ using the single beam technique with SE imaging detector. Since the sample size may affect the resolution of image, experimentalist must take this into account. This method becomes time consuming considering the fact that multiple steps are involved but provides improved quality of data for 3D reconstruction. It should be noted that the voxel size may also affect the time requirement which can further be correlated with data accuracy. Another reconstruction of sample volume $20 \times 15 \times 10 \mu\text{m}^3$ was performed using the dual beam FIB-SEM and imaging is performed using Energy

selective Backscattered (ESB) detector. This proposed lift out technique was a good alternative in reducing the streaking, shadowing, charging and re-deposition effects which commonly occur during imaging and affects final results. Readers must note that charging can be avoided by using different speed of image acquisition. Another method could be to use different acquisition methods such as instead of using frame averaging which often takes time but produces good data sets, line averaging can be an effective alternative. For cell materials which are getting charge extensively or not producing good images, may undergo with Pt or Au coating before imaging but it must be noted that image analysis results may get affected because of coating especially porosity, morphological characteristics etc. even though the coating will be in the range of few nm. This is a biggest challenge for imaging and instrumental scientist to develop a sophisticated method for quantitative image analysis. Further to the effort for making the efficient sampling technique, Vivet et al. 2011(53) made an effort to optimise sample preparation and effort was further extended to optimisation FIB-SEM procedure in order to obtain a high quality 3D structure of the electrode. Sample volume of $8.66 \times 9.79 \times 11.41 \mu\text{m}^3$ was reconstructed which elucidated the presence of 99.8% 99.1% and 87.4% of pore, YSZ and Nickel percolation in the structure respectively. Specific surface areas of Pore, YSZ and nickel phases were observed as 4.27, 4.24 and $2.33 \mu\text{m}^2/\mu\text{m}^3$ respectively. About 50% of nickel surface area was assigned as pore region which could be used for surface catalytic reactions. Measured TPB density was $11.2 \mu\text{m}/\mu\text{m}^3$, out of which, 66% was active with affirmed effective TPB of $7.4 \mu\text{m}/\mu\text{m}^3$. Tortuosity for all the phases was evaluated and the intriguing phenomenon of directional depending difference in tortuosity was noticed. Interestingly ionic conductivity was quite isotropic in nature and was around $1.04 \times 10^{-3} \text{ S/cm}$. Extensive future experiments, describing the role of directional texture in tortuosity could be helpful in discovering the mechanism related to this phenomenon and could further be assisting in durable cell manufacturing by improving the cell life.

Reconstruction by single beam FIB, TPB density was $10.58 \mu\text{m}/\mu\text{m}^3$ with 51% of the total TPB length was found to be percolating whereas reconstruction performed using dual beam FIB exhibited $9.36 \mu\text{m}$ as a TPB with 45% of total TPB length was found percolating. The difference in this percolation values are attributed to the sample size and therefore results were not affirmed through other studies such as

study done by Wilson et al. (42) but were comparable with the results obtained by Golbert et al. (35).

Shearing et al. (47) reconstructed the sample volume of $6.68 \times 5.04 \times 1.50 \mu\text{m}^3$ for the SOFC anode using FIB-SEM and quantified the TPB density which was around $13 \mu\text{m}/\mu\text{m}^3$. Microstructural quantities calculated using 3D reconstruction were used in developing the electrochemical model. Exchange current density, used as a fitting parameter in comparing the results with impedance spectroscopy results. It was depicted that length specific exchange current densities for hydrogen electro-oxidation were 0.94×10^{-10} , 2.14×10^{-10} , and, $12.2 \times 10^{-10} \text{ A}/\mu\text{m}$ at 800, 900 at 1000 °C respectively. Results were consistent with experimental study reported by Bieberle et al. (93). This supports the applicability of 3D image processing as an alternative scientific method to evaluate the electrochemical phenomenon. As briefed earlier in this review, degradation of cell includes various factors such as agglomeration (segregation) of Ni in Ni-YSZ, inappropriate thermal expansion coefficient (with respect to electrolyte) etc. Development of thermomechanical stresses during cell operating conditions was assigned as another probable influential factor which affects cell durability. Clague et al. (49) investigated this factor's (thermomechanical stresses developed during cell operation) effect in the degradation of SOFC. FIB-SEM 3D reconstruction technique was employed for investigating this factor influence over the degradation of cell. It is noted that in earlier studies described in this review, stresses' effect was not been delineated using 3D reconstruction method. Reconstruction was done for the structure of a screen printed anode in an electrolyte supported half-cell. The Finite Element (FE) modelling is done for the reconstructed volume ($6.68 \times 5.04 \times 11.50 \mu\text{m}^3$). Stress predicted by the FE model for nickel was more than the yield strength of nickel and maximum stress was observed at the interface between Ni and YSZ. This study portrayed the relevance of interfacial characterisation, particularly for Ni-YSZ cermet. Authors encourage researchers working in this area to further explore this to get a deeper mechanistic understanding about the reason for generation of stresses at interface from molecular point of view. However, crystallographic lattice mismatch and effect of dislocation density in the interfacial stress generation could be assigned as future promising area of research. Area can be explored with various experimental techniques such as high resolution transmission electron microscopy (HRTEM), XRD etc. Further to this, interfacial

mathematical modelling tools such as Miedema model etc could be a promising way to deal with the problem. Interested readers are encouraged to explore this further as it is beyond the scope of this review,

Reconstruction was further explored by Shikazono et al. (51) using FIB-SEM technique with a sample volume of $18.60 \times 8.43 \times 0.20 \mu\text{m}^3$. Observed TPB lengths were 3.946, 2.979 and, 2.556 μm using three different methods, namely, the edge length, mid-point and centroid methods, respectively. Reader must note that earlier in this review, Comparing various TPB measurement techniques is assigned as future promising area of research by authors of this article since area remained less explored yet. They developed an electrochemical model including the electrochemical reaction at TPB along with ionic, electronic and gaseous component transport using the LBM.

Vivet et al. (54) investigated the effect of nickel concentration on the microstructural recall that in the earlier section of this review, authors were able to describe the effect of segregation (agglomeration) of Ni on fuel cell performance and therefore in this regard, the study conducted by Vivet et al assisted us in developing understanding about the degradation process of fuel cell. Specific surface area of phases and interfacial surface areas between phases were calculated. There was a sudden increase in electrical conductivity while the nickel volume fraction increased from 16 to 26 %, which could be due to the difference in the Ni tortuosity which is directly related with electrical conductivity. Importance of microstructure difference may also catalyse this phenomenon, at the same time, effect of particle size of powders, particle distribution, porosity etc. cannot be discarded. Simple system like metal-insulator, achieving a specific concentration value (33.3 volume %) encourage electronic threshold to occur. Authors emphasise the application of Effective Medium Percolation Theory (EMPT) in predicting the electrical threshold (considering randomised particle system). It is worth to mention that no universal theory is available describing this phenomenon and therefore EMPT holds significance and required immediate attention.

As described earlier, relevance of microstructure cannot be discarded and therefore effect of microstructure was extended to different materials as well apart from Ni-YSZ. Holzer et al. (55) reconstructed the sample volume for Ni-CGO (Nickel-

Gadolinium doped ceria) anode with a graded microstructure and quantified the microstructural parameters from the structure, values were comparable with modelling results. However, small variation in values noticed which was due to the over simplification of structure during the modelling studies. The inter-particle interactions (forces) lead to complex microstructure formation that is quite different from the modelled micro-structure. Degradation in the electrode micro-structure after operation of cell was also studied to get a better comparison. Readers must recall that microstructure is an important parameter which affects the degradation of cell with simultaneous creating hindrance in electrical conductivity. Therefore we recommend to perform EMPT, interfacial thermodynamic calculation as well as experimental microstructural observation to reach out at collective conclusion. In the initial 200 hours of operation, the TPB value decreases very rapidly due to coarsening of nickel particles. Since Ni particles get coarsened, its effect on electrical conductivity may lead to the understanding of the effect of metal concentration on the threshold electrical value. We believe that the study could clarify two important phenomena: (1) phenomenon related to the electrical threshold value achieving and effect of Ni coarsening on it (2) shape and size of grain's effect on electrical threshold value and whether the grain coarsening phenomenon may change the concentration of metal at which electrical threshold occurs. Ni-GDC (Nickel-Gadolinium-doped ceria) anode functional layer was further explored by Kang Take Lee et al. (94) through FIB-SEM 3D reconstruction where sample had varying composition of NiO. The microstructural parameters were quantified from the 3D structure and these parameters were consistent with the initial composition. Experimentally observed porosity was little less than the theoretical value, which can be attributed to the shrinkage of the anode during reduction of NiO to nickel. Microstructural properties examination lead us to the intriguing condition where TPB was maximum (was obtained at 1:1 volume fraction of Ni-GDC). Similar fuel cell material (Ni-GDC) was investigated by Kishimoto et al. (95) where reconstruction of material (nickel infiltrated Gadolinium doped Ceria (Ni-GDC)) anode. The microstructural properties were quantified from the 3-D structure considering the fact that GDC behaves as electronic and the ionic conductor. The electrochemical active region will be the double phase boundary of the GDC and the pore phase. The quantified properties were further used in one-dimensional model in studying the effect of the microstructure on performance and durability (degradation) of cell. It was culminated

through study that increment in the electrochemical double phase boundary helped in improving the performance of cell.

Until now, we have evaluated the FIB-SEM method for 3D reconstruction method and application of 3D images in getting various physical parameter, which is relevant in describing various electrochemical and other mechanistic phenomenon but operation involved in 3D imaging also holds significant relevance. Gunda et al. (56) investigated the effect of various image processing operations involved in the 3D image of the structure. The study involved the reconstruction of sample volume for LSM cathode. Image processing operations like thresholding and median filter operations hold significant importance and contribute to the values of porosity and internal surface areas by 33% and 25%, respectively. The properties evaluated from the 3D structure were anisotropic in nature as evident from earlier literature. This could be due to the size of the reconstructed sample and the procedural steps involved in FIB milling and imaging.

Kishimoto et al. (57) reconstructed the Ni-YSZ anode microstructure where observed TPB density was between 2.37-2.49 $\mu\text{m}/\mu\text{m}^3$ for three different samples. These densities were smaller than the earlier reported results in the literature. This difference can be attributed to the difference in the sample preparation methodology (as described earlier, voxel size as well as sample volume may affect the results) and the approach used to quantify the properties. It was observed that both very large and very small surface area to volume ratio resulted in large tortuosity factor and this (surface to volume ratio) can further be optimised through optimising the composition of phase. The evaluated properties were further utilised for one-dimensional numerical simulation for studying electrochemical performance. The predicted overpotential from the model agrees well with the experimental data in low steam concentration (3%) for hydrogen fuel at high temperature 1000°C but deviates at high steam concentration (20%) and lower temperatures (800-900°C). This may be due to the anisotropic nature of calculated properties from the reconstruction.

We have discussed the effect of thermally developed mechanical stress (also known as thermomechanical stress) on the cell performance and its characterisation through FIB-SEM reconstruction. In the similar manner, Kwok et al. (58) investigated the steady-state creep behaviour of Ni-YSZ in SOFC by using the reconstructed

microstructure from FIB-SEM technique. They investigated the effect of microstructural properties on the mechanical strength of composite. Intriguing study culminated about the increment in creep factor (by a factor of 8-10) with increasing density of YSZ.

2.1.5.2 3D Reconstruction using X-ray Tomography

This method involves reconstruction of the 3-D volume using X-ray as an investigative agent where the series of 2-D projections are obtained during sample rotation from -90 to +90 degrees. It is a non-destructive technique which makes it a suitable technique for many research areas like nanomaterials, semiconductors, environmental science and life sciences. Readers must recall that FIB-SEM is a destructive technique and it may not be possible (if one wants to analyse same region of interest (ROI)) to reuse the sample again for further analysis later. Compared to SEM, XCT (X-ray Computed Tomography) uses x-rays instead of electrons, application of x-rays offers large penetration depths into the material and supplies more reliable 3-D image data at resolutions of tens of nanometer scale without destroying the sample. Schematic of XNT (X-ray nano-tomography) is depicted in Figure (2.8) which illustrates the application of X-ray energy source, typically Cu source gets used, (Cr and Co are another energy sources which get used), energy filter (often used for filtering out the unwanted energy, decided based on the absorption edge of material), rotation stage which allows material to rotate and detector (various detectors get used, delineated later in this section).

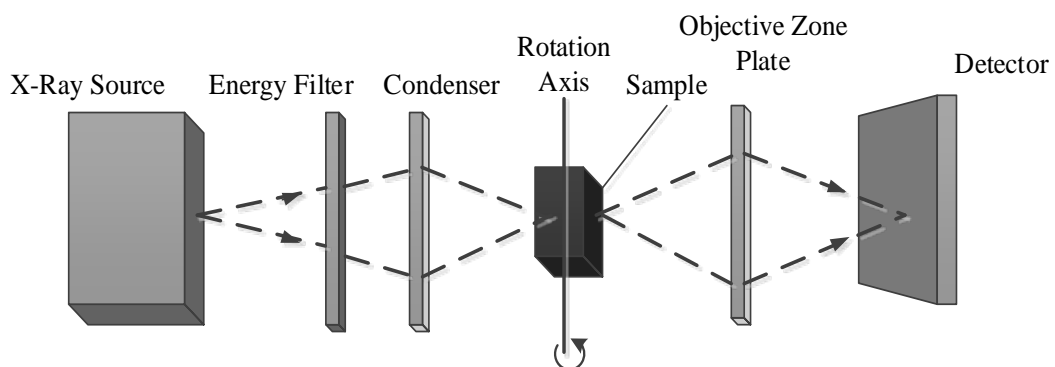


Figure 2.8. Schematic of XNT (X-ray nano-tomography)

XCT and XNT have been utilised for 3D reconstruction and in this section, we will be compiling the studies where these techniques were used. Izzo et al. (96) used X-ray CT technique for SOFCs to reconstruct the anode (Ni-YSZ) microstructure at the resolution of 42.7 nm scale by using 8KeV Cu $K\alpha$ beam. The porosity and tortuosity parameters were quantified from this structure. The LBM was used in studying the transport of different gaseous components in the structure. This technique is specialised in determining the internal porosity and it was found that 98% of pores were interconnected. However, the study was failed in distinguishing solid phases in the anode which means that technique was fairly good in evaluating the interconnectivity of pores whereas was not able to provide any significant information related to solid phase. In this study, investigation on the effect of sample size in porosity calculation was explored and it was found that porosity value becomes independent of sample size after a sample size of 50 voxels. It is worth to mention that effect of voxel size on the 3D reconstruction as well as on physical properties such as tortuosity, TPB etc. were described whereas it would be intriguing to explore the minimum voxel size where these properties may become free from the function of voxel size and study must be directed in this regards. Pore size distribution from this method was found to be consistent with mercury intrusion porosimetry results (96).

XCT was further used to reconstruct the anode sample (Ni-YSZ) of size $2.4^3 \mu\text{m}^3$ at a resolution of 38.5 nm by Grew et al. (97). The distinction between solid phases made possible in this study and which further assisted in calculating the interphase surface area, tortuosity, contiguity and, triple phase areas. Results were consistent with the earlier result reported by Wilson et al. (42). Microstructure induced relative load distribution (MRLD) was used to quantify the resistance losses in the electronic and ionic carriers within the microstructure. It was found that necking of the particles results in increase of the resistance losses. As illustrated earlier about the Ni coarsening's effect on the electrical properties in Ni-YSZ. It would be interesting to examine the phenomenon of necking even at the metal (such as Ni) concentration of 33.3% where electrical threshold should occur (according to theory, earlier described in this review) and X-ray CT would be a prominent method to characterise solid phase as described in this study.

Nelson et al. (98) quantified the SOFC cathode (LSM-YSZ) properties using XNT (X-ray nano-tomography). XNT measurements utilised cylindrical sample (10 μm diameter and 15 μm height), it must be noted that samples were prepared using FIB-SEM. Cylinder is the ideal geometry for the X-ray tomography measurement (it is true even for nano and micro tomography techniques) because this geometry provides uniform cross section for X-ray transmission. 3D structured obtained using XNT were further correlated with FIB-SEM 3D reconstruction. Near edge differential absorption contrast for XNT and EsB for FIB-SEM were used for microstructural and elemental mapping respectively. The reconstructed microstructure obtained using TXM (transmission X-ray microscopy) images was at 45 nm resolution and that from FIB-SEM was with 10 nm resolution. Although both samples were not from same location of the cathode, they represented the bulk structure of cathode. The results obtained using both techniques were comparable for phase size distribution, volume fraction of phases, and contiguity of phases, except for contiguity of LSM. Imaging resolution was assumed as a culprit for this inconsistency and demands further investigation to affirm the assumption. This study highlighted the application of XNT for obtaining accurate 3D images without samples' destruction because as mentioned earlier, XNT is non-destructive techniques, providing comparable results with FIB-SEM.

Nelson et al. (62) further used XNT to study microstructure evolution in the SOFC anode after operating it for different time durations as earlier mentioned different operating condition may and operating time affects tortuosity and TPB. The effective TPB length, contiguity, interphase surface area etc. are measured using XNT technique, applied after different operating times. It is noteworthy that results were comparable with results by Faes et al. (40).

Harris et al. (59) used XNT coupled with X-ray Absorption Near Edge Spectroscopy (XANES) in studying the sulphur poisoning of SOFC anodes due to the absorption of sulphur on the nickel surface. It is worth to mention here that XANES is a prominent X-ray absorption technique. XAS allows us to understand the surface properties at molecular level. It includes two major techniques: (i) XANES and (ii) extended X-ray absorption fine structure (EXAFS). EXAFS works in the range of 1 keV above the K spectrum because of the scattering of electron by atoms whereas XANES works beyond the absorption edge where multiple scattering of

photo electron provides information about atomic clusters. In a simplified manner, readers must note that local structural information can be obtained from EXAFS whereas cluster based information can be obtained through XANES (99). Sulphur poisoning results in lesser electro-chemical active area for the reaction than the samples without sulphur poisoning. This technique enabled us to understand the sulphur poisoning mechanism through direct monitoring of the process. Harris et al. (63) further used this technique to quantify the microstructural properties after sulphur poisoning and it was found that TPB density decreases by 67% due to formation of Ni-S on the nickel surface. It can further be confirmed through FTIR (Fourier transformed infrared microscopy) as well as Raman spectroscopy and it is recommended for future experimental design as spectral mapping obtained by Raman spectroscopy can be used for image processing too. Reconstruction was performed using Fourier transform based gridrec method that can achieve higher accuracy than the filtered back projection.

2.1.6 Future outlook and conclusions

The microstructural characterisation of SOFC electrodes using analytical, numerical and 3D reconstruction methods are reviewed in this work. While the 3D reconstruction using numerical and experimental methods provide realistic information for properties evaluation and performance simulation of electrodes, analytical approaches have been widely used due to their simplicity and give average properties for the electrodes. 2D and 3D image analysis and stereological examination are currently being performed for in-depth microstructural properties analysis of electrodes. These techniques are capable of delineating the various routes of material degradation occurring in the electrodes. Results from analytical methods have been found generally in good agreement with experimentally evaluated results. Various microstructural properties such as triple phase boundary length, tortuosity of phases in the electrode are the main characterisation parameters for the performance evaluation which have been described in detail in this review through various studies. 3D reconstruction using numerical methods are comparatively low-cost techniques compared to experimental reconstruction techniques but needs certain advancement specifically regarding particle shape and size assignment method, accurate examination of porous phases along with the solid phases, prediction of interconnectivity of porosity, arriving an approximation to depict the real structure of

the electrode. Modelling of fuel cells at nano and microscales can be effectively accomplished through numerical models such as Lattice Boltzmann model (LBM) which can be considered as a bridge between the continuum and discrete methods. Analytical electrode models disregard the effect of electrode compositional and structural heterogeneity. Inherent constraints associated with the analytical models such as shape of the particles (spherical), assumption related to the connectivity of pores (which may not be the case in real time phenomenon) etc. could generate misleading results whereas parameters such as porosity (which is considered as dimensionless) is easy to calculate by LBM method. The future development in analytical modelling must consider the incorporation of the effects of particle size, shape, porosity, graded electrodes etc. on the electrode's performance. These properties are used in various other structure property based characterisation such as electrochemical performance analysis (largely depends on compositional and microstructural features of electrode), durability of cell (factors affecting durability has been extensively addressed in this article), mechanical strength determination, creep performance of electrode materials (as discussed in this review). Experimental reconstruction techniques are the direct way for properties estimation but these techniques are time intensive and costly. However various methods have been suggested in this review to overcome this problem.

Experimental techniques like FIB-SEM and TXM are also discussed. Considering the fact that TXM is a non-destructive approach for electrode reconstruction and can also be used for real-time in-situ analysis of performance degradation of cell (electrode materials), it needs extensive research to make it commercially viable and experimentally user friendly (must allow performance evaluation of electrode materials under a range of constrained atmospheres and an in-situ manner). Imaging and image processing techniques play a vital role in elucidating the microstructure of the SOFC electrodes. The obtained data is useful not only for experimental characterisation of the microstructure, but also serve to validate the numerical models. Properly validated numerical models can provide great insights into the parametric effects on the microstructure and can aid in the optimisation of the electrode microstructure. However, the steps of imaging and image processing can introduce a lot of error into the outcomes due to the large number of factors influencing them. Types of samples (such as X-ray sensitive samples, heat sensitive

samples etc.), roughness of the surface (in case of SEM and EDS based characterisation), shape of the samples etc. are important aspects in the experimental characterisation of samples for 3D image processing. X-ray sensitive samples may experience phase transformation while exposed to X-rays during X-ray CT or XNT characterisation. Samples with rough surfaces are always considered problematic due to the scattering of X-rays or electrons from the surface and lead to poor signal to noise ratio. This problem becomes severe in case of XNT, SEM and EDS characterisation. It is worth to mention that standard operating procedure is different for each instrument and that needs to be followed in order to acquire best images. These techniques are ex-situ techniques and may cause moisture ingress during characterisation which sometimes can lead to misleading results in 3D image processing. Therefore, the development of in-situ characterisation techniques is required.

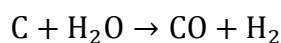
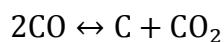
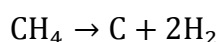
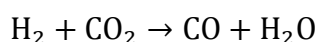
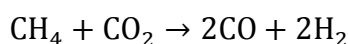
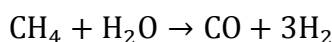
Overall, the micro-modelling techniques coupled with the experimental evaluation of various microstructure parameters using 3D reconstruction techniques jointly provide a good insight for the cell performance degradation mechanism. In this review, the authors also suggested future pathways for research using various other techniques such as XRD, FTIR, and Raman spectroscopy that would enable the micro-engineering of the SOFC electrodes for optimum performance.

From the above literature survey, it is observed that the anode microstructure plays an important role in anode performance. Anode microstructure is greatly influenced by the microstructural parameters and poisoning of catalytic material in anode. There are various modelling studies (14, 15, 18, 20, 22, 35) to investigate particle size effect on cell performance as partly discussed in above sections. Suzuki et al. (100) have experimentally investigated the particle size effect on cell performance and, it has been observed to be greatly enhanced with smaller anode constituent particle size and porous microstructure. But, there has been no experimental investigation to correlate the effect of particle size on microstructural properties. Based on the knowledge developed from the above literature review, 2-D image analysis is a fast and efficient method to experimentally investigate microstructure while there are number of microstructures generated from particle size variations. Therefore, we will be using 2-D image analysis techniques to probe particle size effect on microstructural properties. Previously used image acquisition and image

segmentation techniques have always been challenging as discussed in section 2.1.4.1 and as discussed by Fu et al. (101). As suggested from Lanzini et al. (41) we will also be exploring the EDS maps to help in identifying the individual phases in image and feature based classification for image segmentation purposes.

2.2 Carbon poisoning in SOFC anode

SOFCs have the advantage of using hydrocarbon fuels (natural gas, biogas, biofuel etc.) due to their high operating temperature (102, 103). Natural gas is the most widely used energy source for various applications due to its low cost and natural abundance (104). Methane and carbon mono-oxide are the main components of natural gas and biogas fuel. The use of hydrocarbon fuels also poses some challenges due to the impurities that can result in electrode material degradation and cell performance degradation (105, 106). Apart from these contaminants in the fuel, the carbon component in the hydrocarbon fuel leads to carbon poisoning problem in the most widely used nickel based anodes. This phenomenon has been investigated by several researchers in the past (2, 107-113). While using methane as the fuel, the possible chemical reactions in SOFC anode are described below (102, 114). Nickel acts as an excellent catalyst for carbon formation in these reactions (115).



Carbon formation over nickel catalyst has been explained by dissolution-precipitation mechanism where carbon containing molecules dissociates on metal surface and forms carbon atoms which dissolve and diffuse through the metal bulk and precipitate from the other side of metal (115). There are several quantitative and qualitative methods such as temperature programmed oxidation (TPO), temperature programmed reduction (TPR), Raman spectroscopy and microscopic imaging to investigate the type and amount of carbon formed. The morphology of carbon

formed is found to be dependent on the operation temperature and reacting gaseous species. J. Sehested (110) found three types of carbon morphology, namely, pyrolytic, whisker and encapsulating depending upon the type of hydrocarbon fuel used. He and Hill (111) found that the whisker carbon formation is dominant till 600 °C and at higher temperature carbon gets dissolved in nickel particles resulting in expansion of anode. Carbon formation can be reversible and irreversible depending upon the fuel composition. Reversible carbon can be removed by the addition of steam in the fuel and by the polarisation current. Irreversible carbon cannot be removed by cell polarisation and leads to cell performance degradation (116).

Carbon formation covers the active catalytic sites for chemical and electrochemical reactions and leads to reduction in cell performance (105, 108). This carbon formation also reduces the porosity in the structure leading to mass transport resistance for gaseous species. There have been several experimental and numerical investigations for carbon deposition effect on the microstructural properties and cell performance. (105, 109, 117) (118). Researchers have investigated different mechanisms to deal with carbon deposition phenomenon. External and internal steam reforming of methane has been used to convert the methane to syngas fuel to avoid the carbon deposition. Several researchers have done thermodynamic studies to determine the fuel composition and operating temperature to avoid the carbon formation conditions. Sasaki and Teraoka (119, 120) showed in their equilibrium studies that by varying the amount of steam to fuel ratio, carbon deposition can be controlled. Thermodynamically, for the steam to carbon molar ratio of 1.5, there will be no carbon formation, but will also lead to reduction in fuel efficiency. Addition of other gases like steam, H₂, CO₂, O₂ etc. will also result in decrease of carbon deposition (121-124). Laosiripojana and Assabumrungrat (121) reported in their equilibrium studies that for steam/carbon ratio of 3, at temperature greater than 950 °C, there was no carbon deposition. Wang et al. (124), described that the addition of ammonia to the fuel changes the kinetics of the reaction. 33 % of ammonia added to the fuel resulted in decrease of carbon formation rate by 71% at a temperature of 700 °C. Alternate electrode materials and modification of catalyst activity of nickel have been suggested by several researchers. Kim et al. (125) described Cu as alternative to Ni in the anode during hydrocarbon reforming. Takeguchi et al. (126), showed that the Cao-modified Ni-YSZ anode is resistive to carbon deposition without affecting

the reforming capability. Macek et al. (127), described the effect of different anode composition and synthesis processes on carbon deposition. Different anode materials were prepared by sol-gel and combustion synthesis process with varying composition and amount of dopants. Anode material synthesised by combustion synthesis process doped by Cu and Ag (CS-50-Ag-Cu) was found to be most resistant towards carbon deposition compared to other investigated anode materials.

Fuel cells operating under polarisation are comparatively stable under the operation with hydrocarbon fuels. Researchers have proposed oxygen ion transported from the cathode side to anode side under polarisation reacts first with the carbon deposited at the electrochemically active sites, then with carbon formed at ion transporting phase in electrode and lastly with the carbon formed at the nickel surface (128). Koh et al. (116) determined the critical current density of 85 mA/cm^2 above which no carbon deposition was observed. Lin et al. (129) also suggested carbon deposition prevention with increased oxide ion flux through the anode. Horita et al. (130) have proposed a model for the removal of carbon under polarisation. Studies from the direct carbon fuel cell research also suggest that electro-oxidation of deposited carbon on Ni-YSZ anodes occurs (104, 131, 132). With the control of operating conditions and fuel composition, Ni-YSZ anodes can be used for stable operation of SOFCs.

As discussed above, carbon poisoning of nickel catalyst while using hydrocarbon fuels has been the main cause of cell performance degradation. There have been several approaches to mitigate carbon formation in anode such as alternative anode material development, controlling cell operating conditions and fuel composition. Carbon formation in anode affects microstructural properties such as electrochemical active area (133), conductivity (134) and porosity (133). There have been modelling and experimental studies to investigate carbon deposition effect on microstructural properties (108, 117, 133, 134). But, there is no modelling study to quantify the effect of carbon deposition on microstructural properties. Here we will be using percolation theory and coordination number theory to relate the carbon deposition effect with anode microstructural properties.

2.3 Anode performance modelling

In the literature, several approaches are taken to investigate the effect of microstructures on electrode performance. The effect of structural parameters on activation, ohmic and concentration polarisations have been investigated by several researchers (8, 25, 77, 135). Costamagna et al. (14) firstly developed the micro-model to relate microstructural parameters with electrode performance, where they have investigated the effect of electrode thickness on the ohmic polarisation, although they have ignored the concentration polarisation in the anode and assumed the uniform temperature and current density in the cell. These kinds of electrode micro-model further developed to optimise electrode performance while considering the concentration polarisation in the anode using Fick's law or Dusty gas model and also for the multicomponent mass transport in anode side for fuel mixtures (13, 15, 20, 83, 136, 137). In such models, the average value of microstructural properties was used to evaluate electrode performance. However, the electrochemical active area, pore size and tortuosity vary inside the electrode domain and depend on the microstructure. Simulation studies have been conducted using LBM approach for the numerically reconstructed 3D electrodes and experimentally reconstructed electrodes (which capture the spatial details of the microstructure) to analyse charge and mass transport in SOFC anodes (138).

Joshi et al. (139) have used the LBM modelling approach to investigate the mass transport of hydrogen fuel in the anode and the effect of anode porosity on the distribution of reactant and product species for hydrogen fuel. Chiu et al. (140) from the same research group have further developed the model for multicomponent species transport for hydrocarbon fuels and have considered the heterogeneous chemical reactions and electrochemical reaction in the anode at the respective catalytic active sites. Guo et al. (141) used LBM modelling approach to study the effect of thermal cycling on the anode microstructure and its influence on mass transport of species and electrochemical reaction. Andaluz et al. (142) investigated the porosity gradient effect in the anode microstructure on the mass transport of species and the availability of species for electrochemical reaction at the electrode-electrolyte surface.

CFD is an alternative approach that is widely used to simulate mass transport in electrodes. Various CFD studies have been performed considering the chemical and electrochemical reaction involved in anode volume to investigate the species distribution (143-149) and the effect of average microstructural properties (150) on the performance. Till now, CFD simulation studies have been mostly used for the cell performance simulation using the average microstructural properties such as porosity, tortuosity, active chemical and, electrochemical area. CFD modelling at the microstructural scale will be comparatively less computational intensive than LBM and provides the opportunity to multi-scale modelling by combining with the cell level models. In this work, we use the CFD technique in anode microstructure to study the effect of local heterogeneity and microstructure on the mass transport and species distribution in the anode.

Chapter 3

Microstructural characterisation of Ni-YSZ anode

3.1 Introduction

The reliability and performance degradation of SOFCs are affected by the microstructural properties of its components. The microstructural properties of the electrodes include the electrochemical active area, surface area of constituent phases in the electrode, tortuosity and effective conductivities of the electron and ion conducting phases. These properties are controlled by the structural parameters such as volume fraction, particle size ratios and the particle sizes of constituting phases. Our focus in this study is on the Ni-YSZ anode, which are the most commonly used anodes for SOFCs. We investigate the effect of nickel particle size on anode microstructure and its structural properties. Improvement over imaging, image segmentation and image analysis techniques for the SOFC anode are also proposed.

Several research groups as discussed in Section (2.1.4.1) have used the sample imaging and image analysis to characterise the electrode microstructure. Different imaging tools and techniques have been used to get quality images of electrodes and to segment the image into its constituent phases for further analysis. Many commercial software and individual codes have been used for image processing and image analysis operations. Image analysis and stereological relations have been implemented to extract the 3-D quantitative microstructural information from the specimen 2D images.

Previously optical microscopy is the simplistic approach that has been used for anode characterisation and quantification. This imaging technique requires the sputtering of interference film during sample preparation process to differentiate nickel, YSZ and pore in the anode and it is very tedious to control the thickness of interference film and to optimise it. Further, researchers have used low voltage-SE and high voltage BSE imaging technique that require sophisticated sample preparation procedures and smooth polishing to minimise the greyscale intensity variation within individual phases and it is challenging to segment the image into its constituent phases with large grey intensity variation (Figure 3.7). In this study (Figure 3.1), we propose BSE imaging of the specimen along with energy dispersive x-ray spectroscopy (EDS)

maps to identify the phases and segment the specimen image into constituent phases overcoming the difficulties that we face during segmentation of images obtained from SE and BSE imaging (Figure 3.7). Machine learning techniques have been used in this study for image segmentation.

The main contributions of this chapter are listed below:

- We investigate the effect of nickel particle size on microstructural properties.
- We propose EDS maps combined with BSE imaging to segment the Ni-YSZ anode image into its constituent phases.
- We illustrate the application of machine learning tools for image segmentation in Ni-YSZ anode.

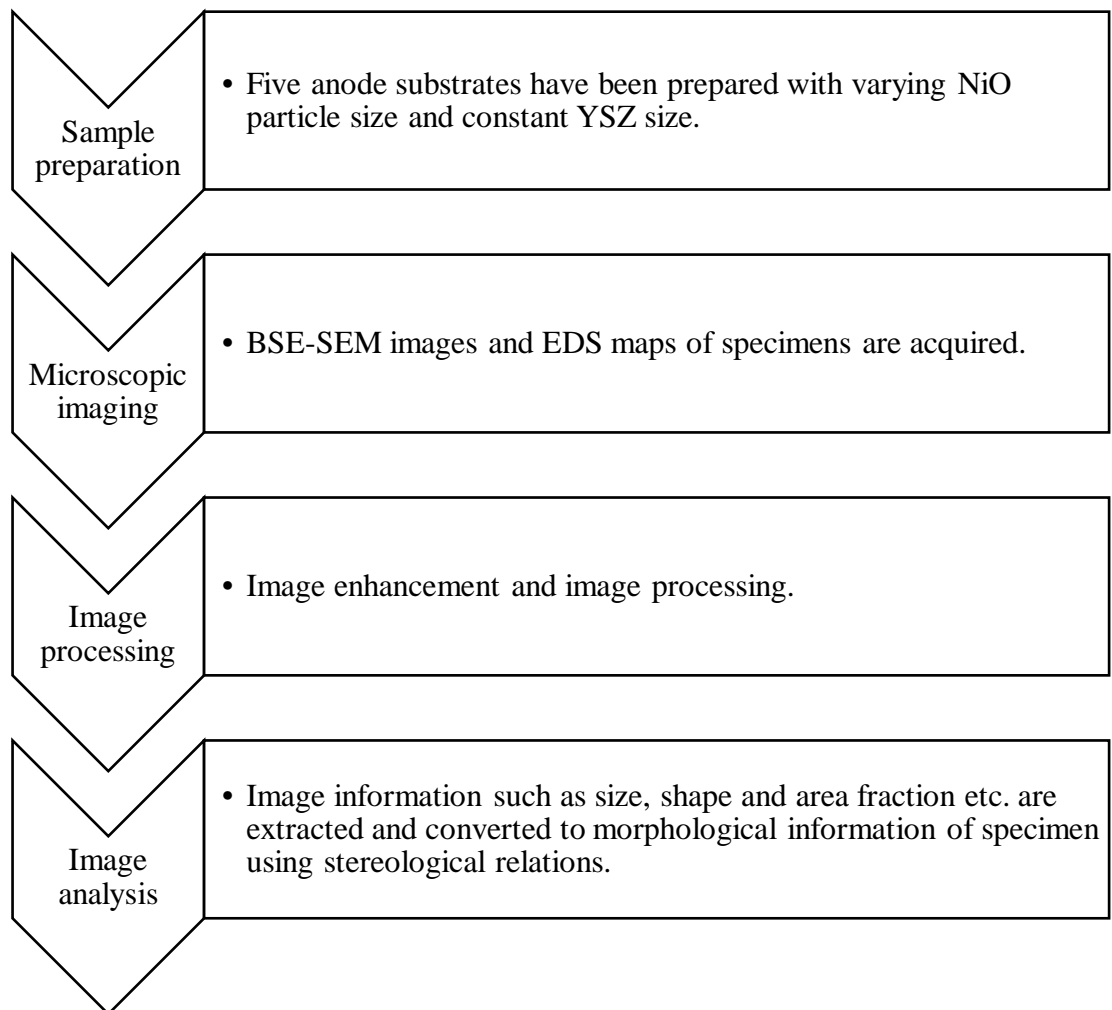


Figure 3.1 Workflow diagram

3.2 Experimental methods

3.2.1 Anode substrate fabrication

Anode materials for SOFCs need to fulfil some requirements such as high electrochemical activity towards fuels electro-oxidation, chemical stability, thermal stability, mechanical stability, low electrical resistivity, low resistance for the transport of reactants and products, fuel flexibility, resistance towards poisoning of material due to fuel impurities (for example-Sulphur), low cost and ease of fabrication (151) (152). Ni-YSZ cermet is the state of art anode material that is widely used due to its low cost, thermal stability, chemical stability and good electronic conductivity (152). It suffers from some issues such as carbon deposition in case of hydrocarbon fuels (2), nickel particle coarsening (85) and low redox stability(153).

Ni-YSZ anode substrates have been fabricated using the commercially available NiO and YSZ powders from fuel cell materials and NexTech Materials, with surface areas of 0.47 m²/gm and 9.6 m²/gm, respectively. There are several methods for NiO-YSZ anode powder preparation such as mechanical processing, combustion synthesis, precipitation, Pechini process, precipitation, and electroless technique. Selection of anode powder preparation method depends upon the cost and ease of technique, required powder morphology and phase distribution (151). In our study, we prepared anode powder by manually mixing the NiO-YSZ in the weight fractions of 60:40 with 7% by weight PVB (Poly Vinyl Butyral) in ethanol due to the simplicity and commercial use of this technique. Anode performance is affected by the volume fraction of nickel due to its role in electrical conductivity and structural stability. Nickel threshold volume fraction is about 30% for conductivity as predicted by percolation theory (30). Nickel volume fraction in the range 40-45% is recommended for optimum anode performance(151).

Five anode powders have been prepared with different particle sizes for the NiO. As per Bond crushing law, energy required to crush the particles is inversely proportional to the square root of particle size, so more energy is required as the particle size decreases. We have ball milled the NiO powder for increasing time durations (0, 1, 3, 6 and 24 hours) to increase the particle size difference using the planetary mill (Fritsch, Pulverisette 6) at 400 rpm (rounds per minute). Anode

fabrication methods are chosen depending upon the type of cell, namely, anode supported, cathode supported or electrolyte supported and the cell geometry; whether it is a planar cell or a tubular cell. There are various methods such as die pressing, gel casting, extrusion, cell printing, wet powder spraying, dip coating, plasma coating etc. (151). Die pressing has been used here to fabricate the anode substrates. Although die pressing technique is a time consuming process, it is widely used for laboratory button cells fabrications and thicker substrates preparation due to its simplicity and cost-effectiveness (154). 0.35 gm of dried anode powder is pressed to form a pellet and the pellets were sintered at 1400 °C (87) (155) for 5 hours.

The sintering temperature effect on anode microstructure and performance has been studied by several researchers (87, 155) (156). It has been observed that the percolation threshold volume fraction decreases with increase in sintering temperature possibly due to narrower pore size distribution, decreased porosity and increased contiguity between nickel particles. Sintered anode pellets were treated in the presence of hydrogen at 750°C for the reduction of NiO to Ni. There is no noticeable change in the anode substrate dimensions (Figure 3.2) due to decrease in volume as NiO reduces to nickel, and most of volume reduction appears as porosity in anode substrate.

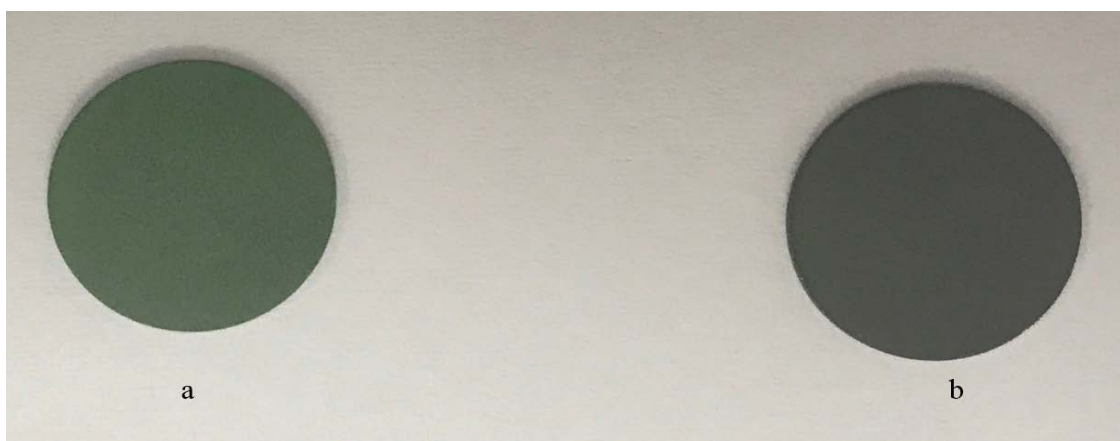


Figure 3.2. Anode substrate before reduction (a), after reduction (b)

NiO is classified as hazardous material according to Safe Work Australia. Because of its carcinogenic effects on humans (IARC (International Agency for Research on Cancer) Group 1), it requires safe work practices and proper handling of material with dust-proof glasses, PVC or rubber gloves, coverall, particulate respirator, recycling of waste and should be prevented from contamination of aquatic life. YSZ

is also classified as hazardous and should be handled with dust-proof glasses, PVC or rubber gloves, coverall, particulate respirator and recycling of waste.

3.2.2 Imaging specimen preparation

For microstructural investigations, samples were sectioned from the cross-section of the anode substrate. Five different anode substrate samples were put into the mould and impregnated with Epofix epoxy resin under vacuum using Struers CitoVac to preserve the anode microstructure during the polishing step.

Samples are further polished down to 0.04 micron in the presence of lubricants using Struers Tegramin-30 as shown in Table 3.1. Specimens are further polished using Buehler Vibromet II for four hours using colloidal silica. Following this, the samples are evaporative coated with carbon using Cressington 208C carbon evaporative coater to make the sample conducting and to avoid any charging effects during imaging.

Table 3.1 Steps for polishing procedure

Polishing	1	2	3	4	5	6	7
Steps							
Cloth	MD- Piano 220	MD- Piano 220	MD- Largo	MD- Pan	MD- Dur	MD- Dur	MD- Chem
Lubricant	Water	Water	Brown	Brown	Brown	Brown	Colloidal Silica
Time (seconds)	30	120	180	210	180	150	120
Coarseness (μm)	-	-	9	9	3	1	0.54

3.2.3 Imaging of anode specimen

Scanning electron microscopy generates images of the sample by scanning the sample surface with high energy electrons. The signals generated by the electron-sample surface interaction provides information about the sample topography, sample morphology, composition and crystalline structure depending upon the incident electron's energies. There are variety of signals generated by sample-

electron interactions, secondary electrons, back-scattered electrons, diffracted back-scattered electrons and characteristics x-rays(Figure 3.3).

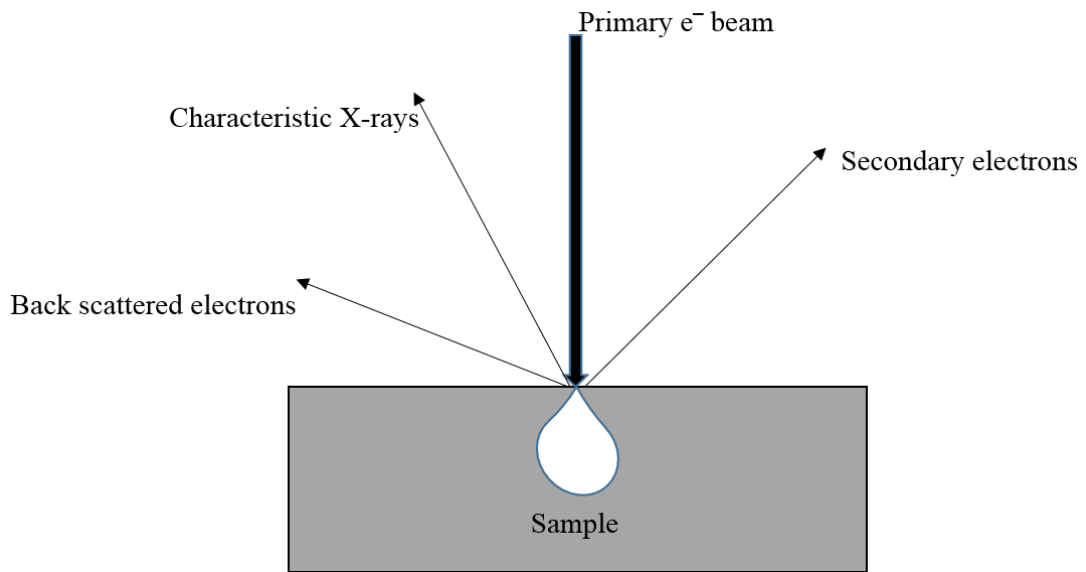


Figure 3.3. Different types of electrons generation during interaction of incident electron beam with matter

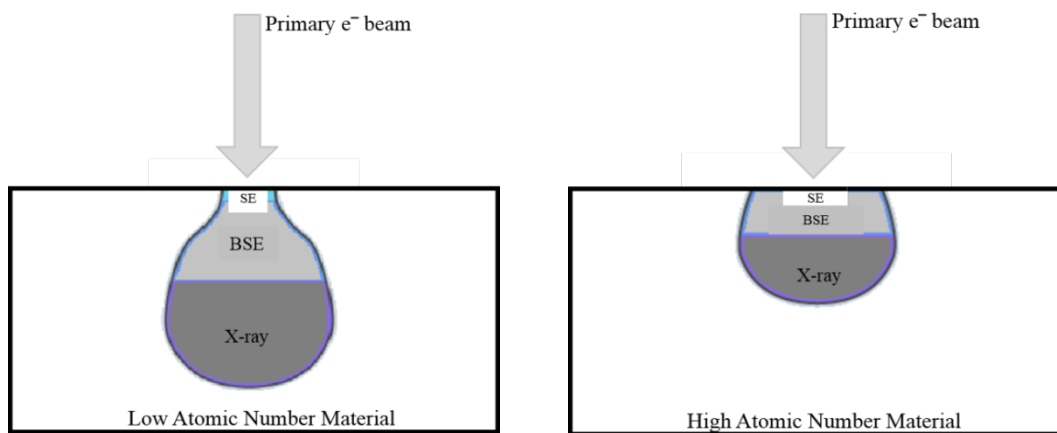


Figure 3.4. Interaction volume of electron beam with different atomic number materials

Secondary electrons are low energy electrons and provide the morphology and topography information of the sample. Backscattered electrons are high energy electrons that provide contrast between different atomic elements. SE images provide good edge details and the yield of secondary electrons from the specimen can be increased by coating the specimen with heavy metal such as gold or platinum. BS electrons are produced from a deeper interaction volume so the spatial resolution in

BSE is not as good compared with the SE image resolution (Figure 3.4). Due to the deeper interaction volume, the BS electron doesn't provide any surface information and gives composition heterogeneity information through atomic number contrast.

SEM combined with EDS analysis can give qualitative and quantitative information on the chemical composition of the sample. Two types of x-rays are generated by interaction of the incident electron with material; continuum or background x-rays and characteristic x-rays. Background x-rays are generated by the slowing down of primary electrons due to electric field of sample nuclei (Figure 3.5). Electrons from primary beam loose energy and change direction due to the inelastic scattering in the sample. Some of the lost energy is converted to x-rays with energies varying from zero to primary beam electron energy. So the background x-rays cannot have energy more than the primary electron beam energy and that is known as Duane-Hunt limit. Characteristic x-rays generation is a two-stage process: ionisation followed by relaxation. Firstly, an electron is removed from one of the inner shells of the atom by a primary beam electron so that the atom is ionised and unstable. Secondly, the atom regains stability when an electron from an outer shell fills the inner shell vacancy and an x-ray photon is emitted (Figure 3.6). The energy of the emitted x-ray is equal to the difference between the ionisation energies of the electrons involved in the transition. The spectrum from the EDS shows the characteristic x-ray lines superimposed on the background x-rays. Since the x-rays are generated from the whole interaction volume in the specimen, the spatial resolution is in the order of several microns. This interaction volume increases with increase in the incident electron energy and decreases with the element's atomic number.

Anode substrate specimens were imaged using SEM (Tescan mira3 XMU). We have performed low voltage SEM as suggested by Thyden et al. (39) and Faes et al. (40). Our parameters for imaging were 3kV accelerating voltage, 30 μm aperture size and working distance of 6 mm. As our specimen images Figure 3.7 (a) and its histogram Figure 3.7 (b) shows, it is difficult to identify any phases and obtain segmentation of Ni and YSZ in the image acquired using LV-SEM. (Figure 3.7). HV-BSE imaging has also been tried as suggested by Monachon et al. (38). The imaging parameters we used were 20kV accelerating voltage with 15 mm working distance. Although it gives a better contrast between Ni, YSZ and pore compared to low voltage SEM images, still it is very difficult to clearly identify the individual particles in the

sample image Figure 3.7 (e). We have also investigated the in-lense BSE-SEM imaging at 5 kV accelerant voltage, working distance of 4.3 mm for our sample, it seems quite promising and gives clear distinction for pores in the image but still there is not enough contrast in the Ni and YSZ to separate the phases as we can see in the histogram Figure 3.7 (c & d). There is a large variation in grey scale of one particular phase and no clear separation for Ni and YSZ as observed in the histogram. The above techniques may require more smooth polishing of the specimen to minimize the grey variation within the individual phases and to improve contrast between different phases.

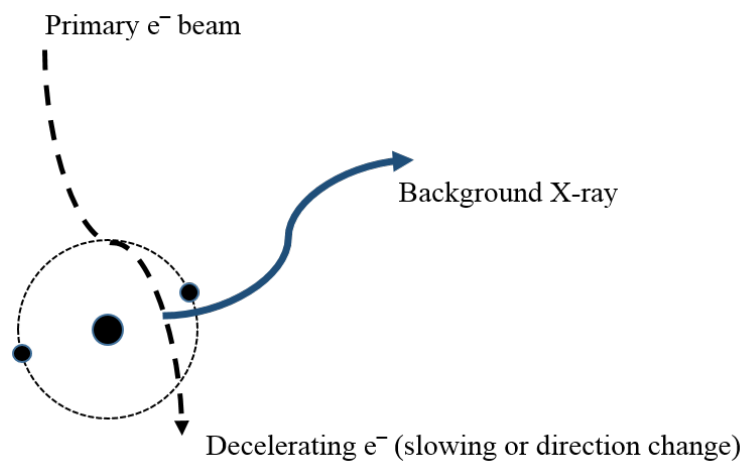


Figure 3.5. Background X-ray generation during atom-electron beam interaction

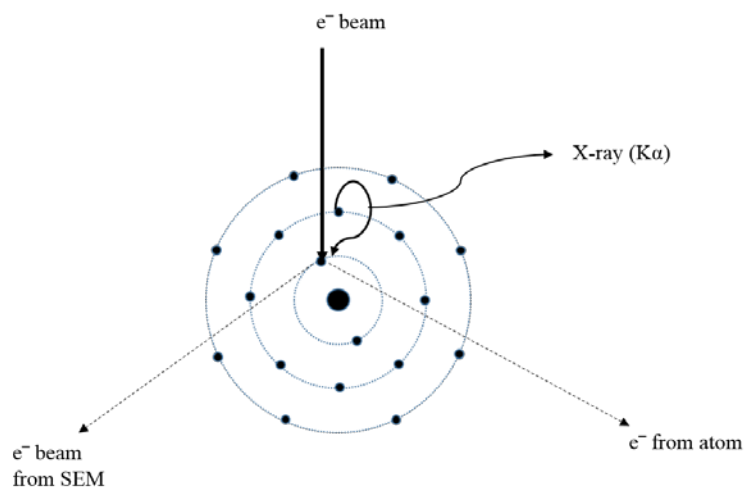


Figure 3.6. Characteristic X-ray generation from an atom during interaction with electron beam

To overcome this issue of phase identification and separation of the phases in the image, we have used information from EDS maps that help in clearly identifying phases in the anode substrate as shown in Figure 3.8(a). Laznini et al. (41) also have suggested EDS maps to analyse phases in anode substrate. EDS maps give the elemental map information but due to larger interaction volume of electron beam (refer to Section 3.2.3) with material, there is very poor resolution in-between particles and difficult to identify the pores. BSE imaging gives the best resolution for pores among SE and BSE imaging. Therefore, combining the BSE image with EDS maps gives us an image with the identification of pores, nickel and YSZ. It can be observed from the histogram (Figure 3.8 e) of such EDS-BSE grey image (Figure 3.8 d) that gives the clear distinction between all three phases. To the best of our knowledge, EDS-BSE image has not been used for the extraction of microstructural properties in SOFC electrodes.

3.3 Quantitative analysis

3.3.1 Image segmentation

Image processing operations are performed on raw images to get enhanced images that can be used for further image analysis to get quantitative information from images. These image processing operations are performed using Fiji (157) and Matlab Image Processing toolbox. BSE images superimposed with EDS maps are converted into greyscale images and, contrast and brightness were enhanced for further image processing operations. In this greyscale image, it becomes very easy to identify the phases where Ni is light grey, YSZ is dark grey and pore is black in Figure 3.8(d).

Further, noise is removed from the images using noise filters available in Fiji. Salt and pepper noise is a prevalent artefact in EDS maps and appears as isolated pixels and rough edges on the features in the image. It should be kept in mind that noise removal and detail preservation are conflicting requirements. Salt and pepper noise in the image is removed using Despeckle filter in Fiji, which is a median filter. In a median filter, the output value of a particular pixel is given as the median value of that pixel along with all the pixels in its immediate neighbourhood.

Image segmentation is the process of segmenting image into meaningful parts based on the similarity of features or properties. Traditionally used image segmentation

methods are based on discontinuity detection or similarity detection of pixels in a region. Threshold method, Edge based method, Clustering based method, region based method, Watershed based method, and Partial Differential Equation (PDE) based method are the most popular image segmentation techniques (158). Apart from traditional methods, there are some trainable segmentation methods, which use much more information than intensity or colour information of a pixel. In these machine learning techniques, artificial neural network is used to segment the image by simulating its learning process. A set of pixels are labelled and identified as a feature space that can be used as a classifier, once the classifier is trained that can be used for segmentation of rest of pixels in image data. There are many commercial and open source platforms for this purpose. We are adopting the open source software TWS due to its user friendliness and GUI, that makes it easy to use without intensive programming. It combines the image processing toolkit Fiji and machine learning algorithm provided in data mining and machine learning toolkit Waikato Environment for Knowledge Analysis (WEKA). TWS provides feature based classification based on edge detection (Sobel filter, difference of Gaussians, Gabor filters etc.), texture information (Minimum, Maximum, Median, Variance, Entropy etc.) or customizable features that can be user defined with simple script(159). GUI in TWS provides the feasibility of interactively train the classifiers in image data and use them for further image segmentation. There are set of training features provided in TWS, we have used Gaussian blur, Sober filter, Membrane projections, Difference of Gaussians, Variance, Mean, Maximum and Median features to train the classifier and, the default classifier FastRandomForest. This kind of segmentation is better compared to a simple thresholding method where it is difficult to define the particle boundaries (160, 161). Simple thresholding is the most widely used image segmentation method in SOFC electrode research area. But, due to the challenges involved in image segmentation using traditional thresholding (37, 41, 53, 56, 58, 162, 163),(164) PDE based (101) image segmentation technique has also been explored.

Image segmentation using Otsu's threshold method and one from trainable segmentation method are shown and compared in Figure. (3.9), As evident from this figure that the quality of trainable segmentation (Figure 3.9 c) is better than the segmented image from Otsu's threshold segmentation (Figure 3.9 b) method.

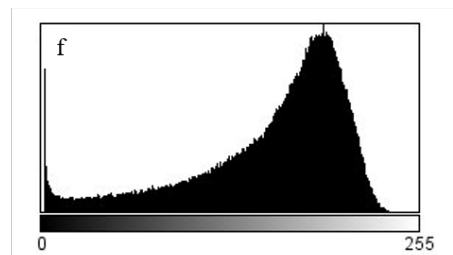
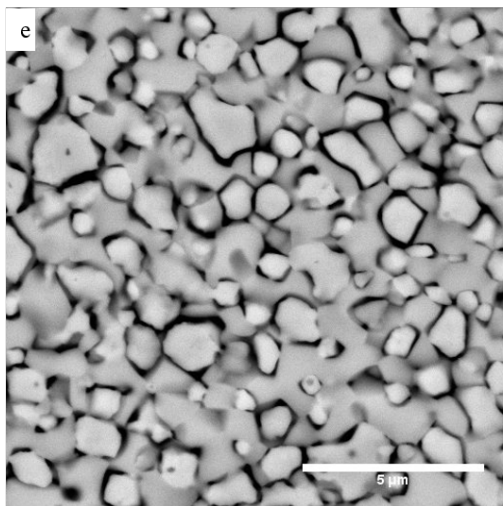
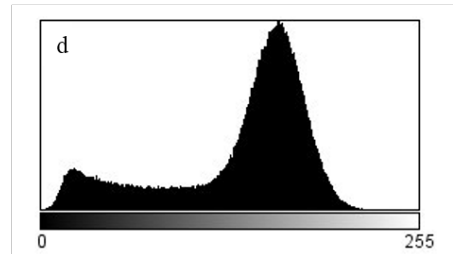
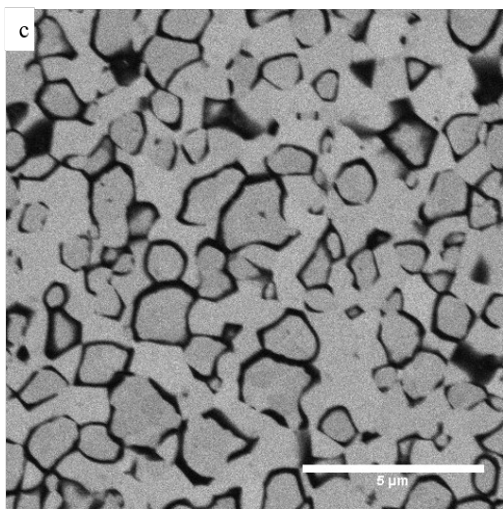
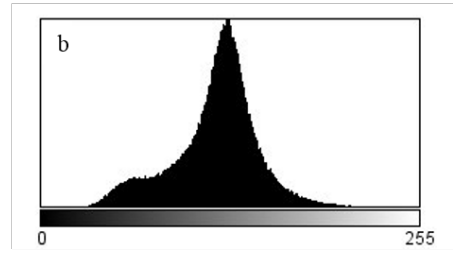
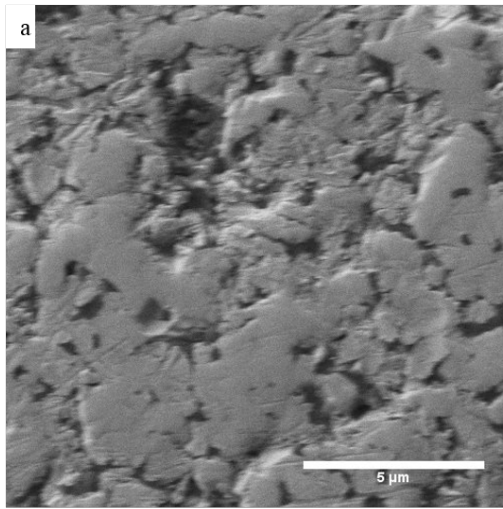


Figure 3.7. Low voltage secondary electron image (a), histogram of secondary electron image (b), low voltage in-lense BSE image (c), histogram of in-lense BSE image (d), high voltage BSE image of sample (e), histogram of high voltage BSE image (f)

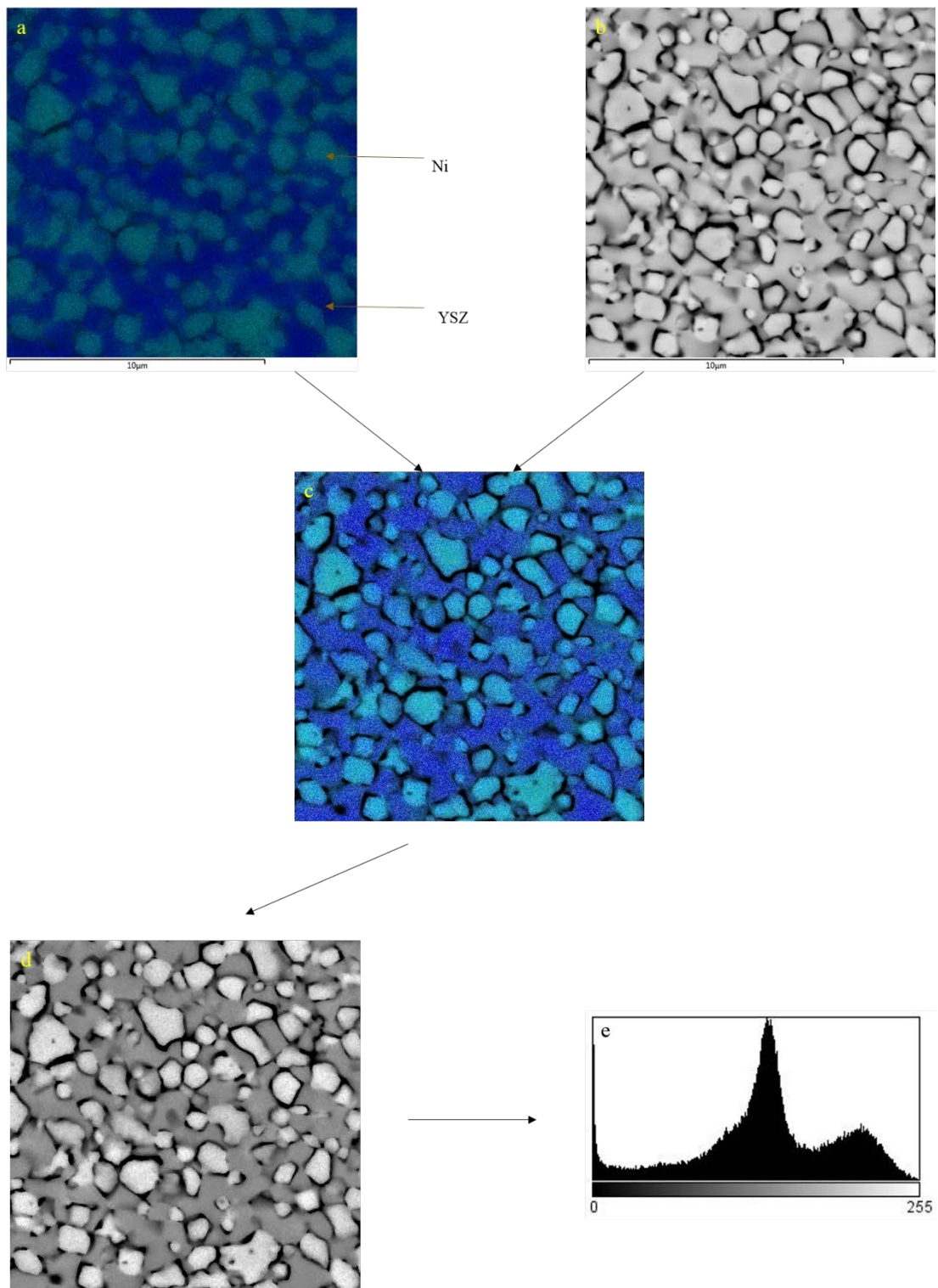


Figure 3.8. EDS map of Ni-YSZ anode substrate (a), high voltage BSE image (b), overlaid BSE image on EDS map (c), grayscale image of superimposed image (d) histogram of superimposed grayscale image (e)

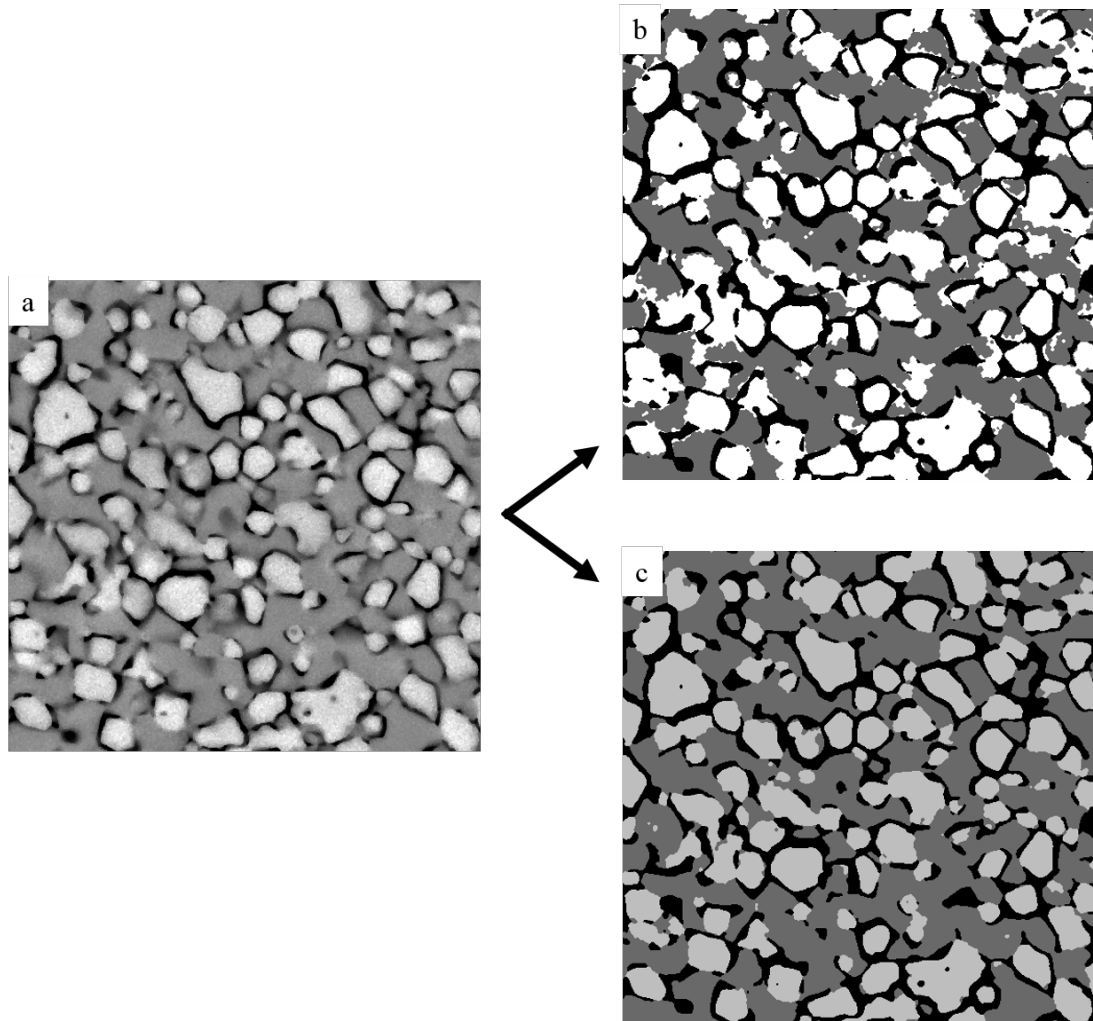


Figure 3.9 Greyscale image (a), segmented image obtained using Otsu's thresholding method (b), segmented image obtained using TWS (c)

3.3.2 Image analysis and stereology

Image analysis is the extraction of meaningful information from the images to characterise their content. This information is object specific such as shape, area, colour and intensity etc. This image analysis information can be further transformed into morphological quantities of the specimen using stereological relations.

Stereology is a sub-discipline of stochastic geometry that is used to obtain 3D microstructure information from 2D planar sections (165). While deriving such information from the 2-D images of objects, it is assumed that the investigated material is isotropic, uniform and random (158). 2-D image is considered as a representative microstructure. While calculating surface area in the microstructure, surfaces should be isotropic, that is, they should have equal probability of being

oriented in any direction. Every part in the microstructure should have equal probability of being examined through the image (uniform assumption). There should be no bias while imaging to include or exclude some areas in the image (random assumption). In general, microstructures can be non-uniform (e.g. gradient materials) and anisotropic. In order to obtain a reliable and correct quantitative description of arbitrary microstructures in 3D, the sampling procedure must be such that the probes intersect the microstructure isotropically, uniformly and randomly. That means, probing should take all orientations and positions into equal account and sampling should not be influenced by microstructural systematicity (e.g. periodicity).

3.3.2.1 Volume fraction

Volume fraction of a phase can be determined using the most fundamental stereological relationship, *Delesse-Rosiwal law* given as,

$$V_V = A_A = L_L = P_P$$

Where, V_V is the volume fraction of a phase of interest in 3D volume, P_P is the fraction of points hitting the phase of interest divided by the total number of points placed on the image, L_L is fraction of length of lines hitting the phase of interest divided by the total length of lines placed on the image and, A_A is area fraction of a phase of interest divided by the total area of the specimen image. So, the volume fraction of a phase can be calculated by measuring the area fraction of that phase on the image or, equivalently, by using a superimposed line grid or point grid to measure the cumulative line length or the number of points hitting the phase in image, respectively.

3.3.2.2 Surface area

Surface area of individual phases, S_V in the sample volume can be determined from the specimen image using the stereological relation (equation 3.1),

$$S_V = 2P_L = \frac{4}{\pi}L_A \quad (3.1)$$

Where L_A is the total length of perimeter of phase of interest per unit area of sample image (m^{-1}) and can be calculated using the Matlab image processing toolbox, P_L number of intersection points with feature lines or curves (e.g. phase perimeters) per unit length of a probe line (e.g. a line in a superimposed grid) (m^{-1}). Interface surface

area between two phases can be calculated from individual surface area values. The relation between interface area and individual phase surface can be expressed as:

Nickel surface area = Ni-pore interface area + Ni-YSZ interface area

YSZ surface area = Ni-YSZ interface area + Pore-YSZ interface area

Pore surface area = Ni-pore interface area + YSZ-pore interface area

3.3.2.3 Triple phase boundary

TPB length is defined as the region where all the three phases are present to support the electrochemical reaction. TPB length per unit volume can be estimated using the stereological relation (equation 3.2).

$$L_{TPB} = 2P_A \quad (3.2)$$

Where, L_{TPB} is TPB length per unit volume and, P_A are the points of interest per unit area of image, P is the point where all three phases meet in the 2-D image of specimen as shown in Figure 3.10 Triple phase points in the image are found by scanning the sample image with 2×2 matrix of all possible combinations where all three phases are present.

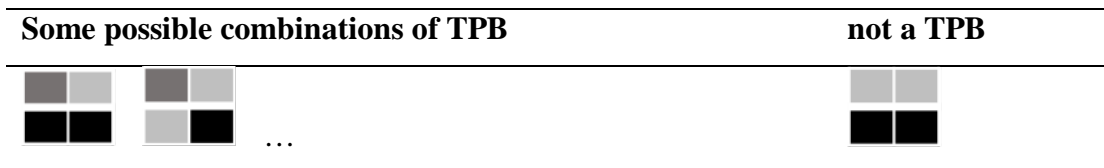


Figure 3.10. Some possible combinations of TPB pixels (a), not a TPB point (b)

3.3.2.4 Particle size

There are various methods and approaches to calculate particle size from the 2-D images. Few commonly used methods are described below.

Line intercept method: The number of particles from the phase i intercepted by the line (N) is measured along horizontal and vertical lines (spaced of 10 pixels). Knowing the total length of the line (L) and the volume fraction (V), the particle size for a particular phase can be obtained using (equation 3.3),

$$L_{IM} = \frac{LV_i}{N_i} \quad (3.3)$$

Particle size from the image analysis data is multiplied by a factor of 1.5 to get real mean particle size [38] for spherical particles. YSZ and pore are considered irregularly shaped. In this case, the real particle size is obtained using the ASTM

standards, where equiaxed but irregularly shaped grains should be multiplied by a factor of 1.13.

Morphological method: It involves the Feret diameter calculation, which is the distance between two parallel lines drawn on opposite ends of an object. It can be measured in any direction, usually the maximum distance between two parallel lines drawn on opposite end for a particle is given as the Feret diameter. In similar fashion, minimum Feret diameter will be the minimum distance between two parallel drawn on a particle.

Equivalent diameter: Equivalent circle diameter is often used to measure particle size due to its simplicity and it avoids any particle shape effects. It is calculated by measuring the area of each particle and the equivalent diameter of each particle is measured as the diameter of an equivalent area circle, $D = 2\sqrt{(Area/\pi)}$ Average size for the particles of a particular phase can be determined statistically from the individual equivalent diameter measurements.

Thickness: Individual phase size is calculated by the local thickness approach using BoneJ plugin available for Fiji (166). Particle size is measured as structure thickness which is also known as local thickness (167) measured at any given point in the structure as diameter of the largest circle that contains that point and fills completely inside the structure as shown in Figure 3.11. The blue to yellow collar variation is for largest diameter circle size that can be fit into the pore structure.

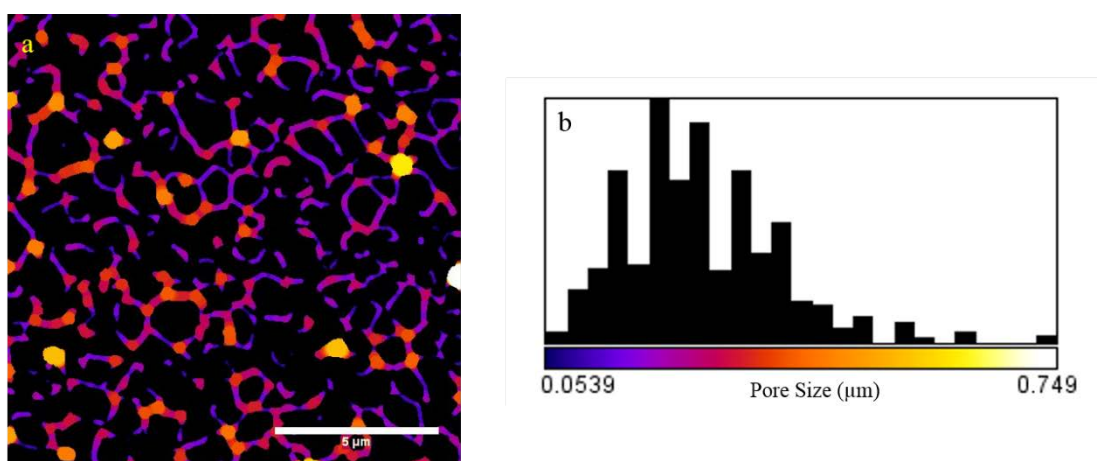


Figure 3.11. Thickness diagram for pore phase in a sample (a) and, size distribution of pore size (b) in sample

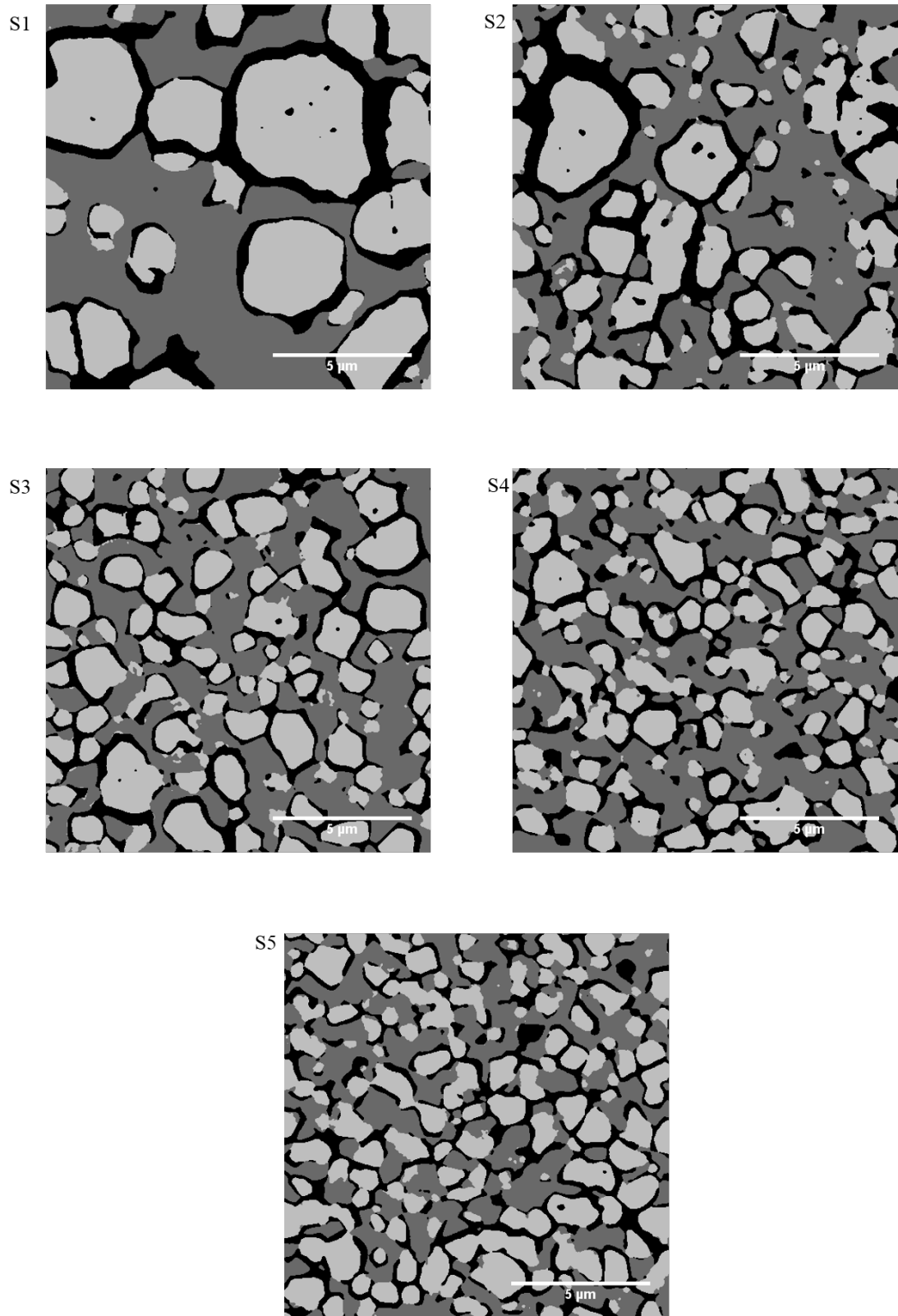


Figure 3.12 Five microstructures S1 to S5 resulted from different Ni particle size

3.4 Results and Discussion

Volume fraction: All samples are composed of the same volume fraction of NiO-YSZ with different particle sizes for NiO powder. We considered the anode samples to have no packing porosity before reducing the anode substrate from NiO-YSZ to Ni-YSZ (40). Porosity in anode substrate Ni-YSZ is generated from the reduction of NiO-YSZ in presence of hydrogen as explained in section 3.2.1. As the particle size for NiO has changed, it resulted in different microstructures as shown in Figure 3.12.

Volume fractions of each phase in the sample images are calculated using image analysis and stereological relations as explained in section 3.3.2.1. The initial volume fraction of phases are calculated using the available weight fraction value and density of Ni, NiO and YSZ. Image acquisition, image processing and image analysis processes induce error in the extraction of microstructural properties from the specimens. It is very difficult and subjective to identify the contribution of error from each step during information extraction from images (168). Fluctuations in properties with S1 to S5 can be due to the reason of this process uncertainty. It can be observed in volume fraction values that error is +20% to -3% of theoretical volume fractions. Uncertainty in image analysis results has been found in the range of 15% in the literature (40). Anode composition can be calculated using known weight fractions and densities of NiO, Ni and YSZ.

Table 3.2 Volume and weight fraction of individual phases in Ni-YSZ anode substrate

Anode composition (Before Reduction)		Anode composition on solid basis (After Reduction)				Anode composition including porosity (After Reduction)				
Weight percentage	Volume percentage	Weight percentage	Volume percentage	Weight percentage	Volume percentage	Volume percentage				
NiO	YSZ	NiO	YSZ	Ni	YSZ	Ni	YSZ	Ni	YSZ	Pore
60	40	57.02	42.98	54.10	45.9	43.84	56.16	42.98	33.53	23.49

Particle size: We have used three methods for nickel particle size measurement. It is not feasible to determine particle size using equivalent diameter or Feret diameter for YSZ and pores due to their morphology (since pores and YSZ phase are continuous

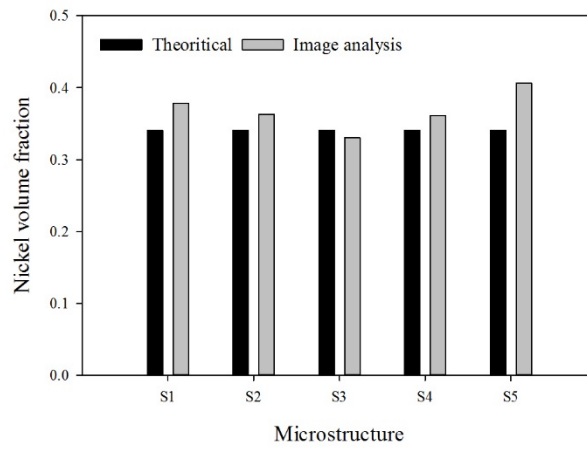
and doesn't have discrete particle shapes). Local thickness approach has been used to characterise size for YSZ and pores (135). Nickel particles size is measured as Feret diameter, equivalent diameter and local thickness. Nickel particle measurement from all the three methods (Figure 3.14) show similar trends of decreasing size. Although the trend is the same, the values of Feret diameter for the nickel particle are fluctuating due to the limitation of the measurement technique (since it measures the maximum Feret diameter of a particle.). It is observed that the magnitude of change for the particle size is comparatively small after first grinding of the NiO powder. Increase in grinding time resulted in no significant changes in particle sizes. This could be due to the de-agglomeration and re-agglomeration of nickel particles at the smaller size and the energy released during the ball milling (169). This limit of particle size decrease is dependent upon the impact energy of the grinding media balls; which varies with grinding media size and milling conditions (170).

It is also observed that varying the size of NiO powder during the synthesis of anode substrate resulted in the decrease of YSZ size and pore size in the anode substrates as shown in Figure 3.15(a & b). It has been observed that the size ratio of YSZ size and nickel particle is around one after sintering. There could be two possible reasons for that: First is NiO particles are inhibiting the grain growth for YSZ particle similar as observed for NiO-BSCF electrode by Chen et al. [26]. Second is, during the mixing of NiO and YSZ powders before sintering if smaller the size of NiO particles they will get distributed in the packing of particles and will result into smaller grain size for YSZ. This can also be observed from the research work reported by Faes et al. (40), where the size of YSZ and pore also changed while nickel particle coarsened and size increased during cell operation. Although they ignored this change in YSZ size and assumed it to be within the range of measurement technique error. To the best of our knowledge, this phenomenon is observed the first time for NiO-YSZ anode substrate, where decrease in NiO size also resulted in decrease in YSZ size after sintering with the size ratio remaining around one after sintering as shown in Figure 3.16.

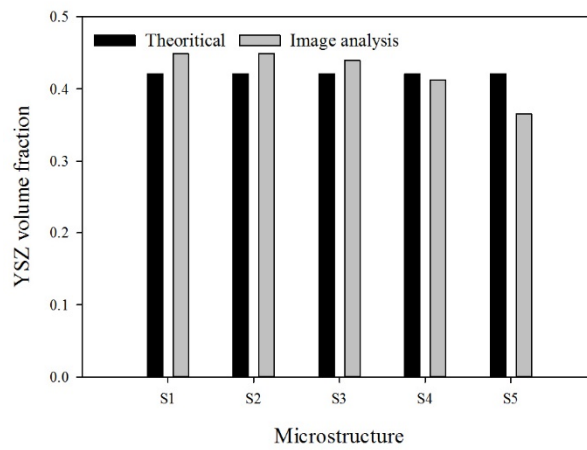
Finer the nickel or YSZ particle, easier will be percolation of the particles (171), which will enhance the electrical and mechanical performance of the anode substrate (172). Pore size will have an effect on the mass transport in anode substrate influencing the reaction rates and electrochemical performance (135) (173).

The decrease in nickel particle size in the microstructure will also result in decrease in pore size as observed from Figure 3.15(b). Smaller pore size will inhibit the transport of gas molecules from bulk to the active sites resulting in increase of concentration polarisation in anode (77). Flow of gaseous molecules in the anode can be described by ordinary flow, Knudsen flow and viscous flow depending upon the Knudsen number. Generally for the SOFC anode Knudsen number lies in the range of 0.1 to 5 (135) and that is transitional diffusion regime. Flow is controlled by ordinary diffusion and Knudsen diffusion in the transition regime. Knudsen number is dependent upon the pore size and mean free path of gaseous molecule. Lower the pore size greater will be Knudsen number and, Knudsen diffusion will be the controlling mechanism (21, 135). Knudsen diffusion coefficient is proportional to pore size and will decrease as the pore size in the anode decrease. Therefore, it can be observed that the small nickel particle size gives higher concentration polarisation in anode.

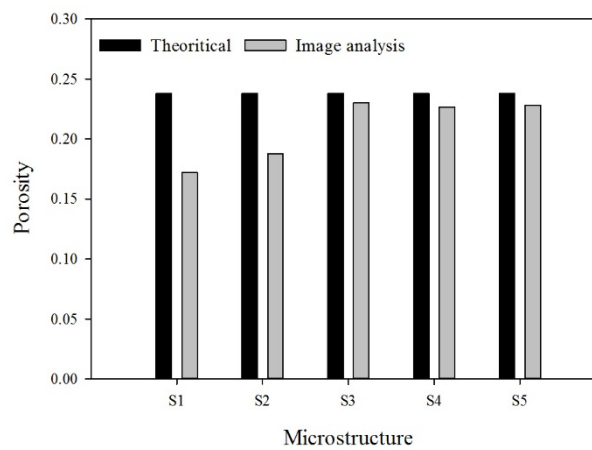
Interface area: Ni-YSZ, Ni-pore and YSZ-pore interface area was found to increase with change in microstructure from sample S1 to S5 (Figure 3.17) due to decrease in nickel particle size. While the nickel particle size decreases from S2 to S3 there is increase in size of YSZ phase. Whereas, from microstructure S1 to S5, the overall trend of particle size is decreasing for both nickel and YSZ. The change in trend of YSZ size from S2 to S3 compared to the overall trend from S1 to S5 is due to the reason of uncertainty in the overall process of feature extraction from images. This error involved in properties extraction from images will probably also lead to the decrease in nickel-pore surface area from S2 to S3 while the overall trend from S1 to S5 is increasing for the nickel-pore surface area. Increase in Ni-pore interface area will provide more surface area for steam reforming reaction in the case of hydrocarbon fuel (174) and will also benefit the electrochemical reaction (54). Increase in YSZ-pore area will provide more availability of oxide ions and will be beneficial for electro-oxidation of carbon deposited in anode (109). Interface surface area values for Ni-YSZ, Ni-pore and YSZ-pore are in the range of 0.1-1.9 $\mu\text{m}^2/\mu\text{m}^3$, 0.7-1.7 $\mu\text{m}^2/\mu\text{m}^3$ and 0.5-1.6 $\mu\text{m}^2/\mu\text{m}^3$ respectively, for different nickel particle sizes, which are of the same order of the values reported by Vivet et al. (54) for different volume fraction of nickel in the anode.



(a)

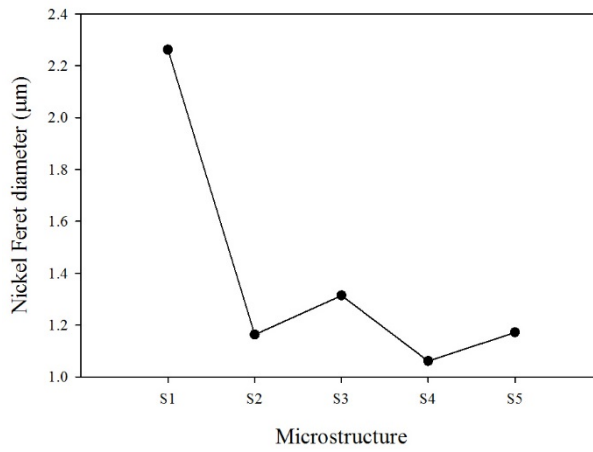


(b)

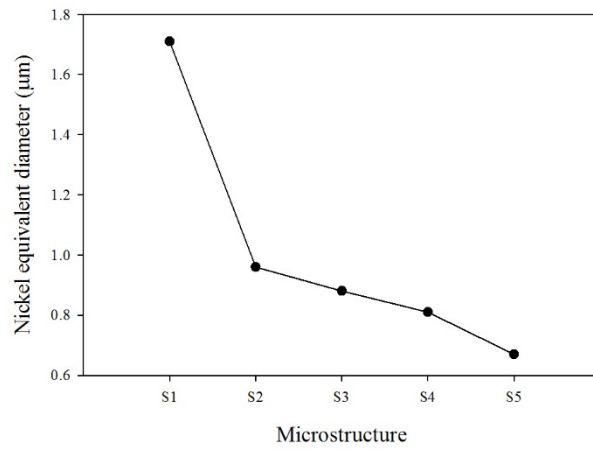


(c)

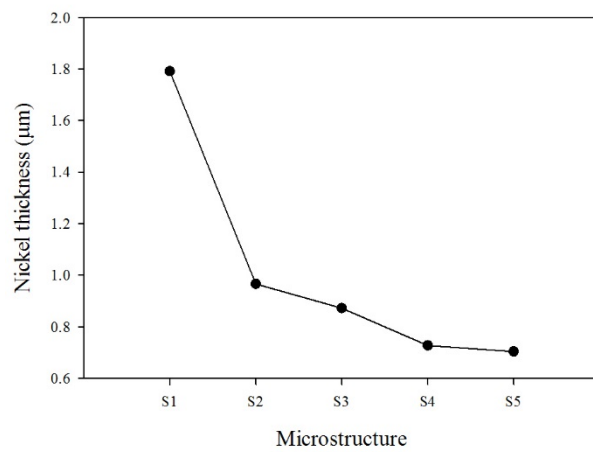
Figure 3.13 Volume fraction for Ni in microstructure S1 to S5 (a), Volume fraction for YSZ in microstructure S1 to S5 (b) and, Volume fraction for Pore in microstructures S1 to S5 (c)



(a)



(b)



(c)

Figure 3.14 Nickel Feret diameter (a), Nickel equivalent diameter (b) and, Nickel local thickness (c) for microstructures S1 to S5

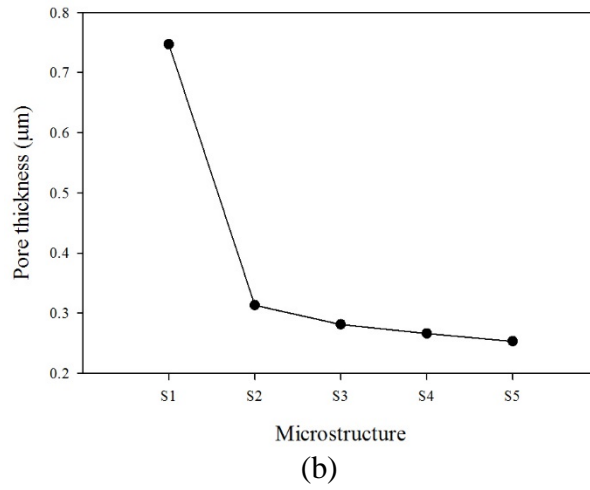
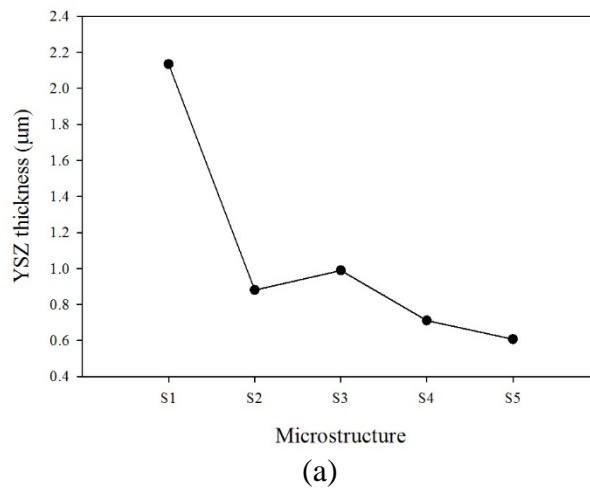


Figure 3.15 YSZ local thickness (a) and, Pore local thickness (b) for microstructures S1 to S5

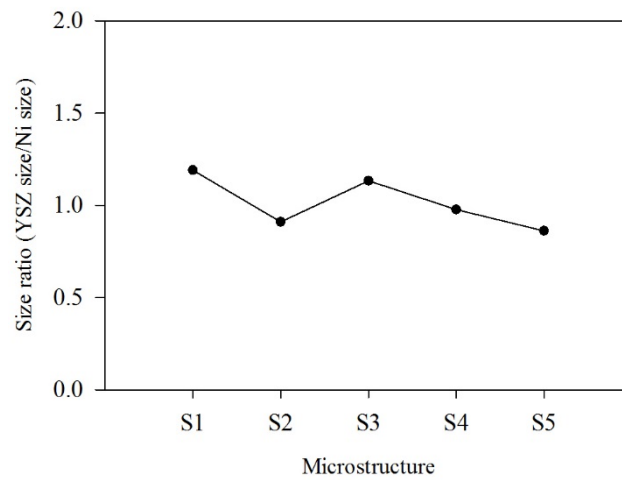
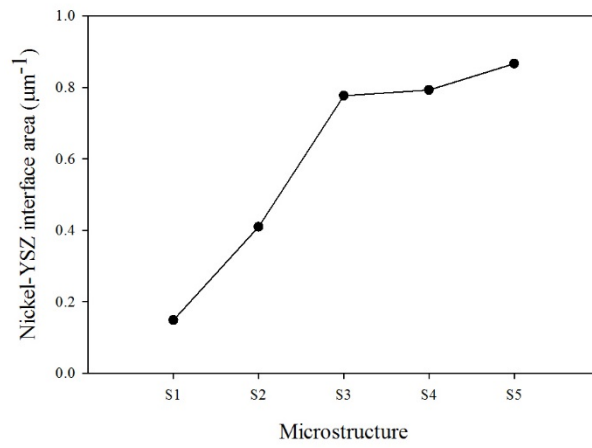
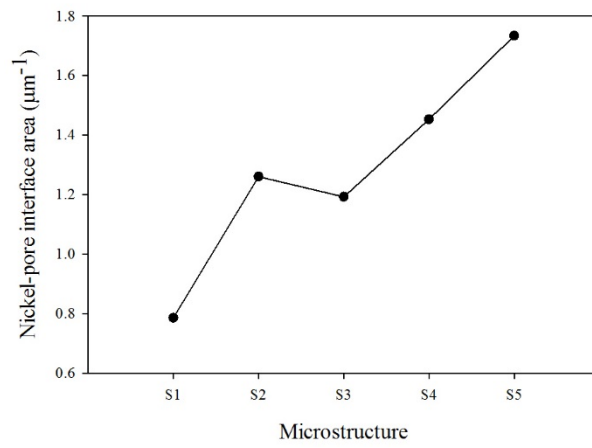


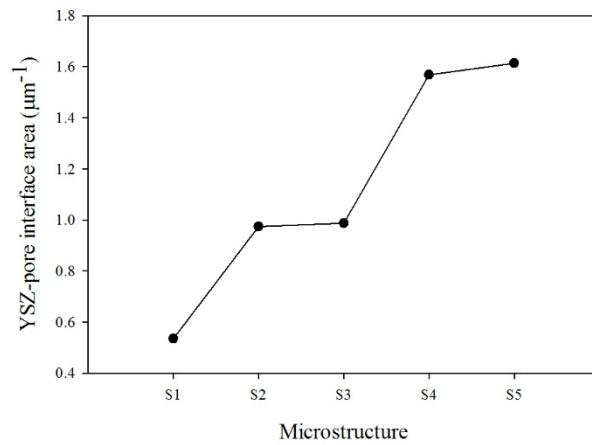
Figure 3.16 size ratio of YSZ to nickel particle for microstructures S1 to S5



(a)



(b)



(c)

Figure 3.17 Ni-YSZ interface area (a), Ni-Pore interface area (b) and, YSZ-Pore interface area (c) for microstructures S1 to S5

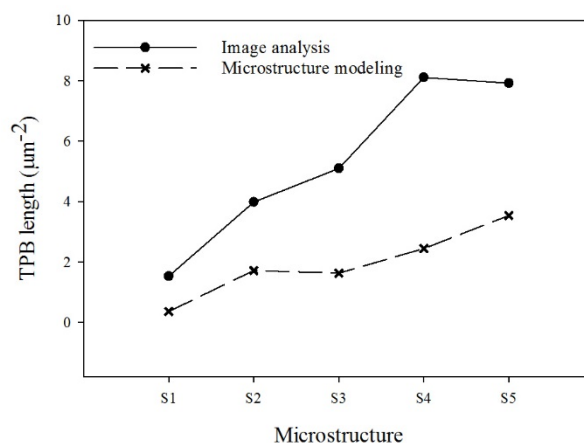


Figure 3.18 Triple phase boundary length for microstructures S1 to S5

Triple Phase Boundary: TPB length plays an important role in the electrochemical performance of SOFCs (81). TPB length has been observed to be affected significantly with the change in the microstructure (54) (48, 55, 175). The triple phase boundary calculated here using image analysis and stereology showed that it increases to fivefold as the anode microstructure changes with decreasing nickel particle size. TPB density increased from $1.52 \mu\text{m}/\mu\text{m}^3$ to $8 \mu\text{m}/\mu\text{m}^3$ as the nickel particle size varied from $2.26 \mu\text{m}$ to $1.17 \mu\text{m}$ (Figure 3.18).

It has been also observed that while the change in particle sizes was very small for microstructures from S_2 to S_5 , TPB length changes by comparatively larger magnitude and this behaviour is similar to the results obtained from analytical modelling of anode microstructure (Figure 3.18). Also, it can be observed from our micro-modelling results that as the particle size decreases the TPB area increases very rapidly (Figure 4.4(e)). This increase in TPB from microstructure S_1 to S_5 is due to inverse proportionality of the TPB with the square of the particle size ($A_{tpb} \propto 1/\min(r_{Ni}, r_{YSZ})^2$). Our results are found to be of the same order as the results by Faes et al. (40) and Wilson et al. (80). Experimental results reported from 3-D reconstruction of Ni-YSZ anode from Wilson et Al. 2006 (42) was also of the same order reported as $4.28 \mu\text{m}/\mu\text{m}^3$. Increase in TPB is desirable property for better electrochemical performance. So, the smaller nickel particle size should be preferred for anode synthesis but at the same time this decrease in nickel particle size also decreases the pore size in anode and results in greater concentration polarisation.

3.5 Conclusions

In this chapter, BSE imaging and EDS maps of the specimen are utilised to improve the segmentation of phases in the electronic image of Ni-YSZ anode. We have combined the EDS information with BSE images of the specimen to simplify the identification of phases in the sample. We have further used machine learning based algorithm to segment the image in individual phases through the TWS plugin available in Fiji. Image analysis and stereological relations have been used to extract the structural properties from the processed images of samples.

Further, we investigated the effect of nickel particle size on the microstructure properties of Ni-YSZ anode. There is decrease in the rate of nickel particle size decrement with increase in milling time and the maximum decrease in nickel particle size is observed in the first hour of ball milling. It has been observed that decrease in particle size of NiO powder also resulted in the decrease in size of YSZ phase and pore phase; and changed the anode microstructure, while the volumetric composition of the components in the anode were kept constant. Interface area between phases increased linearly with particle sizes and the TPB density is observed to increase with a larger magnitude for a relatively smaller change in nickel particle size. This suggests that the use of smaller sized nickel oxide powder for the anode synthesis is beneficial for increasing the active area, but could result in increasing the concentration polarisation. The trade-off between the effects of the active area and the concentration polarisation should be a key consideration for microstructural optimisation of the anode.

Chapter 4

Anode microstructural modelling considering structural degradation

4.1 Introduction

There are several approaches as explained in the literature review in Chapter-2 to determine the electrode microstructural properties including the electrochemical active area, interface surface areas, pore size, tortuosity and effective conductivity of electron conducting and ion conducting phases. In this chapter, analytical approach is used to determine these electrode properties. Further, we use this analytical approach involving coordination number theory and percolation theory (Section 2.1.2) to investigate the effect of degradation phenomena such as nickel coarsening and carbon deposition on the anode microstructural properties. Loss of electrochemical performance in SOFC is mainly credited to the structural degradation in electrodes due to harsh operating conditions such as high operating temperature and varying fuel compositions. Such operating conditions lead to various degradation phenomena such as coking and redox in the anode; and deactivation and poisoning of catalytic materials in the electrodes due to fuel impurities. Coarsening of nickel particles and carbon formation are two important degradation phenomena in the anode that severely affect the electrode microstructural properties. Researchers have investigated the structural degradation phenomena in anode through numerical and experimental methods (40, 73, 105, 133, 176). There are several experimental studies to investigate the effect of carbon formation on microstructural properties (127, 134) but there is no study to quantify the carbon formation effect on microstructural properties. In this chapter, we use the earlier developed expressions by Bertei et al. (4) for co-ordination number and percolation probability to evaluate microstructural properties and compare with previously reported results from Chen et al. (5). We also extend our model to study the nickel coarsening n effect on microstructural properties. A microstructure model is developed to study the effect of carbon formation on microstructural properties, such model will help to optimally design the anode under several operating conditions. The main contributions of this chapter are listed below:

- We develop a model to evaluate the microstructural properties with the co-ordination number and percolation probability expressions suggested by Bertei et al.(4) and compare the results with the earlier developed model by Chen et al. (5)
- We further extend our model to investigate the effect of nickel coarsening phenomenon during cell operation on microstructural properties.
- We develop a microstructural model to investigate the effect of carbon deposition on the anode microstructural properties.

4.2 Model development:

4.2.1 Microstructural modelling

In our modelling approach, the electrode microstructure is approximated as a random packing of spherical particles; and percolation theory and co-ordination number theory are used to determine microstructural properties. In the representative electrode microstructure, ion and electron conducting particles can form three types of clusters as shown in Figure 2.2. A and B-type of clusters can contribute towards electrochemical active sites while percolating the ions (or electrons) to the reaction sites. However, ion (or electron) conducting particles form only form A-type of clusters above the threshold volume fraction of ion (or electron) conducting particles as explained in percolation theory in section 2.2. Therefore, the effect of B-type clusters have been neglected here while calculating the properties. Microstructural properties can be modified by controlling the structural parameters such as volume fraction and particle size during electrode synthesis. Microstructural parameters such as number fraction, volume fraction and surface area fraction of electron or ion conducting particles are inter-related and can be expressed in interchangeable forms given below (equation 4.1, 4.2 and 4.3):

$$n_j = \frac{\psi_j / r_j^3}{\psi_j / r_j^3 + \psi_i / r_i^3} \quad (4.1)$$

$$\psi_j = \frac{n_j \alpha^3}{n_j \alpha^3 + n_i} \quad (4.2)$$

$$S_j = \frac{\psi_j/r_j}{\psi_j/r_j + \psi_i/r_i} \quad (4.3)$$

Where α is size ratio of particle (r_j/r_i) and r_i, r_j are the size of i and j phase particles in binary particle packing, ψ_i and ψ_j are the volume fractions.

Researchers have developed few expressions for coordination number and percolation probability in random packing of particles as discussed in section 2.1.2. We adopt the coordination number and percolation probability relations given by Bertei et al. (4), since these expressions are valid for the poly-dispersed particle sizes in the electrode, and satisfies the contact number conservation principles, while also matching very well with simulated and experimental results.

The expressions for co-ordination number and percolation probability developed by Bertei et al. (4) (equation 4.5-4.8 and 4.10) are based on the expressions given by Suzuki and Oshima (65). Co-ordination number between two particles (i and j) in binary packing of particles is given as (equation 4.4)

$$Z_{ij} = S_j N_{ij} \quad (4.4)$$

Where (for $r_i > r_j$)

$$N_{ij} = \frac{0.5(2 - \sqrt{3})N_{ii} \left(\frac{r_i}{r_j} + 1 \right)}{1 + \frac{r_i}{r_j} - \left(\frac{r_i}{r_j} \left(\frac{r_i}{r_j} + 2 \right) \right)^{0.5}} \quad (4.5)$$

$$N_{ji} = \frac{0.5(2 - \sqrt{3})N_{jj} \left(\frac{r_i}{r_j} + 1 \right)}{\left(1 + \frac{r_i}{r_j} - \left(\frac{r_i}{r_j} \left(\frac{r_i}{r_j} + 2 \right) \right)^{0.5} \right) \frac{r_i}{r_j^2}} \quad (4.6)$$

And, (for $r_i < r_j$)

$$N_{ij} = \frac{0.5(2 - \sqrt{3})N_{ii} \left(\frac{r_j}{r_i} + 1 \right)}{\left(1 + \frac{r_j}{r_i} - \left(\frac{r_j}{r_i} \left(\frac{r_j}{r_i} + 2 \right) \right)^{0.5} \right) \frac{r_j}{r_i^2}} \quad (4.7)$$

$$N_{ji} = \frac{0.5(2 - \sqrt{3})N_{ii} \left(\frac{r_j}{r_i} + 1 \right)}{\left(1 + \frac{r_j}{r_i} - \left(\frac{r_j}{r_i} \left(\frac{r_j}{r_i} + 2 \right) \right)^{0.5} \right) \frac{r_j}{r_i^2}} \quad (4.8)$$

Where,

$$N_{jj} = N_{ii} = N_c = 6$$

Percolation probability is given as equation (4.9) using Z_{ii} from equation (4.10)

$$P_i = 1 - \left(\frac{4.236 - Z_{ii}}{2.472} \right)^{3.7} \quad (4.9)$$

Where,

$$Z_{ii} = S_i N_{ii} \quad (4.10)$$

Electrochemical performance modelling requires the triple phase boundary area (A_{TPB}) and triple phase boundary length (L_{TPB}) expressions depending upon the exchange current density units. Electrochemical active area (triple phase boundary area) for the anode is given by the equation (4.11), where the pore phase is assumed to be percolated in the electrode microstructure, so the reacting chemical species will be available at the TPB area making it as effective reactive area for the electrochemical reactions.

$$A_{TPB} = \pi K \min(r_i, r_j)^2 n_t n_i P_i P_j Z_{ij} \quad (4.11)$$

Where, $K = \sin^2 \frac{\theta}{2}$

The triple phase boundary length is given as (equation 4.12),

$$L_{TPB} = 2\pi r_i \sin \frac{\theta}{2} n_t n_i P_i P_j Z_{ij} \quad (4.12)$$

Interphase surface area: The interface area between electron and ion conducting phases is proportional to the cross sectional area (equation 4.14) between the particles, coordination number and, the total number of electron or ion conducting particles per unit volume and it is given as (equation 4.13) (5).

$$S_{ij}^V = a_{ij} n_i^V Z_{ij} \quad (4.13)$$

$$a_{ij} = \pi (\min(r_i, r_j) \sin \theta / 2)^2 \quad (4.14)$$

Where one phase will be the electron conducting particles (nickel) and the other one consists of the ion conducting particles (YSZ). The nickel-pore interface area is evaluated by subtracting the surface area of nickel particles lost due to the Ni-Ni interfaces and the Ni-YSZ interfaces from the total surface area of nickel particles (Figure 4.1). In this figure, the black surface of the nickel particle shows the nickel-pore interface (equation 4.15).

$$S_{Ni-Pore} = [n_t n_{Ni} 4\pi r_{Ni}^2] - [n_t n_{Ni} Z_{Ni-Ni} 2\pi (1 - \cos \theta / 2) r_{Ni}^2] - [n_t n_{Ni} Z_{Ni-YSZ} 2\pi (1 - \cos \theta / 2) (\min(r_{Ni}, r_{YSZ}))^2] \quad (4.15)$$

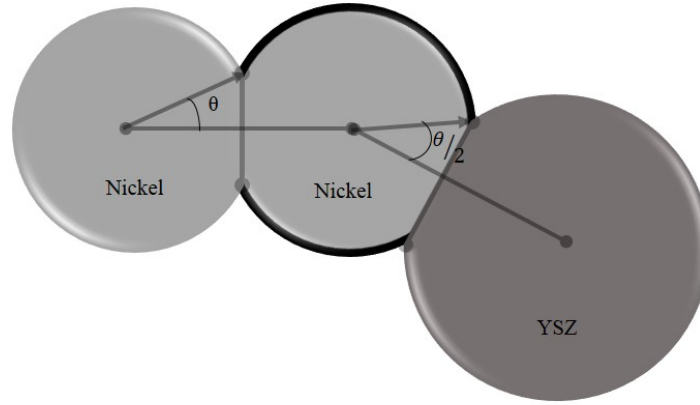


Figure 4.1 Nickel particle surface area covered by Nickel and YSZ; and exposed to pore

4.2.2 Microstructural modelling with structural degradation

In this section, the variation of microstructural properties due to nickel coarsening and carbon formation on nickel particles is investigated using the microstructural model presented in the previous section.

4.2.2.1 Microstructural modelling with nickel coarsening

Nickel particle size has been observed to increase due to nickel coarsening during cell operation and Faes et al. (40) gave an expression (equation 4.16) for the same as:

$$r_{Ni}(t) = (r_{Ni}^{max} - r_{Ni}^o)(1 - \exp(-k_s t)) + r_{Ni}^o \quad (4.16)$$

Where, $r_{Ni}(t)$ the radius of nickel particle at time t, r_{Ni}^o is the initial size of nickel particle, r_{Ni}^{max} is the maximum size nickel particle can attain after coarsening and k_s is growth constant given as $2 \times 10^{-3} h^{-1}$. The maximum size of nickel particles after coarsening is limited due to the zirconia framework in anode substrate. It has been observed that nickel particle size generally increases to 30% of the initial size (40). Sharma and Basu (73) gave the following expression (equation 4.22) for the coordination number with change in microstructure due to nickel coarsening (73). We further modify these expressions (including the nickel particle size variation due to coarsening)(equation 4.17- 4.23) based on the relations given by Bertei et al.(4)

$$Z_{Ni-YSZ} = S_{YSZ} N_{Ni-YSZ} \quad (4.17)$$

$$S_{YSZ} = \left[\frac{\psi_{YSZ}/r_{YSZ}}{\psi_{YSZ}/r_{YSZ} + \psi_{Ni}/r_{Ni}(t)} \right] \quad (4.18)$$

If $r_{Ni}(t) > r_{YSZ}$

$$r_{Ni}(t) = (r_{Ni}^{max} - r_{Ni}^o)(1 - \exp(-k_s t)) + r_{Ni}^o \quad (4.19)$$

$$N_{Ni-YSZ} = \frac{0.5(2 - \sqrt{3})N_{Ni-Ni} \left(\frac{r_{Ni}(t)}{r_{YSZ}} + 1 \right)}{1 + \frac{r_{Ni}(t)}{r_{YSZ}} - \left(\frac{r_{Ni}(t)}{r_{YSZ}} \left(\frac{r_{Ni}(t)}{r_{YSZ}} + 2 \right) \right)^{0.5}} \quad (4.20)$$

If $r_{Ni}(t) < r_{YSZ}$

$$N_{Ni-YSZ} = \frac{0.5(2 - \sqrt{3})N_{YSZ-YSZ} \left(\frac{r_{YSZ}}{r_{Ni}(t)} + 1 \right)}{\left(1 + \frac{r_{YSZ}}{r_{Ni}(t)} - \left(\frac{r_{YSZ}}{r_{Ni}(t)} \left(\frac{r_{YSZ}}{r_{Ni}(t)} + 2 \right) \right)^{0.5} \right) \frac{r_{YSZ}}{r_{Ni}(t)}} \quad (4.21)$$

$$Z_{Ni-Ni} = N_{Ni-Ni} \left[\frac{\psi_{Ni}/r_{Ni}(t)}{\psi_{Ni}/r_{Ni}(t) + \psi_{YSZ}/r_{YSZ}} \right] \quad (4.22)$$

$$Z_{YSZ-YSZ} = N_{YSZ-YSZ} \left[\frac{\psi_{YSZ}/r_{YSZ}}{\psi_{Ni}/r_{Ni}(t) + \psi_{YSZ}/r_{YSZ}} \right] \quad (4.23)$$

Where Z is the average co-ordination number, r_{YSZ} radius of YSZ particle, ψ_{Ni} and ψ_{YSZ} are the volume fraction of nickel and YSZ, respectively. Percolation probabilities of the nickel and YSZ particles can be evaluated using equation 4.9 and above co-ordination number expressions (equation 4.22 and 4.23).

The electrochemically active area will vary due to the change in coordination number and percolation probability with time and it can be expressed as (equation 4.24)

$$A_{TPB} = \pi \min(r_{Ni}(t), r_{YSZ})^2 n_t n_{Ni} P_{Ni} P_{YSZ} Z_{Ni-YSZ} \quad (4.24)$$

Where, $r_{Ni}(t)$ nickel particle size at any time t, r_{YSZ} is the size of YSZ particles, n_t is the total number of particles per unit volume, n_{Ni} is the number fraction of nickel particles, Z_{Ni-YSZ} is the coordination number between nickel and YSZ particles, P_{Ni} and P_{YSZ} are the percolation probabilities of the nickel and YSZ phases, respectively.

Although the porosity remains constant during nickel coarsening, the pore size changes due to variation in nickel particle size as given by Farhad and Hamdullahpur (21)(equation 4.25):

$$r_{pore} = \frac{2}{3} \left(\frac{1}{1 - \varepsilon} \right) \left(\frac{1}{\psi_{YSZ}/r_{YSZ} + \psi_{Ni}/r_{Ni}(t)} \right) \quad (4.25)$$

The tortuosity is estimated using the following expression (equation 4.26):

$$\tau = \frac{\varepsilon}{\frac{\pi}{4} d_{pores}^2 n_t^{2/3}} \quad (4.26)$$

Interface surface areas can be calculated from the expressions similar to the ones discussed in the last section. The nickel-YSZ interface area is given by following expression (equation 4.27 and 4.28).

$$S_{Ni-YSZ}^V = a_{Ni-YSZ} n_{Ni}^V Z_{Ni-YSZ} \quad (4.27)$$

$$a_{Ni-YSZ} = \pi (\min(r_{Ni}(t), r_{YSZ}) \sin \theta/2)^2 \quad (4.28)$$

Nickel-pore interface area with coarsening of nickel particles is expressed as (equation 4.29),

$$S_{Ni-Pore} = [n_t n_{Ni} 4\pi r_{Ni}^2] - [n_t n_{Ni} Z_{Ni-Ni} 2\pi (1 - \cos \theta/2) r_{Ni}^2] - [n_t n_{Ni} Z_{Ni-YSZ} 2\pi (1 - \cos \theta/2) (\min(r_{Ni}, r_{YSZ}))^2] \quad (4.29)$$

Effective conductivity variation for nickel and YSZ in anode with coarsening phenomenon can be given using the expressions (equation 4.30 and 4.31), where we have used the Bruggeman factor value of 3.5 (this value accounts for the tortuous path for the conducting of electrons) as suggested by Sanyal et al. (8)

$$\sigma_{Ni}^{eff} = \sigma_{Ni} [(1 - \varepsilon) \psi_{Ni} P_{Ni}]^{3.5} \quad (4.30)$$

$$\sigma_{YSZ}^{eff} = \sigma_{YSZ} [(1 - \varepsilon) \psi_{YSZ} P_{YSZ}]^{3.5} \quad (4.31)$$

Where pure electronic conductivity of nickel and YSZ are given as (equation 4.32 and 4.33),

$$\sigma_{Ni} = 3.27 \times 10^6 - 1065.3 T \quad (4.32)$$

$$\sigma_{YSZ} = 3.34 \times 10^4 \exp\left(\frac{-10300}{T}\right) \quad (4.33)$$

4.2.2.2 Microstructural modelling with carbon deposition

Carbon poisoning of nickel particles in anode degrades the anode performance due to decrease of porosity and the decrease in the catalyst activity due to the coverage of nickel particles. In this part, we extend our model to investigate the effect of carbon formation on microstructural properties. In this work, we have assumed uniform distribution of carbon on all the nickel particles. Carbon coverage is assumed to be all around the nickel particle (Figure 4.3) as observed from experimental studies by Chen et al. (133) (Figure 4.2).

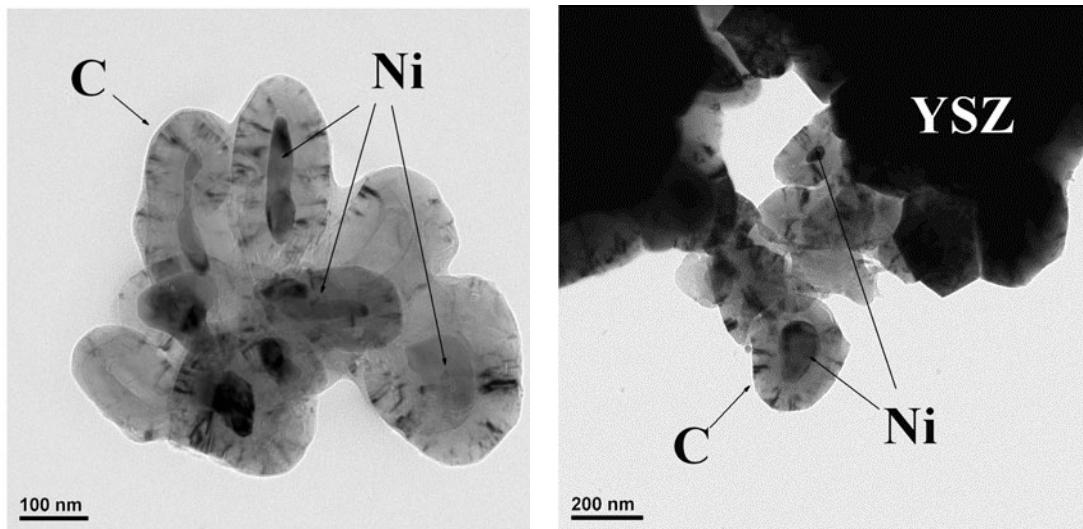


Figure 4.2 Carbon distribution over nickel particles, Reprinted with permission from ref (133) Copyright 2011 Elsevier.

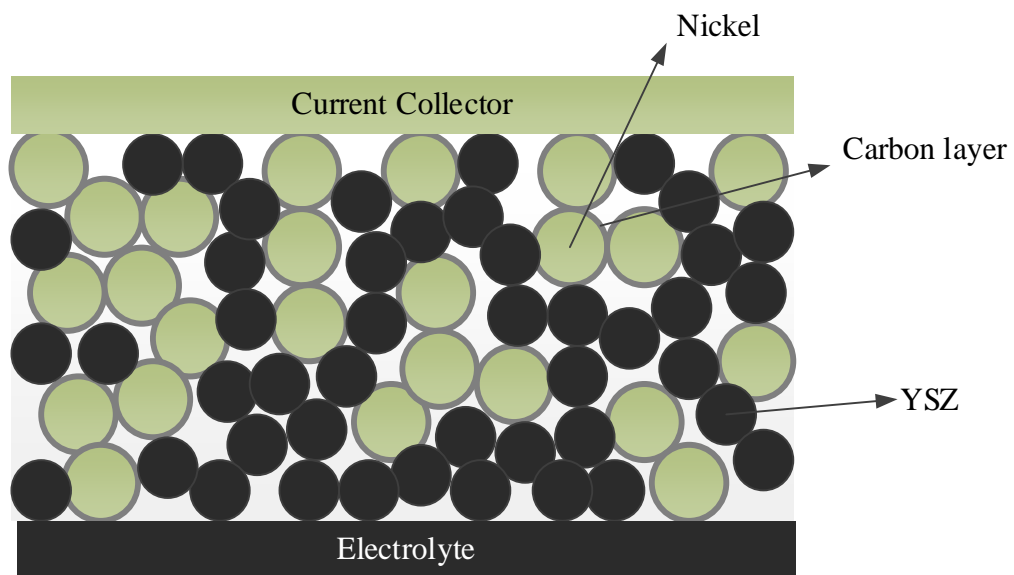


Figure 4.3 Schematic of anode where nickel particles are covered by carbon.

The amount of carbon deposited can be obtained from the reaction kinetics of carbon forming reactions such as methane cracking, Boudouard reaction etc. We have included the carbon effect in this study using the volume fraction of carbon in anode that can be obtained using the density of carbon. Anode porosity decreases by the amount of volume fraction of carbon formed, now the new porosity (equation 4.34) can be expressed as:

$$\varepsilon = \varepsilon_o - \psi_c \quad (4.34)$$

Where ε is the anode porosity, ε_o is the initial anode porosity and ψ_c is the volume fraction of carbon in anode.

Due to electron conducting nature of carbon, the electron conducting phase consists of nickel particle and carbon layer on it. Therefore the electron conducting phase particle size (r_{Ni_c}) increases, and it is expressed as (equation 4.35):

$$r_{Ni_c} = r_{Ni_o} \times \left(1 + \frac{\psi_c}{\psi_{Ni_o}}\right)^{(1/3)} \quad (4.35)$$

Carbon formed will contribute to the electron conducting phase in anode. So the volume fractions of electron (ψ_{Ni_c}) and ion conducting phases (ψ_{YSZ}) will be changing and these are expressed as (equation 4.36 and 4.37) :

$$\psi_{Ni_c} = \frac{\psi_{Ni_o} + \psi_c}{\psi_{Ni_o} + \psi_c + \psi_{YSZ_o}} \quad (4.36)$$

$$\psi_{YSZ} = \frac{\psi_{YSZ_o}}{\psi_{Ni_o} + \psi_c + \psi_{YSZ_o}} \quad (4.37)$$

Co-ordination number between electron conducting and ion conducting phases will also change with the amount of carbon. This change in coordination number is expressed in the following equations (4.38 - 4.40) using the revised expressions (equation 4.36-4.37) for volume fractions and particle sizes.

$$Z_{Ni_c-YSZ} = S_{YSZ} N_{Ni_c-YSZ} \quad (4.38)$$

$$Z_{Ni_c-Ni_c} = N_{Ni-Ni} \left[\frac{\psi_{Ni_c}/r_{Ni_c}}{\psi_{Ni_c}/r_{Ni_c} + \psi_{YSZ}/r_{YSZ}} \right] \quad (4.39)$$

$$Z_{YSZ-YSZ} = N_{YSZ-YSZ} \left[\frac{\psi_{YSZ}/r_{YSZ}}{\psi_{Ni_c}/r_{Ni_c} + \psi_{YSZ}/r_{YSZ}} \right] \quad (4.40)$$

Electrochemical active area, since the carbon is an electron conducting phase so the contact points between carbon covered nickel particles and YSZ particles will contribute to the TPB and hence electrochemical active area is expressed as (equation 4.41):

$$A_{TPB} = \pi \min(r_{Ni_c}, r_{YSZ})^2 n_t n_{Ni_c} P_{Ni_c} P_{YSZ} Z_{Ni_c-YSZ} \quad (4.41)$$

Carbon deposition will lead to decrease in anode porosity and consequently the pore size will be decreasing is given as (equation 4.42)

$$r_{pore} = \frac{2}{3} \left(\frac{1}{1 - \varepsilon} \right) \left(\frac{1}{\psi_{YSZ}/r_{YSZ} + \psi_{Ni_c}/r_{Ni_c}} \right) \quad (4.42)$$

Tortuosity in the anode for the species transport will be varying due to change in pore size is expressed as (equation 4.43)

$$\tau \approx \frac{\varepsilon}{\frac{\pi}{4} d_{pores}^2 n_t^{2/3}} \quad (4.43)$$

Interface surface area between the electron and ion conducting phases can be evaluated using expression below (equation 4.44 and 4.45)

$$S_{Ni_c-YSZ}^V = a_{Ni_c-YSZ} n_{Ni_c}^V Z_{Ni_c-YSZ} \quad (4.44)$$

$$a_{Ni_c-YSZ} = \pi (\min(r_{Ni_c}, r_{YSZ}) \sin \theta / 2)^2 \quad (4.45)$$

However, the surface between nickel and pore will reduce to zero with little amount of carbon formation since all the nickel particles are assumed to be uniformly deposited with carbon.

There will be a change in the conductivity of the electronic conducting phase. Initially, it was the electronic conductivity of solid nickel particles σ_{Ni} . The effective electronic conductivity of electron conducting particle after carbon deposition can be evaluated by the expression below (equation 4.46):

$$\frac{1}{\sigma_{Ni_c}} = \rho_{Ni_c} = \rho_{Ni} + \left[(\rho_c - \rho_{Ni}) \left(\frac{r_{Ni_c} - r_{Ni}}{Ni_c} \right) \right] \quad (4.46)$$

Now the effective conductivity of electron and ion conducting phase can be determined using equations 4.30 and 4.31. All the above-described equations have been solved with increasing amount of carbon volume fraction in the anode to obtain the influence of carbon deposition on microstructural properties.

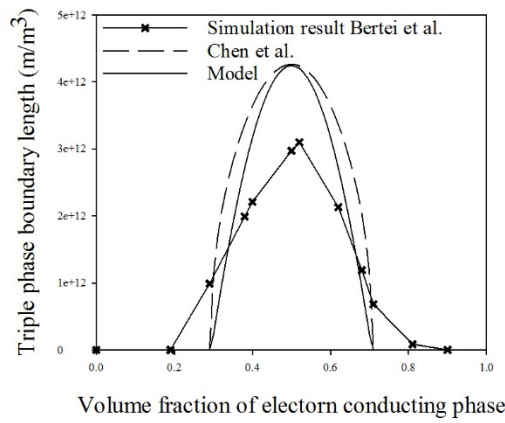
4.3 Results and Discussions

4.3.1 Anode microstructural properties

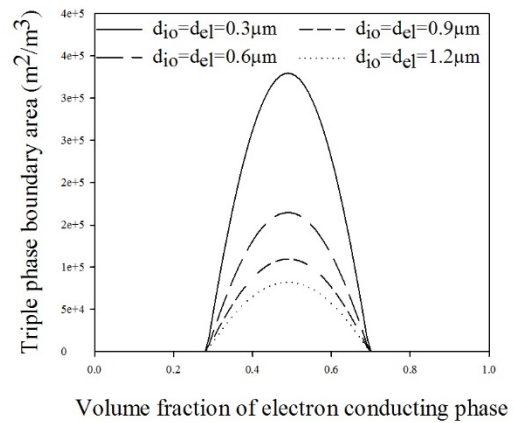
Our micromodel provides the variation of properties with controllable microstructural parameters like particle size, volume fraction of individual phase, porosity and particle size ratio. In Figure 4.4(a), TPB length is evaluated and compared with the microstructural model developed by Chen et al.(5) and with the simulation results from Sanyal et al. (8). Our results match very well with results from other models and show comparatively more proximity with simulation results. We have shown that the TPBL results here to compare favourably with earlier reported results. Further, we evaluate the triple phase boundary area due to its wide application in electrochemical performance modelling. Figure 4.4(b & c) shows the effect of microstructural parameters on the triple phase boundary area. It can be observed from the results that the triple phase boundary area is maximised at equal volume fraction, and equal sizes of electron and ion conducting particles. Triple phase boundary area expeditiously decreases near the threshold volume fraction of particles (Figure 4.4 (b)) and, this threshold volume fraction is dependent upon the size ratio of particles. The triple phase active area is found to increase swiftly with decreasing particle size (Figure 4.4 (e)) that also qualitatively matches with our experimental results as discussed in Chapter-3. The TPB area is also observed to decrease linearly with increase in electrode porosity (Figure 4.4(d)).

Nickel-pore interface area is an important parameter that has been mostly ignored in modelling studies till now. Nickel-pore interface provides the active catalytic area for the steam reforming reaction and methane cracking reaction during the use of hydrocarbon fuels in the anode. Nickel-pore interface also needs to be optimised as it is the active area for reforming reactions. The nickel-pore interface is found to increase rapidly with decrease of particle size (Figure 4.5(a)) and it increases linearly with the increase in nickel volume fraction (Figure 4.5(b)).

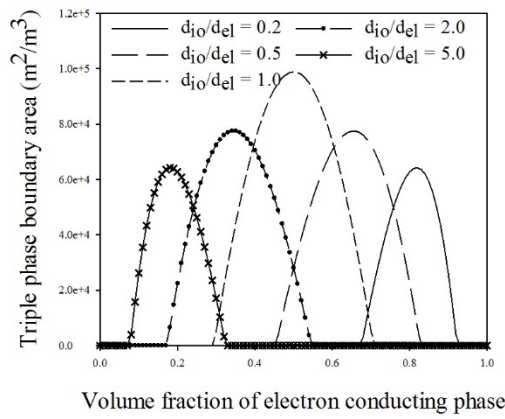
The pore size has an influence on the concentration polarisation in the electrode. It is observed to increase with increasing particle size and with increasing particle size ratio. Although decrease in particle size results in increase in electrochemical active area, it leads to decrease in pore size and hence increase in concentration polarisation.



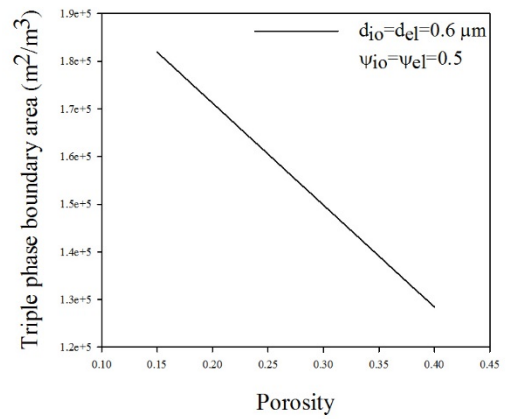
(a)



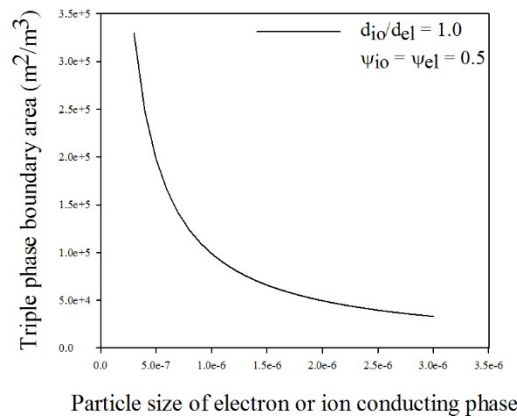
(b)



(c)



(d)



(e)

Figure 4.4 Triple phase boundary length variation with volume fraction (a), Triple boundary area variation with volume fraction and size of particles (b), with volume fraction and size ratio of particles (c), with porosity(d), with particle size (e)

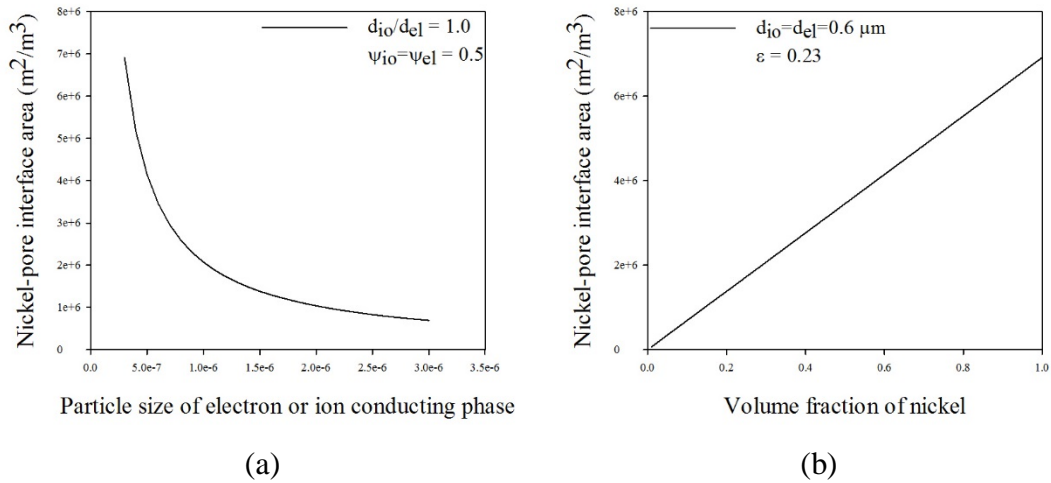


Figure 4.5 Nickel-pore interface area variation with particle size (a), with nickel volume fraction (b)

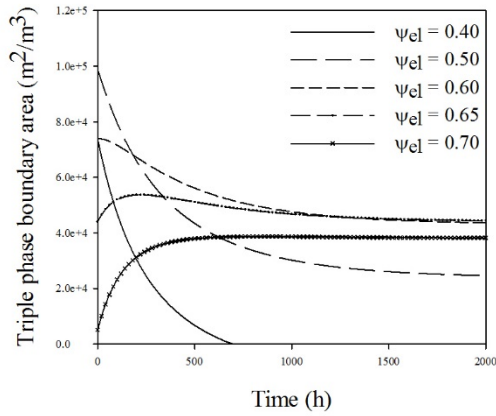
4.3.2 Anode microstructural properties with nickel coarsening

This model also enables us to investigate the behaviour of properties after cell operation and the changes induced due to nickel coarsening. Nickel particle coarsening results in increasing the size of particles that leads to a decrease in the electrochemically active area. The electrochemical active area diminishes to zero after around 700 hours of operation if only 40% volume of nickel is used (Figure 4.6 (a)). It has been observed that there is no significant change in electrochemical active area at higher nickel volume fractions. This analysis can help to determine the optimum amount of nickel in anode for achieving minimum TPB degradation in anode. It is observed that around 65% of nickel volume fraction, the electrochemical active area variation is minimum with time. However, higher volume fractions of nickel particles may result in structural degradation due to stresses induced by thermal coefficient mismatch of nickel and YSZ (49). In further development of the modelling techniques, structure stability parameter should be considered for electrode microstructure optimisation. Nickel-pore interface area (Figure 4.6(b)) is found to decrease with time due to nickel particle coarsening. Nickel coarsening leads to agglomeration of nickel particles resulting in larger nickel particle sizes that consequently leads to decrement of nickel-pore interface area. Pore size (Figure 4.6(c)) is found to increase with time due to increase in size of nickel particles. The

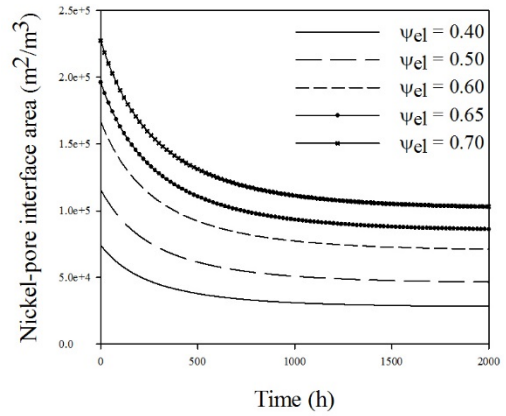
nickel coarsening will help in reducing concentration polarisation but at the same time will decrease the TPB area and nickel-pore interface area.

Nickel volume fraction should be more than 50% for minimum variation of electrochemical active area and at the same time increasing the pore size with operation time. Tortuosity (Figure 4.6 (d)) decreases with nickel coarsening due to increase in porosity. The amount of decrease of tortuosity with coarsening is higher with a higher volume fraction of nickel in the anode and it becomes constant after long operation time.

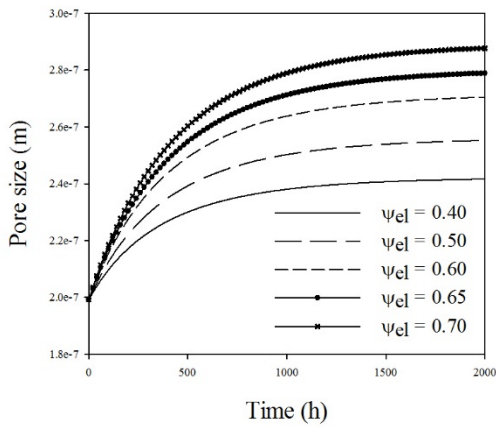
Conductivity (Figure 4.6 (e)) is observed to decrease with coarsening of nickel particles. Since coarsening leads to decrease in the particle size ratio, it affects the percolation of particles leading to decrease in conductivity. However, at the higher volume fractions of the nickel particles this rate of decrement in conductivity decreases. Threshold volume fraction of nickel particle for electronic conductivity at initial composition will lead to zero electronic conductivity in electrode after a while as observed in Figure 4.6(e). So higher volume fractions of nickel are favourable to maintain constant conductivity during cell operation. However it needs to be optimised such that the volume fraction of ion conducting phase is above the threshold volume fraction.



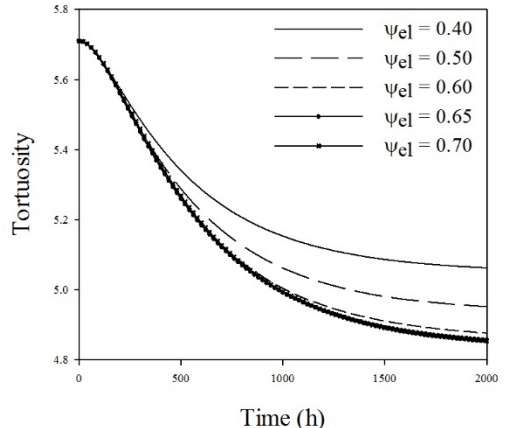
(a)



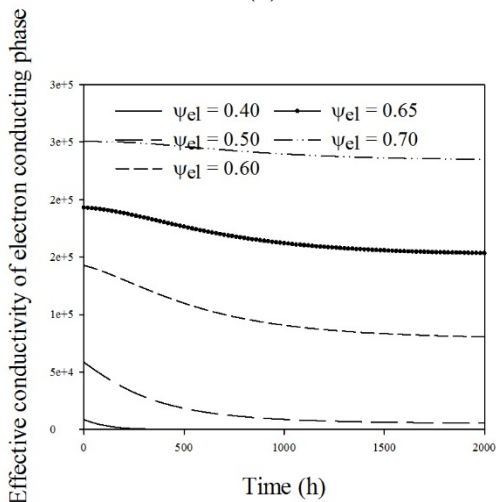
(b)



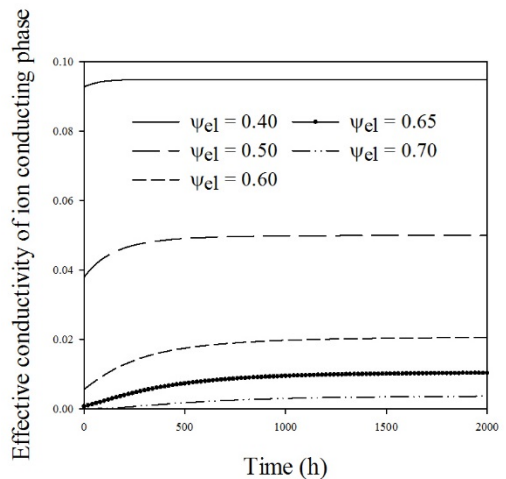
(c)



(d)



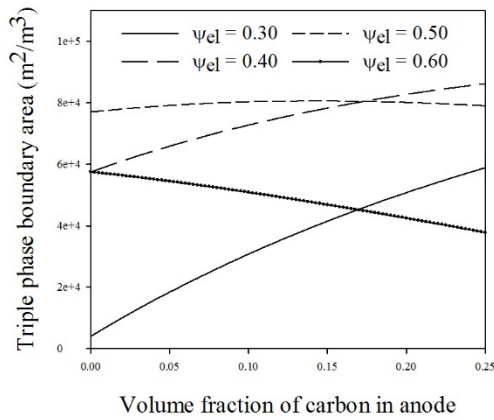
(e)



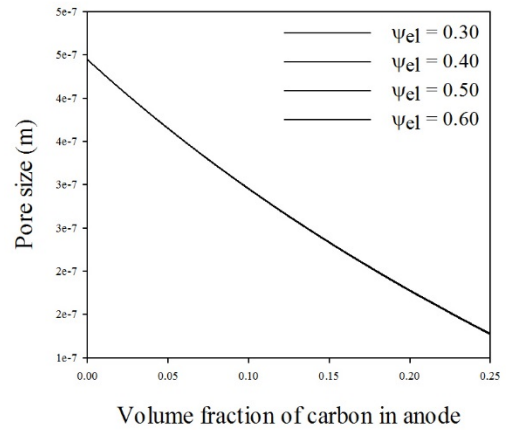
(f)

Figure 4.6 Nickel coarsening effect on TPB area (a), Ni-pore area (b), pore size (c), tortuosity (d), effective conductivity of e⁻ conducting (e) and, ion conducting phase

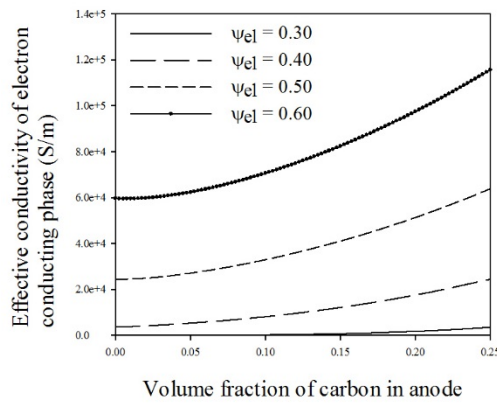
(f)



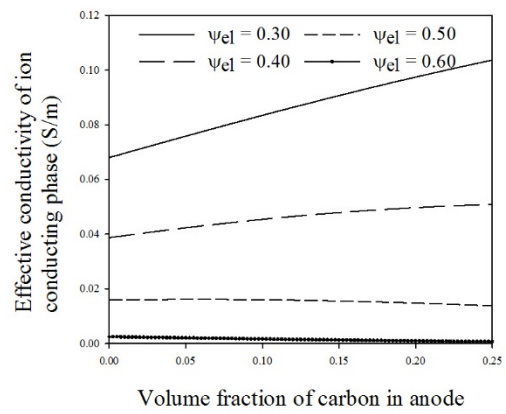
(a)



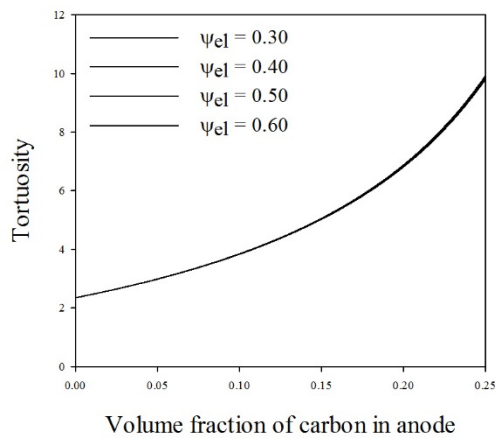
(b)



(c)



(d)



(e)

Figure 4.7 Carbon effect ($\epsilon_o=0.23$) on TPB area(a), pore size(b), effective conductivity of electron conducting phase(c), ion conducting phase(d) and, tortuosity (e)

4.3.3 Anode microstructure properties with carbon poisoning

Carbon poisoning on anode nickel particles is a serious issue during the use of hydrocarbon fuels. Carbon deposition on the nickel particle surface affects the electrochemical active area, and this active area (Figure 4.7 (a)) is observed to increase for lower volume fraction of nickel particles and to decrease for higher volume fraction of nickel. For lower volume fraction of nickel, carbon deposition on nickel particle surface leads to increase in the volume of electron conducting particles and therefore increase in electrochemical active area. While using higher amounts of nickel, carbon deposition affects the threshold volume fraction of ion conducting phase and hence reduces the triple phase boundary area. In the case of carbon poisoning of nickel particles, a small amount of carbon will cover the surface of all nickel particles since we have assumed the uniform distribution of carbon formation over nickel particles.

Carbon formation in the anode will decrease the porosity in anode and hence the pore size (Figure 4.7 (c)) hindering the fuel species transport. Tortuosity (Figure 4.7 (e)) is found to increase due to the decrease in pore size. It has been observed that the effective conductivity of electron conducting phase (Figure 4.7(b)) will increase due to increase in the volume of electron conducting phase. The effective conductivity of the ion conducting phase (Figure 4.7 (d)) is decreasing due to decrease in the volume fraction of ion conducting phase. There is no experimental data available to directly validate our work. Although there are some experimental evidences where the conductivity of anode is observed to increase with carbon deposition (134). This behaviour of increase in conductivity is similar to our modelling results. In addition, carbon formation will lead to decrease in pore size, which can also be observed from several experimental studies (127, 133, 134).

4.4 Conclusions

A microstructure model has been developed using the corrected percolation probability and co-ordination number expressions to determine the anode microstructural properties. These microstructural properties (electrochemical active area, interphase surface area, pore size, tortuosity and effective conductivity) are important for the anode performance optimisation and depend upon the microstructural parameters (volume fraction, particle size, size ratio and porosity).

This model provides the way to quantify these microstructural properties with microstructural parameters. It is observed that equal volume fraction, equal particle sizes and the possible smallest size of particles are preferred for the maximisation of the electrochemical active area. However, the smaller particle sizes results in smaller pore sizes and must be optimised for concentration polarisation. This microstructure model is further extended to study the effect of nickel coarsening and carbon deposition on microstructural properties. This model suggests usage of higher volume fraction (more than 50%) of nickel for obtaining stable electrochemical active area. Electrochemical area variation is minimum for 65% volume fraction of nickel particles. However, the higher volume fractions of nickel particle may result in structural stresses due to the thermal coefficient mismatch of nickel and YSZ. This model should be further developed accounting for the structural stresses of particles induced due to different thermal expansion coefficients. In the study of microstructural properties variation with carbon deposition, it is observed that electrochemical active area is constant with 50% volume fraction of nickel particles. Nickel coarsening results in the increase of pore radius and carbon deposition results in the decrease of pore radius. The pore radius parameters along with the degradation parameters should be optimised for the minimisation of concentration polarisation. Effective conductivity is found to increase with carbon deposition and decrease with nickel coarsening. The developed model gives us quantitative relationships between microstructural properties and degradation parameters that can be further included in anode performance modelling for obtaining optimised performance.

Chapter 5

Modelling of multicomponent mass transport and carbon deposition in SOFC anode

5.1 Introduction

In the SOFC, all reactant and product species diffuse through the anode and react chemically and electrochemically in the anode. When the hydrocarbon fuels are utilised, several chemical reactions occur in the anode due to the availability of nickel catalyst. In this chapter, we model the diffusive flow of fuel species through the anode while considering the chemical reactions involved at the catalytic active surfaces in the anode and electrochemical reaction at the anode-electrolyte interface. We also investigate the effect of the anode microstructure on species transport and species distribution in the anode. In the Ni-YSZ anode, nickel not only provides the catalytic sites for steam methane reforming reaction, but also catalyses the carbon forming reactions (methane cracking and Boudouard reactions). This carbon formation in the anode deactivates the catalytic active surface and reduces the porous volume in the anode. This decrease in porosity due to the carbon formation results into higher concentration polarisation for the anode.

In this chapter, we are using CFD techniques for representative anode microstructure to investigate the effect of local heterogeneity and microstructure effect on the mass transport and species distribution. We investigate the effect of porosity on the species transport and species distribution in the anode. We also investigate the effect of the gas-solid interface area on the species distribution.

5.2 Model development

To consider the effect of microstructure on the mass transport, involved chemical and electrochemical processes, we have considered a representative microstructure for anode as shown in Figure (5.1) with varying porosities of 0.30, 0.40 and 0.50. In another model geometry, we vary the gas-solid interface area in anode while keeping the porosity constant at 40% (Figure 5.1b and 5.2).

5.2.1 Mass transport model

CFD model has been simulated for mass transport inside the representative anode geometry. Species transport is considered through multicomponent diffusion. We have assumed the isothermal conditions inside the anode for simplicity. To calculate the rate of change of mass fraction of each species in the domain, we have used the following equation (5.1)

$$\frac{\partial}{\partial t}(\rho Y_i) + \nabla \cdot (\rho \vec{v} Y_i) = -\nabla \cdot \vec{J}_i + R_i + S_i \quad (5.1)$$

Where R_i the chemical reaction rate of production or consumption of species, S_i is the generation or consumption term for any species in the system, ρ is the mass density of mixture, v is the velocity term for convective transport and Y_i is the mass fraction of component i . J_i is the diffusion flux of species which arises due to concentration gradient in the domain. We have assumed no convective transport of species in our system and full multicomponent diffusion of species is considered. Maxwell-Stefan equation (equation 5.2) has been used to determine the diffusive mass flux of species (177).

$$\sum_{\substack{j=1 \\ j \neq i}}^N \frac{X_i X_j}{D_{ij}} \left(\frac{\vec{J}_j}{\rho_j} - \frac{\vec{J}_i}{\rho_i} \right) = \nabla X_i - \frac{\nabla T}{T} \sum_{\substack{j=1 \\ j \neq i}}^N \frac{X_i X_j}{D_{ij}} \left(\frac{D_{T,j}}{\rho_j} - \frac{D_{T,i}}{\rho_i} \right) \quad (5.2)$$

X_i is the mole fraction, J_i is the diffusion flux, D_{ij} is the binary mass diffusion coefficient, and $D_{T,i}$ is the thermal diffusion coefficient for species i . D_{ij} is evaluated here using the correlation of Fuller Schettler and Giddings equation (equation 5.3) (178).

$$D_{ij} = \frac{10^{-7} T^{1.75} \left(1/M_i + 1/M_j \right)^{1/2}}{P \left(V_i^{1/3} + V_j^{1/3} \right)^2} \quad (5.3)$$

Where D_{ij} is the binary diffusivity, M_i and M_j are the molar mass of species i and j , V_i and V_j are the molar volume of species i and j , P is pressure (Pa) and T is temperature (K). Binary diffusivities are given as: $D_{H_2-H_2O} = 7.99E-04$, $D_{H_2-CO_2} = 5.87E-04$, $D_{H_2-CO} = 6.95E-04$, $D_{H_2-CH_4} = 6.24E-04$, $D_{CH_4-CO_2} = 1.58E-04$, $D_{CH_4-CO} = 1.92E-04$, $D_{CH_4-H_2O} = 2.32E-04$, $D_{CO_2-CO} = 1.45E-04$, $D_{CO_2-H_2O} = 1.85E-04$, $D_{H_2O-CO} = 2.30E-04$ at $T = 1023$ K.

5.2.2 Chemical model

This part consists of equations that have been used to account for the generation and consumption of individual components due to the chemical reaction involved in the catalyst layers. Here we have considered the methane steam reforming, water gas shift, methane dry reforming, methane cracking and Boudouard reactions in anode catalyst layer.

Methane steam reforming (MSR) reaction: There have been several rate expressions developed and used for methane steam reforming (117) (179). We are using the rate expression for MSR that is widely used for SOFC anode and it is given as equation (5.4)(180).



$$R_{MSR} = k_{rf} \left(P_{\text{CH}_4} P_{\text{H}_2\text{O}} - \frac{P_{\text{CO}} P_{\text{H}_2}^3}{K_{pr}} \right) \quad (5.4)$$

Where,

$$k_{rf} = 2.39 \times 10^3 \times \exp\left(\frac{-2.31 \times 10^5}{RT}\right)$$

$$K_{pr} = 1.0267 \times 10^{10}$$

$$\times \exp(-0.2513\theta^4 + 0.3665\theta^3 + 0.5810\theta^2 - 27.134\theta + 3.2770)$$

$$\theta = \frac{1000}{T(K)} - 1$$

Where the units for R1 is $\text{mol}^{-3}\text{sec}^{-1}$, pressure unit is in Pa, temperature in K and, R is universal gas constant $8.314 \text{ J mol}^{-1} \text{ K}^{-1}$

Water gas shift reaction: Water gas shift reaction rate for catalyst layer is given as equation (5.5) (180)



$$R_{WGS} = k_{sf} \left(P_{\text{H}_2\text{O}} P_{\text{CO}} - \frac{P_{\text{CO}_2} P_{\text{H}_2}}{K_{ps}} \right) \quad (5.5)$$

Where,

$$k_{sf} = 0.0171 \times \exp\left(\frac{-1.03 \times 10^5}{RT}\right)$$

$$K_{ps} = \exp(-0.2935\theta^3 + 0.6351\theta^2 - 4.1788\theta + 0.3169)$$

$$\theta = \frac{1000}{T(K)} - 1$$

Where the units for R2 is $\text{mol}^{-3}\text{sec}^{-1}$, pressure units are in Pa, temperature in K and, R is universal gas constant $8.314 \text{ J mol}^{-1} \text{ K}^{-1}$

Methane dry reforming (MDR): Rate expression for MDR is expressed as equation (5.6) (181)



$$R_{MDR} = \frac{k_{CO_2} K_{CO_2} K_{CH_4} P_{CH_4} P_{CO_2}}{(1 + K_{CO_2} P_{CO_2} + K_{CH_4} P_{CH_4})^2} \quad (\text{5.6})$$

Where,

$$k_{CO_2} = 1.17 \times 10^7 \exp\left(\frac{-8.35 \times 10^4}{RT}\right)$$

$$K_{CO_2} = 3.11 \times 10^{-3} \exp\left(\frac{4.92 \times 10^4}{RT}\right)$$

$$K_{CH_4} = 0.653 \exp\left(\frac{1.60 \times 10^4}{RT}\right)$$

Where the units for R3 is $\text{mol}^{-3}\text{sec}^{-1}$, pressure units are in atm, temperature in K and, R is universal gas constant $8.314 \text{ J mol}^{-1} \text{ K}^{-1}$

Methane cracking reaction: reaction rate expression for methane cracking is given as equation (5.7)(182).



$$R_C = k \frac{P_{CH_4} - \frac{P_{H_2}^2}{K_p}}{(1 + K_H \sqrt{P_{H_2}})^2} \quad (\text{5.7})$$

Where,

$$k = 2.31 \times 10^{-5} \exp\left(20.492 - \frac{1.04 \times 10^5}{RT}\right)$$

$$K_H = \exp\left(\frac{1.63200 \times 10^5}{RT} - 22.426\right)$$

$$K_p = 5.088 \times 10^5 \exp\left(\frac{-9.12 \times 10^4}{RT}\right)$$

Where the reaction rate units for R4 is in terms of gm-moles of carbon formed per unit gm-mass of catalyst per unit second, partial pressure unit is in bar, temperature in K, K_p units are in bar, and k_H is unit less.

Boudouard reaction: the rate of Boudouard reaction is given as equation (5.8) (183).



$$R_B = k_{fb}k_{CO} \frac{P_{CO} - \frac{P_{CO_2}}{K_{pb}}P_{CO}}{\left(1 + k_{CO}P_{CO} + \frac{P_{CO_2}}{k_{CO}k_{CO_2}}P_{CO}\right)^2} \quad (5.8)$$

Where,

$$k_{fb} = 2.67 \times 10^7 \exp\left(\frac{-1.08 \times 10^5}{RT}\right)$$

$$k_{CO} = 1.0245 \times 10^{-6} \exp\left(\frac{9.25 \times 10^4}{RT}\right)$$

$$k_{CO_2} = 3.02 \times 10^7 \exp\left(\frac{-8.98 \times 10^4}{RT}\right)$$

$$K_{pb} = \exp\left(\frac{-1.70 \times 10^2}{R}\right) \exp\left(\frac{1.62 \times 10^5}{RT}\right)$$

Where the units for Boudouard reaction (R5) rate is in moles of carbon formed per unit mass (gm) of catalyst per unit hour, pressure units are in bar, and temperature unit is in K. Carbon formation rate from methane cracking and Boudouard reaction rate expressions are given per unit mass of catalyst. To convert the reaction rates into per unit surface area of catalyst, reaction rate expressions are multiplied by the specific surface area of catalyst. The net rate of carbon formation will be the addition of methane cracking and Boudouard reaction rates.

5.2.3 Electrochemical reaction rate

We have considered the electrochemical reactions to take place at the anode-electrolyte interface, the rate of generation and consumption of species due to the electrochemical reaction are evaluated using the relation given as (equation 5.9):

$$J_{H_2} = -J_{H_2O} = \frac{I}{nF} \quad (5.9)$$

Where I is the current density (A/m²), n is number electron transfer taking place during electrochemical reaction and F is Faraday constant (F=96785 A.sec/mol).

5.3 Model Geometry

The species transport is modelled in the anode while accounting for possible chemical reactions involved (R1, R2, R3, R4 and R5). The anode is represented by the model geometry with varying porosity in the structure and varying gas-solid phase interface area. This representation of electrode is a qualitative representation similar to the ones assumed by Joshi et al. (139) and Xu & Dang (118). In the

following model geometry, the square boxes represent the solid phase in the anode and provide the surface area for chemical reactions. The area (channels) between these square boxes represents the porous zone in the anode for gaseous species diffusion and volumetric reaction. This model geometry (Figure 5.3) represents anode thickness of 750 μm . Three model geometries are created with different porosities for the anode (30%, 40% and 50%) (Figure 5.1) by contracting and expanding the solid phase in anode microstructure. Four different anode microstructures (Microstructure 1,2,3,4) are created by varying the number of square blocks (16, 25, 36, 49 blocks) in the anode geometry hence varying the gas-solid interface area with a constant porosity of 40% (Figure 5.2). Effect of anode porosities is investigated for geometries from Figure 5.1 and the effect of gas-solid interface area is investigated for Figure 5.1(b) geometry called here microstructure 1 and Figure 5.2 geometries (Microstructure 2, 3 and 4).

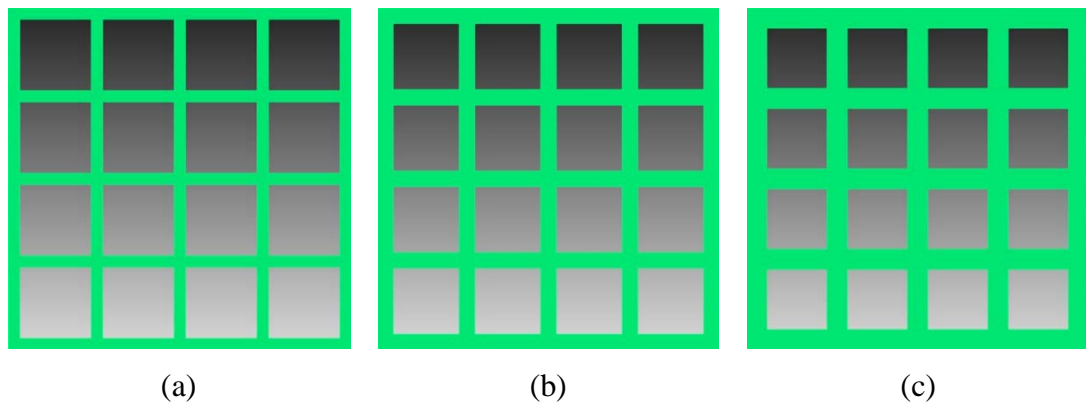


Figure 5.1 Model anode geometry with 30% porosity (a), 40% porosity (Microstructure 1) (b) and, 50% porosity (c)

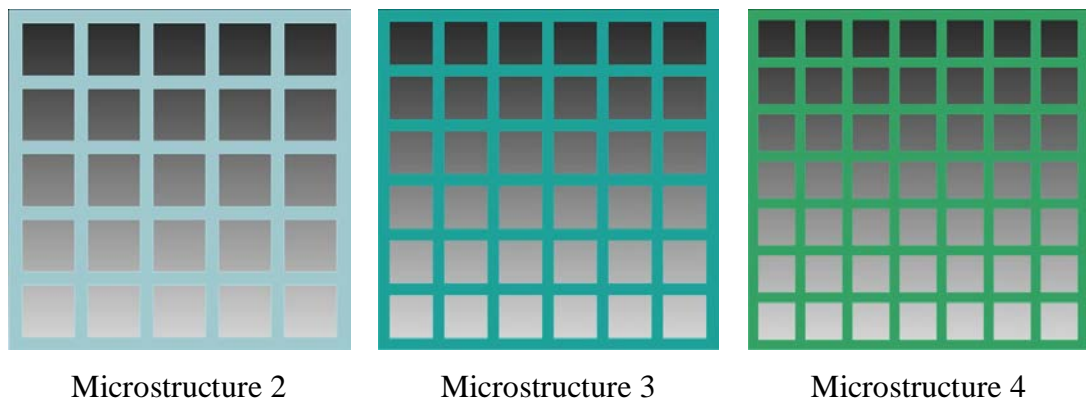


Figure 5.2 Three different microstructures with constant porosity (40%) and increasing gas-solid interface area microstructure 2, microstructure 3, microstructure 4

5.4 Numerical Approach

Among the various commercial packages of CFD, we have used ANSYS Fluent (version 18.1) here to solve the developed model in 2-D space. Geometry and mesh are generated using Trelis (version 15.2). Source terms and reaction rate terms appearing in equation (5.1) are implemented using the user-defined functions programmed in C language. At every iteration step, the species concentration and the thermodynamic state variables are accessed from the solver and used to calculate the output from UDFs. The boundary conditions mentioned in section (5.5) are used for calculations. The model is solved using fixed time step and SIMPLE method for implicit time treatment of variables. Numerical simulations are performed for three different porosity and four different gas-solid interface area microstructures.

5.5 Boundary Conditions

Periodic boundary conditions have been assumed at the top and bottom boundaries of geometry. Molar concentrations of inlet fuel species are known at the fuel-channel/anode interface and the electrochemical reaction rate at the anode/electrolyte interface determines the flux of participating species in the electrochemical reaction (Figure 5.3). Input parameters for these simulations are: pressure = 101325 Pa, Temperature = 1023 K, $I = 13000 \text{ A/m}^2$ Fuel composition $\text{H}_2 = 30.0\%$, $\text{CO} = 3.3\%$, $\text{CH}_4 = 19.4\%$, $\text{CO}_2 = 5.0\%$ and $\text{H}_2\text{O} = 42.2\%$.

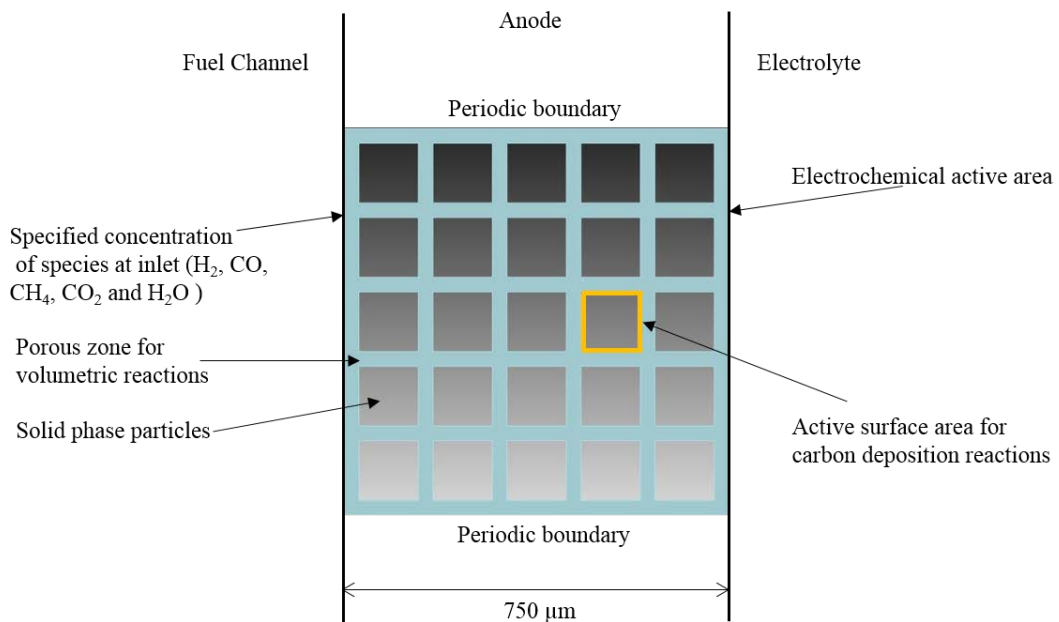


Figure 5.3 Model geometry to represent anode microstructure and boundary conditions

5.6 Results and Discussion

The anode porosity and microstructure can be controlled during the synthesis process of the anode. We investigate the effect of anode microstructure on the mass transport and distribution of chemical species in the anode. Species transport takes place through the pore space in model geometry and the chemical reactions take place in the porous anode domain and at the gas-solid interface. We have run the CFD simulation for fifty seconds to reach the steady-state distribution of species in the anode. We perform these simulations with a current density of 13000 A/m² at anode-electrolyte interface. Species distribution contours of H₂, CO, CH₄, CO₂ and H₂O are shown in Figure 5.4, where $x=0$ is the fuel channel-anode interface and $x=0.75$ is the anode-electrolyte interface.

We can observe from Figure 5.5 (microstructure 2 with 40% anode porosity) that there is little effect of the chemical reaction rates on the species distribution in the anode. The mole fraction of all chemical species is observed to be more or less linear with the anode thickness. If reaction rates would have affected the species distribution, then there must have been some deviation from linearity in mole fraction distribution curves along the anode thickness. It suggests that the concentration of species in the anode at TPB is much more governed by diffusion of species and not much affected by chemical reactions involved in the anode domain. We can also observe that the mole fraction of water vapour is very close to unity at the anode-electrolyte interface. We speculate that the main reason for this higher concentration of water vapour is due to the lower diffusion rate of water molecules.

We can observe the effect of anode porosity on species distribution in Figure 5.6. It can be observed from Figure 5.6 (a-e), that the mole fraction of H₂, CO, CH₄, CO₂ increases and H₂O mole fraction decrease at the anode-electrolyte interface with increase in porosity. This increase in porosity leads to decrease in a concentration gradient of species and hence decrease in the concentration polarisation in the anode.

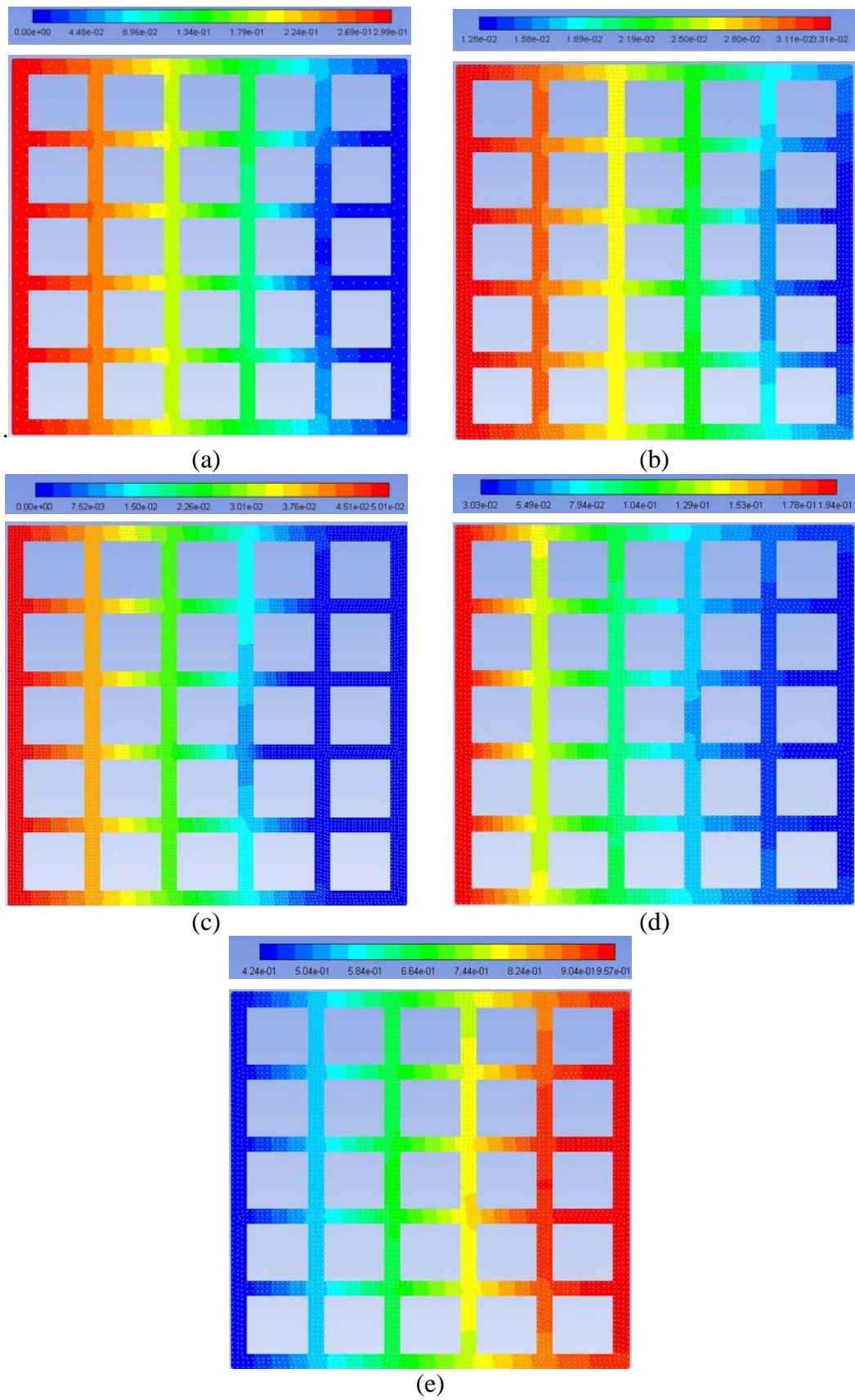


Figure 5.4 Molar fraction distribution of H_2 (a), CO (b), CO_2 (c), CH_4 (d), and H_2O (e) in porous anode along the anode thickness

We investigate the effect of gas-solid interface area on species distribution. It can be observed from Figure 5.7 that there is a slight change in mole fraction of H_2 , CO , CH_4 , CO_2 and H_2O with increase in gas-solid interface area. Since we keep the porosity constant and increase the gas-solid interface area from microstructure 1 to microstructure 4; that results in the change of heterogamous chemical reaction rates in the anode. As we observed in Figure 5.5 (a-e) that species distribution is mainly affected by diffusion and not much by reaction rates, here observe only a slight difference in species distribution with the increase in chemical reaction rates.

The effect of microstructure on carbon deposition rates is also investigated. It can be observed from Figure 5.6 (f), that carbon deposition rates are comparatively less for higher anode porosity. With the constant porosity in anode and with the increase in gas-solid interface, an increase of carbon deposition rates is observed. It is also observed that the carbon deposition rates are higher at inlet side of anode. This suggests that maintaining high porosity in the initial thickness of anode reduces the carbon formation.

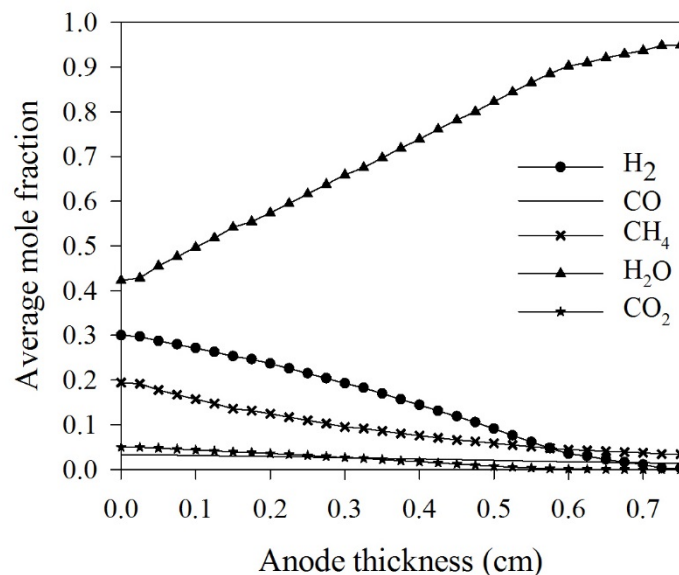


Figure 5.5 Average mole fraction of H_2 , CO , CH_4 , H_2O , CO_2 in porous anode with chemical and electrochemical reactions at the anode-electrolyte interface

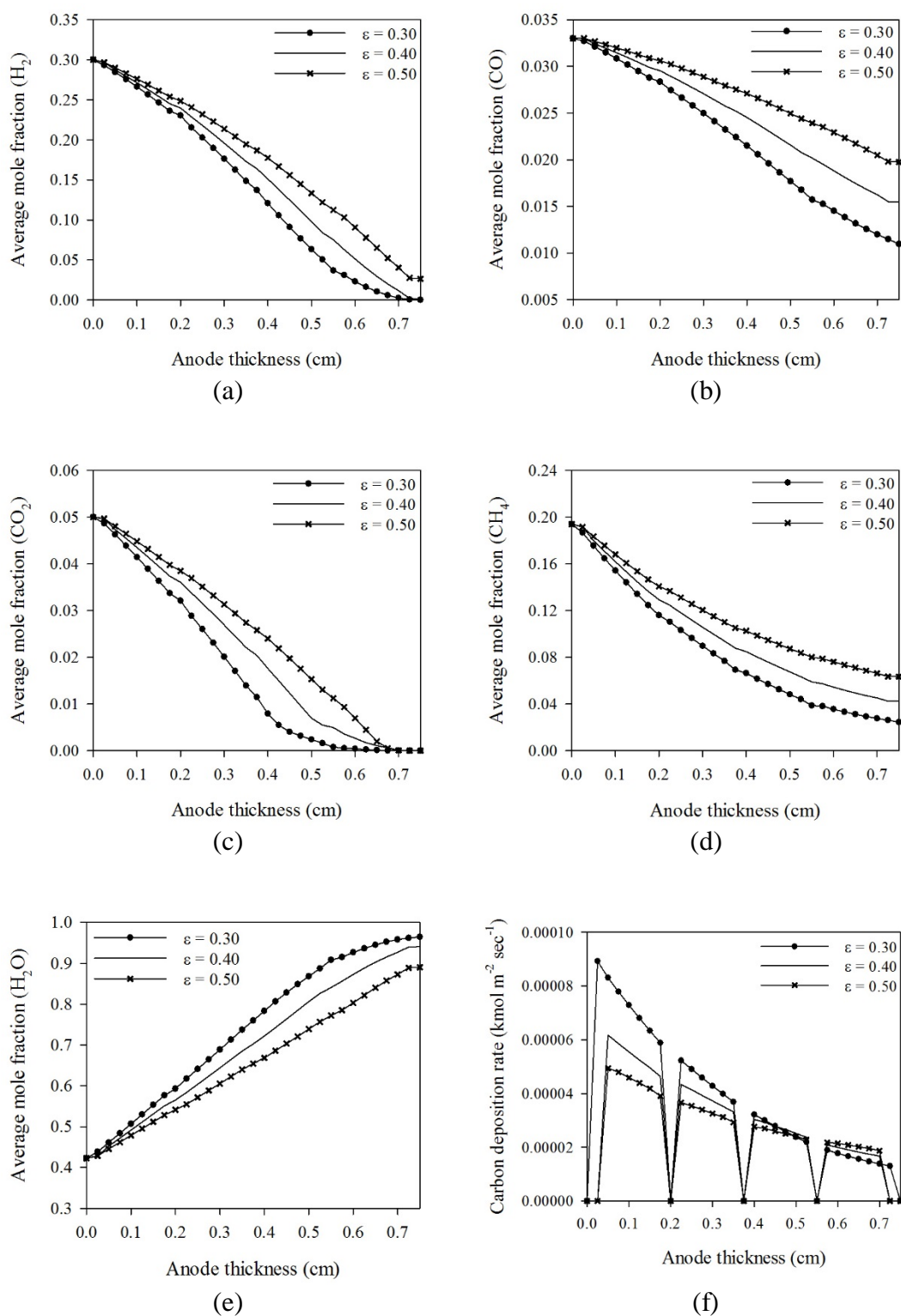


Figure 5.6 Average mole fraction of H_2 (a), CO (b), CO_2 (c), CH_4 (d), H_2O (e) and average carbon deposition rate along the anode thickness.

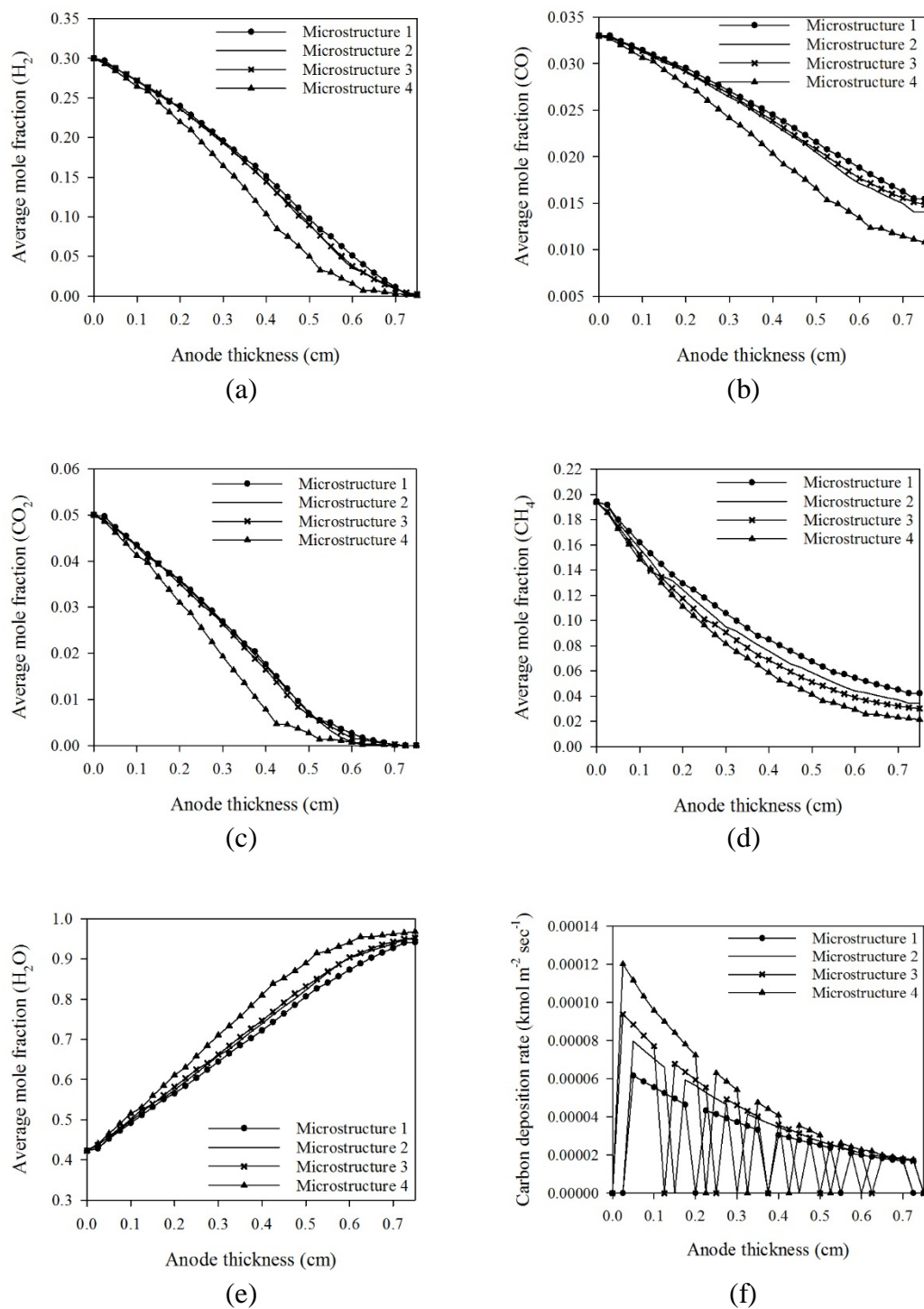


Figure 5.7 Average mole fraction of H₂ (a), CO (b), CO₂ (c), CH₄ (d), H₂O (e) and average carbon deposition rate (f) along the anode thickness

5.7 Conclusions

In this chapter, the CFD technique has been used for studying the multicomponent species transport and carbon deposition in the SOFC anode in order to study the effect of anode microstructure. Model anode geometries are considered in the similar fashion as previously used in literature. We have obtained results for mole fraction distribution and carbon deposition rate in the anode geometries for varying porosities and varying gas-solid interface areas. The main observations from this work are as follows: Firstly, it is observed that increasing the porosity in anode will lead to decrease in concentration polarisation and; there is no significant effect observed for the increase in gas-solid interface on the species distribution in the anode. Secondly, it is observed that the decrease in porosity and increase in gas-solid interface area increases the carbon deposition rate in the anode by providing more catalytic surface area for the reaction. This inverse behaviour of porosity and gas-solid interface area can be optimised for the minimum carbon deposition rate. The higher porosity at the inlet will give lower carbon deposition rates. Third, the model will enable us to test different anode microstructures and hence minimise the concentration polarisation in the anode. This model can further be developed for three-dimensional geometries of electrodes that will enable us to model more realistic microstructures. Such models will also be capable of handling other microstructural parameters such as tortuosity and volumetric triple phase boundary for the electrochemical reaction. Further, electron and ion transport can also be considered with such kind of models to minimise ohmic polarisation in the anode.

Chapter 6

Conclusion and future work

6.1 Conclusions

In this research work, we have used different approaches for microstructure investigations. Firstly, image analysis techniques were used to get the quantitative information of the anode microstructural properties. Segmentation of phases in a microscopic image is quite a challenging task. BSE imaging combined with EDS maps have been proposed to improve the segmentation of phases in the electronic image of Ni-YSZ anode. We have combined the EDS information with BSE images of the specimen to simplify the identification of phases in the sample. We have further illustrated the applicability of machine learning based algorithm to segment the image in individual phases through the TWS plugin available in Fiji. Image analysis and stereological relations have been used to extract the quantitative information of micro-structural properties from the processed images of the anode specimens.

Further, the effect of the nickel particle size on the microstructure properties of Ni-YSZ anode has been investigated using this image analysis technique. It has been observed that decrease in particle size of NiO powder also resulted in the decrease in size of YSZ phase and pore phase; and changed the anode microstructure, while the volumetric compositions of the components in the anode were kept constant. This was a very intriguing phenomenon and should be investigated further. We have observed that the interface area between phases increases linearly with particle sizes and the TPB density increases by a larger magnitude for a relatively smaller change in nickel particle size. This suggests that the use of smaller sized nickel oxide powder for the anode synthesis is beneficial for increasing the electrochemical active area, but at the same time it will result in decrease of pore size; inhibiting the transport of gaseous species and increasing the concentration polarisation.

We have used the analytical modelling approach for the investigation of microstructural parameters and degradation phenomenon effect on the microstructural properties. This model provides the way to quantify the microstructural properties with microstructural parameters and degradation

parameters (such as operation time and the amount of carbon deposited). It is observed that equal volume fraction, equal particle sizes and the possible smallest size of particles are preferred for the maximisation of the electrochemical active area while there is no degradation effect in the anode. However, the smaller particle sizes result into smaller pore sizes and must be optimised for concentration polarisation using the anode performance modelling. This microstructure model is further extended to study the effect of nickel coarsening and carbon deposition on the microstructural properties. This model suggests the use higher volume fraction (more than 50%) of nickel for obtaining a stable electrochemical active area while considering the effect of nickel coarsening phenomenon. Electrochemical area variation is minimum for 65% volume fraction of nickel particles. However, the higher volume fraction of nickel particle may result in structural stress due to the thermal coefficient mismatch of nickel and YSZ. This model should be further developed accounting for the structural stresses of particles induced due to different thermal expansion coefficients. In the study of microstructural properties variation with carbon deposition, it is observed that electrochemical active area is constant with 50% volume fraction of nickel particles. Nickel coarsening results in the increase of pore radius and carbon deposition results in the decrease of pore radius. The pore radius parameters with degradation parameters should be optimised using the anode performance modelling for the minimisation of concentration polarisation. Effective conductivity is found to increase with carbon deposition and decrease with nickel coarsening. This developed model gives us quantitative relationships between microstructural properties and degradation parameters that can be further included in anode performance modelling for obtaining optimised performance.

We have further demonstrated the use of CFD technique for the multicomponent species transport and carbon deposition in the anode to study the effect of anode microstructure. We have obtained results for the mole fraction distribution and carbon deposition rate in the model anode geometries for varying porosities and varying gas-solid interface area. It has been observed that increasing the porosity in anode will lead to decrease in the concentration polarisation. The concentration of reacting species H₂ is increased at electrochemical active boundary while porosity is increased from 30% to 50%. Species distribution has been observed to be prominently affected by the diffusion of species and not from the chemical reaction

inside anode. The increase in the gas-solid interphase area increases the reaction rate for carbon deposition but there is very slight difference in the distribution of species in the anode. Higher carbon deposition rates are observed near the inlet side of anode while the active surface area for carbon formation reaction is increased. It is suggested to maintain higher porosity and lower gas-solid interphase area at the inlet side of the anode to minimise the carbon deposition. This model will enable us to test different anode microstructures and hence minimise the concentration polarisation in the anode.

6.2 Recommendations for Future work

- The proposed BSE-SEM imaging with EDS mapping provides a convenient and comparatively simple experimental process that can be used with further proposed image segmentation methods for microstructure analysis. This technique can be used for the microstructure analysis after the cell operation and could help to quantify the microstructure degradation induced during cell operating due to several reasons such as catalyst poisoning, thermal stress etc. The proposed imaging methods and segmentation method can be further used for the three-dimensional imaging techniques (such as FIB-SEM). This technique can be further used for the microstructural properties evaluation of electrodes obtained using different synthesis methods and will provide the insights about the most suitable electrode microstructure and synthesis methods.
- We observed that the nickel particle inhibits the grain growth of the YSZ particle during sintering. This is very intriguing phenomenon and should be further explored to optimise microstructure and also to gain insight into the redox phenomenon which is a major performance degradation factor during cell operation.
- The proposed CFD simulation studies can be used for the designing of microstructure. This technique can be further developed for a more realistic microstructure of electrode and also extended for the 3D microstructures of the electrode. Such studies can provide insights about the structural degradation phenomena like catalyst poisoning on the performance.

References

1. Stambouli AB, Traversa E. Solid oxide fuel cells (SOFCs): a review of an environmentally clean and efficient source of energy. *Renewable and Sustainable Energy Reviews*. 2002;6(5):433-55.
2. McIntosh S, Gorte RJ. Direct Hydrocarbon Solid Oxide Fuel Cells. *Chemical Reviews*. 2004;104(10):4845-66.
3. Almutairi G. Ageing of Intergrated-Planar Solid Oxide Fuel Cells. Birmingham: University of Birmingham; 2013.
4. Bertei A, Nicoletta C. A comparative study and an extended theory of percolation for random packings of rigid spheres. *Powder Technology*. 2011;213(1):100-8.
5. Chen D, Lin Z, Zhu H, Kee RJ. Percolation theory to predict effective properties of solid oxide fuel-cell composite electrodes. *Journal of Power Sources*. 2009;191(2):240-52.
6. Singhal SC. Advances in solid oxide fuel cell technology. *Solid State Ionics*. 2000;135(1-4):305-13.
7. Sunde S. Simulations of Composite Electrodes in Fuel Cells. *Journal of Electroceramics*. 2000;5(2):153-82.
8. Sanyal J, Goldin GM, Zhu H, Kee RJ. A particle-based model for predicting the effective conductivities of composite electrodes. *Journal of Power Sources*. 2010;195(19):6671-9.
9. Grew KN, Chiu WKS. A review of modeling and simulation techniques across the length scales for the solid oxide fuel cell. *Journal of Power Sources*. 2012;199:1-13.
10. Timurkutluk B, Mat MD. A review on micro-level modeling of solid oxide fuel cells. *International Journal of Hydrogen Energy*. 2016;41(23):9968-81.
11. Bouvard D, Lange FF. Relation between percolation and particle coordination in binary powder mixtures. *Acta Metallurgica et Materialia*. 1991;39(12):3083-90.
12. Kuo C-H, Gupta PK. Rigidity and conductivity percolation thresholds in particulate composites. *Acta Metallurgica et Materialia*. 1995;43(1):397-403.
13. Chan SH, Xia ZT. Anode Micro Model of Solid Oxide Fuel Cell. *Journal of The Electrochemical Society*. 2001;148(4):A388-A94.

14. Costamagna P, Costa P, Antonucci V. Micro-modelling of solid oxide fuel cell electrodes. *Electrochimica Acta*. 1998;43(3–4):375-94.
15. Nam JH, Jeon DH. A comprehensive micro-scale model for transport and reaction in intermediate temperature solid oxide fuel cells. *Electrochimica Acta*. 2006;51(17):3446-60.
16. Suzuki M, Oshima T. Estimation of the Co-ordination number in a Multi-Component Mixture of Spheres. *Powder Technology*. 1983;35(2):159-66.
17. Broers GHJ, Treijtel BW. Carbon deposition boundaries and other constant parameter curves, in the triangular representation of C-H-O equilibria, with applications to fuel cells. *Advanced Energy Conversion*. 1965;5(4):365-82.
18. Chen D, Bi W, Kong W, Lin Z. Combined micro-scale and macro-scale modeling of the composite electrode of a solid oxide fuel cell. *Journal of Power Sources*. 2010;195(19):6598-610.
19. Chen D, Lu L, Li J, Yu Z, Kong W, Zhu H. Percolation micro-model to predict the effective properties of the composite electrode with poly-dispersed particle sizes. *Journal of Power Sources*. 2011;196(6):3178-85.
20. Farhad S, Hamdullahpur F. Micro-modeling of porous composite anodes for solid oxide fuel cells. *Aiche Journal*. 2012;58(6):1893-906.
21. Farhad S, Hamdullahpur F. Optimization of the microstructure of porous composite cathodes in solid oxide fuel cells. *Aiche Journal*. 2012;58(4):1248-61.
22. Chinda P. The Performance Improvement of a Thick Electrode Solid Oxide Fuel Cell. *Enrgy Proced*. 2013;34(0):243-61.
23. Kenney B, Valdmanis M, Baker C, Pharoah JG, Karan K. Computation of TPB length, surface area and pore size from numerical reconstruction of composite solid oxide fuel cell electrodes. *Journal of Power Sources*. 2009;189(2):1051-9.
24. Comiti J, Renaud M. A new model for determining mean structure parameters of fixed beds from pressure drop measurements: application to beds packed with parallelepipedal particles. *Chemical Engineering Science*. 1989;44(7):1539-45.
25. Sunde S. Calculation of Conductivity and Polarization Resistance of Composite SOFC Electrodes from Random Resistor Networks. *Journal of The Electrochemical Society*. 1995;142(4):L50-L2.

26. Sunde S. Monte Carlo Simulations of Conductivity of Composite Electrodes for Solid Oxide Fuel Cells. *Journal of The Electrochemical Society*. 1996;143(3):1123-32.
27. Sunde S. Monte Carlo Simulations of Polarization Resistance of Composite Electrodes for Solid Oxide Fuel Cells. *Journal of The Electrochemical Society*. 1996;143(6):1930-9.
28. Martin CL, Bouvard D, Shima S. Study of particle rearrangement during powder compaction by the Discrete Element Method. *Journal of the Mechanics and Physics of Solids*. 2003;51(4):667-93.
29. Nishida Y, Itoh S. A modeling study of porous composite microstructures for solid oxide fuel cell anodes. *Electrochimica Acta*. 2011;56(7):2792-800.
30. Dees DW, Claar TD, Easler TE, Fee DC, Mrazek FC. Conductivity of Porous Ni/ZrO₂-Y₂O₃ Cermets. *Journal of The Electrochemical Society*. 1987;134(9):2141-6.
31. Bennett CH. Serially Deposited Amorphous Aggregates of Hard Spheres. *Journal of Applied Physics*. 1972;43(6):2727-34.
32. Abel J, Kornyshev AA, Lehnert W. Correlated Resistor Network Study of Porous Solid Oxide Fuel Cell Anodes. *Journal of The Electrochemical Society*. 1997;144(12):4253-9.
33. Abbaspour A, Nandakumar K, Luo J, Chuang KT. A novel approach to study the structure versus performance relationship of SOFC electrodes. *Journal of Power Sources*. 2006;161(2):965-70.
34. Ali A, Wen X, Nandakumar K, Luo J, Chuang KT. Geometrical modeling of microstructure of solid oxide fuel cell composite electrodes. *Journal of Power Sources*. 2008;185(2):961-6.
35. Golbert J, Adjiman CS, Brandon NP. Microstructural Modeling of Solid Oxide Fuel Cell Anodes. *Industrial & Engineering Chemistry Research*. 2008;47(20):7693-9.
36. Lee JH, Moon H, Lee HW, Kim J, Kim JD, Yoon KH. Quantitative analysis of microstructure and its related electrical property of SOFC anode, Ni-YSZ cermet. *Solid State Ionics*. 2002;148(1-2):15-26.
37. Lee KR, Choi SH, Kim J, Lee HW, Lee JH. Viable image analysing method to characterize the microstructure and the properties of the Ni/YSZ cermet anode of SOFC. *Journal of Power Sources*. 2005;140(2):226-34.

38. Monachon C, Hessler-Wyser A, Faes A, Van Herle J, Tagliaferri E. Rapid Preparation and SEM Microstructural Characterization of Nickel–Yttria-Stabilized Zirconia Cermets. *Journal of the American Ceramic Society*. 2008;91(10):3405-7.
39. Thydén K, Liu YL, Bilde-Sørensen JB. Microstructural characterization of SOFC Ni–YSZ anode composites by low-voltage scanning electron microscopy. *Solid State Ionics*. 2008;178(39–40):1984-9.
40. Faes A, Hessler-Wyser A, Presvytes D, Vayenas CG, Van herle J. Nickel–Zirconia Anode Degradation and Triple Phase Boundary Quantification from Microstructural Analysis. *Fuel Cells*. 2009;9(6):841-51.
41. Lanzini A, Leone P, Asinari P. Microstructural characterization of solid oxide fuel cell electrodes by image analysis technique. *Journal of Power Sources*. 2009;194(1):408-22.
42. Wilson JR, Kobsiriphat W, Mendoza R, Chen H-Y, Hiller JM, Miller DJ, et al. Three-dimensional reconstruction of a solid-oxide fuel-cell anode. *Nat Mater*. 2006;5(7):541-4.
43. Wilson J, Kobsiriphat W, Mendoza R, Chen H-Y, Hines T, Hiller J, et al. Three Dimensional Reconstruction of Solid Oxide Fuel Cell Electrodes Using Focused Ion Beam - Scanning Electron Microscopy. *ECS Transactions*. 2007;7(1):1879-87.
44. Wilson JR, Duong AT, Gameiro M, Chen H-Y, Thornton K, Mumm DR, et al. Quantitative three-dimensional microstructure of a solid oxide fuel cell cathode. *Electrochemistry Communications*. 2009;11(5):1052-6.
45. Rüger B, Joos J, Weber A, Carraro T, Ivers-Tiffée E. 3D Electrode Microstructure Reconstruction and Modelling. *ECS Transactions*. 2009;25(2):1211-20.
46. Shearing PR, Golbert J, Chater RJ, Brandon NP. 3D reconstruction of SOFC anodes using a focused ion beam lift-out technique. *Chemical Engineering Science*. 2009;64(17):3928-33.
47. Shearing PR, Cai Q, Golbert JI, Yufit V, Adjiman CS, Brandon NP. Microstructural analysis of a solid oxide fuel cell anode using focused ion beam techniques coupled with electrochemical simulation. *Journal of Power Sources*. 2010;195(15):4804-10.

48. Shearing PR, Gelb J, Yi J, Lee WK, Drakopolous M, Brandon NP. Analysis of triple phase contact in Ni-YSZ microstructures using non-destructive X-ray tomography with synchrotron radiation. *Electrochemistry Communications*. 2010;12(8):1021-4.
49. Clague R, Shearing PR, Lee PD, Zhang Z, Brett DJL, Marquis AJ, et al. Stress analysis of solid oxide fuel cell anode microstructure reconstructed from focused ion beam tomography. *Journal of Power Sources*. 2011;196(21):9018-21.
50. Robinson JB, Brown LD, Jervis R, Taiwo OO, Heenan TMM, Millichamp J, et al. Investigating the effect of thermal gradients on stress in solid oxide fuel cell anodes using combined synchrotron radiation and thermal imaging. *Journal of Power Sources*. 2015;288:473-81.
51. Shikazono N, Kanno D, Matsuzaki K, Teshima H, Sumino S, Kasagi N. Numerical Assessment of SOFC Anode Polarization Based on Three-Dimensional Model Microstructure Reconstructed from FIB-SEM Images. *Journal of The Electrochemical Society*. 2010;157(5):B665-B72.
52. Iwai H, Shikazono N, Matsui T, Teshima H, Kishimoto M, Kishida R, et al. Quantification of SOFC anode microstructure based on dual beam FIB-SEM technique. *Journal of Power Sources*. 2010;195(4):955-61.
53. Vivet N, Chupin S, Estrade E, Piquero T, Pommier PL, Rochais D, et al. 3D Microstructural characterization of a solid oxide fuel cell anode reconstructed by focused ion beam tomography. *Journal of Power Sources*. 2011;196(18):7541-9.
54. Vivet N, Chupin S, Estrade E, Richard A, Bonnamy S, Rochais D, et al. Effect of Ni content in SOFC Ni-YSZ cermets: A three-dimensional study by FIB-SEM tomography. *Journal of Power Sources*. 2011;196(23):9989-97.
55. Holzer L, Münch B, Iwanschitz B, Cantoni M, Hocker T, Graule T. Quantitative relationships between composition, particle size, triple phase boundary length and surface area in nickel-cermet anodes for Solid Oxide Fuel Cells. *Journal of Power Sources*. 2011;196(17):7076-89.
56. Gunda NSK, Choi H-W, Berson A, Kenney B, Karan K, Pharoah JG, et al. Focused ion beam-scanning electron microscopy on solid-oxide fuel-cell electrode: Image analysis and computing effective transport properties. *Journal of Power Sources*. 2011;196(7):3592-603.
57. Kishimoto M, Iwai H, Saito M, Yoshida H. Quantitative evaluation of solid oxide fuel cell porous anode microstructure based on focused ion beam and scanning

electron microscope technique and prediction of anode overpotentials. *Journal of Power Sources*. 2011;196(10):4555-63.

58. Kwok K, Jørgensen PS, Frandsen HL, Wakai F. Computation of Effective Steady-State Creep of Porous Ni-YSZ Composites with Reconstructed Microstructures. *Journal of the American Ceramic Society*. 2015;98(9):2873-80.

59. Harris WM, Nelson GJ, Kiss AM, Izzo JR, Jr., Liu Y, Liu M, et al. Nondestructive volumetric 3-D chemical mapping of nickel-sulfur compounds at the nanoscale. *Nanoscale*. 2012;4(5):1557-60.

60. Kiss AM, Harris WM, Wang S, Vila-Comamala J, Deriy A, Chiu WKS. In-situ observation of nickel oxidation using synchrotron based full-field transmission X-ray microscopy. *Applied Physics Letters*. 2013;102(5):053902.

61. Nelson GJ, Harris WM, Jr. JRI, Grew KN, Chiu WKS, Chu YS, et al. Three-dimensional mapping of nickel oxidation states using full field x-ray absorption near edge structure nanotomography. *Applied Physics Letters*. 2011;98(17):173109.

62. Nelson GJ, Grew KN, Izzo JR, Lombardo JJ, Harris WM, Faes A, et al. Three-dimensional microstructural changes in the Ni-YSZ solid oxide fuel cell anode during operation. *Acta Materialia*. 2012;60(8):3491-500.

63. Harris WM, Lombardo JJ, Nelson GJ, Lai B, Wang S, Vila-Comamala J, et al. Three-dimensional microstructural imaging of sulfur poisoning-induced degradation in a Ni-YSZ anode of solid oxide fuel cells. *Sci Rep*. 2014;4:5246.

64. Liang B, Suzuki T, Hamamoto K, Yamaguchi T, Sumi H, Fujishiro Y, et al. Performance of Ni-Fe/gadolinium-doped CeO₂ anode supported tubular solid oxide fuel cells using steam reforming of methane. *Journal of Power Sources*. 2012;202(0):225-9.

65. Suzuki M, Oshima T. Estimation of the co-ordination number in a two-component mixture of cohesive spheres. *Powder Technology*. 1983;36(2):181-8.

66. Chan SH, Chen XJ, Khor KA. Cathode Micromodel of Solid Oxide Fuel Cell. *Journal of The Electrochemical Society*. 2004;151(1):A164-A72.

67. Gokhale AM, Zhang S, Liu M. A stochastic geometry based model for total triple phase boundary length in composite cathodes for solid oxide fuel cells. *Journal of Power Sources*. 2009;194(1):303-12.

68. Stauffer D, Aharony A. *Introduction to Percolation Theory*. 2nd ed. London: Taylor & Francis.; 1992 12 February 1992.

69. Liu L, Flesner R, Kim GY, Chandra A. Modeling of Solid Oxide Fuel Cells with Particle Size and Porosity Grading in Anode Electrode. *Fuel Cells*. 2012;12(1):97-108.
70. Divisek J, Wilkenhöner R, Volfkovich Y. Structure investigations of SOFC anode cermets Part I: Porosity investigations. *Journal of Applied Electrochemistry*. 1999;29(2):153-63.
71. Wilson JR, Cronin JS, Duong AT, Rukes S, Chen H-Y, Thornton K, et al. Effect of composition of (La_{0.8}Sr_{0.2}MnO₃-Y₂O₃-stabilized ZrO₂) cathodes: Correlating three-dimensional microstructure and polarization resistance. *Journal of Power Sources*. 2010;195(7):1829-40.
72. Chen DF, He HH, Zhang DH, Wang HZ, Ni M. Percolation Theory in Solid Oxide Fuel Cell Composite Electrodes with a Mixed Electronic and Ionic Conductor. *Energies*. 2013;6(3):1632-56.
73. Sharma A, Basu S. Study of Transient Behavior of Solid Oxide Fuel Cell Anode Degradation Using Percolation Theory. *Industrial & Engineering Chemistry Research*. 2014;53(51):19690-4.
74. Berson A, Choi H-W, Pharoah JG. Determination of the effective gas diffusivity of a porous composite medium from the three-dimensional reconstruction of its microstructure. *Physical Review E*. 2011;83(2):026310.
75. Wang G, Mukherjee PP, Wang C-Y. Direct numerical simulation (DNS) modeling of PEFC electrodes: Part II. Random microstructure. *Electrochimica Acta*. 2006;51(15):3151-60.
76. Zalc JM, Reyes SC, Iglesia E. The effects of diffusion mechanism and void structure on transport rates and tortuosity factors in complex porous structures. *Chemical Engineering Science*. 2004;59(14):2947-60.
77. Bertei A, Nucci B, Nicoletta C. Microstructural modeling for prediction of transport properties and electrochemical performance in SOFC composite electrodes. *Chemical Engineering Science*. 2013;101:175-90.
78. Bruggeman DAG. Berechnung verschiedener physikalischer Konstanten von heterogenen Substanzen. I. Dielektrizitätskonstanten und Leitfähigkeiten der Mischkörper aus isotropen Substanzen. *Annalen der Physik*. 1935;416(7):636-64.
79. Ruud JA, Striker T, Midha V, Ramamurthi BN, Linsebigler AL, Fogelman DJ. Microstructure-Performance Relationships in Lsm-Ysz Cathodes. 28th

International Conference on Advanced Ceramics and Composites A: Ceramic Engineering and Science Proceedings: John Wiley & Sons, Inc.; 2008. p. 251-6.

80. Wilson JR, Barnett SA. Solid Oxide Fuel Cell Ni-YSZ Anodes: Effect of Composition on Microstructure and Performance. *Electrochemical and Solid-State Letters*. 2008;11(10):B181-B5.

81. Janardhanan VM, Heuveline V, Deutschmann O. Three-phase boundary length in solid-oxide fuel cells: A mathematical model. *Journal of Power Sources*. 2008;178(1):368-72.

82. Costamagna P, Honegger K. Modeling of Solid Oxide Heat Exchanger Integrated Stacks and Simulation at High Fuel Utilization. *Journal of The Electrochemical Society*. 1998;145(11):3995-4007.

83. Jeon DH, Nam JH, Kim C-J. Microstructural Optimization of Anode-Supported Solid Oxide Fuel Cells by a Comprehensive Microscale Model. *Journal of The Electrochemical Society*. 2006;153(2):A406-A17.

84. Kang FR, Vogt FG, Brum J, Forcino R, Copley RCB, Williams G, et al. Effect of Particle Size and Morphology on the Dehydration Mechanism of a Non-Stoichiometric Hydrate. *Crystal Growth & Design*. 2012;12(1):60-74.

85. Simwonis D, Tietz F, Stöver D. Nickel coarsening in annealed Ni/8YSZ anode substrates for solid oxide fuel cells. *Solid State Ionics*. 2000;132(3-4):241-51.

86. Iliadis L, Jayne C. Engineering Applications of Neural Networks: 16th International Conference, EANN 2015, Rhodes, Greece, September 25-28 2015. Proceedings: Springer International Publishing; 2015.

87. Suzue Y, Shikazono N, Kasagi N. Micro modeling of solid oxide fuel cell anode based on stochastic reconstruction. *Journal of Power Sources*. 2008;184(1):52-9.

88. Yeong CLY, Torquato S. Reconstructing random media. II. Three-dimensional media from two-dimensional cuts. *Physical Review E*. 1998;58(1):224-33.

89. Bentz DP, Martys NS. Hydraulic radius and transport in reconstructed model three-dimensional porous media. *Transport in Porous Media*. 1994;17(3):221-38.

90. F. Zhao YJ, G.Y. Lin, A.V. Virkar, editor. Solid Oxide Fuel Cell VII (SOFC-VII); 2001; Paris: The Electrochemical Society.

91. Adler SB. Factors Governing Oxygen Reduction in Solid Oxide Fuel Cell Cathodes. *Chemical Reviews*. 2004;104(10):4791-844.

92. Tanner CW, Fung KZ, Virkar AV. The Effect of Porous Composite Electrode Structure on Solid Oxide Fuel Cell Performance: I. Theoretical Analysis. *Journal of The Electrochemical Society*. 1997;144(1):21-30.
93. Bieberle A, Meier LP, Gauckler LJ. The Electrochemistry of Ni Pattern Anodes Used as Solid Oxide Fuel Cell Model Electrodes. *Journal of The Electrochemical Society*. 2001;148(6):A646-A56.
94. Lee KT, Vito NJ, Wachsman ED. Comprehensive quantification of Ni–Gd_{0.1}Ce_{0.9}O_{1.95} anode functional layer microstructures by three-dimensional reconstruction using a FIB/SEM dual beam system. *Journal of Power Sources*. 2013;228:220-8.
95. Kishimoto M, Lomberg M, Ruiz-Trejo E, Brandon NP. Numerical modeling of nickel-infiltrated gadolinium-doped ceria electrodes reconstructed with focused ion beam tomography. *Electrochimica Acta*. 2016;190:178-85.
96. Izzo JR, Joshi AS, Grew KN, Chiu WKS, Tkachuk A, Wang SH, et al. Nondestructive Reconstruction and Analysis of SOFC Anodes Using X-ray Computed Tomography at Sub-50 nm Resolution. *Journal of The Electrochemical Society*. 2008;155(5):B504-B8.
97. Grew KN, Chu YS, Yi J, Peracchio AA, Izzo JR, Hwu Y, et al. Nondestructive Nanoscale 3D Elemental Mapping and Analysis of a Solid Oxide Fuel Cell Anode. *Journal of The Electrochemical Society*. 2010;157(6):B783-B92.
98. Nelson GJ, Harris WM, Lombardo JJ, Izzo Jr JR, Chiu WKS, Tanasini P, et al. Comparison of SOFC cathode microstructure quantified using X-ray nanotomography and focused ion beam–scanning electron microscopy. *Electrochemistry Communications*. 2011;13(6):586-9.
99. Dwivedi D, Lepkova K, Becker T. Emerging surface characterization techniques for carbon steel corrosion: a critical brief review. *Proc Math Phys Eng Sci*. 2017;473(2199):20160852.
100. Suzuki T, Hasan Z, Funahashi Y, Yamaguchi T, Fujishiro Y, Awano M. Impact of Anode Microstructure on Solid Oxide Fuel Cells. *Science*. 2009;325(5942):852-5.
101. Fu X, Xiang Y, Chen L, Xu X, Li X. A Novel Ni/YSZ Anode Image Segmentation Method for Solid Oxide Fuel Cell Electrodes Microstructure. *Fuel Cells*. 2016:n/a-n/a.

102. Wang W, Su C, Wu Y, Ran R, Shao Z. Progress in Solid Oxide Fuel Cells with Nickel-Based Anodes Operating on Methane and Related Fuels. *Chemical Reviews*. 2013;113(10):8104-51.
103. Park S, Vohs JM, Gorte RJ. Direct oxidation of hydrocarbons in a solid-oxide fuel cell. *Nature*. 2000;404(6775):265-7.
104. Gür TM. Comprehensive review of methane conversion in solid oxide fuel cells: Prospects for efficient electricity generation from natural gas. *Progress in Energy and Combustion Science*. 2016;54:1-64.
105. Lanzini A, Ferrero D, Papurello D, Santarelli M. Reporting Degradation from Different Fuel Contaminants in Ni-anode SOFCs. *Fuel Cells*. 2017
106. Irvine JTS, Neagu D, Verbraeken MC, Chatzichristodoulou C, Graves C, Mogensen MB. Evolution of the electrochemical interface in high-temperature fuel cells and electrolyzers. 2016;1:15014.
107. McIntosh S, He H, Lee S-I, Costa-Nunes O, Krishnan VV, Vohs JM, et al. An Examination of Carbonaceous Deposits in Direct-Utilization SOFC Anodes. *Journal of The Electrochemical Society*. 2004;151(4):A604-A8.
108. Yurkiv V. Reformate-operated SOFC anode performance and degradation considering solid carbon formation: A modeling and simulation study. *Electrochimica Acta*. 2014;143:114-28.
109. Xiao J, Xie Y, Liu J, Liu M. Deactivation of nickel-based anode in solid oxide fuel cells operated on carbon-containing fuels. *Journal of Power Sources*. 2014;268:508-16.
110. Sehested J. Four challenges for nickel steam-reforming catalysts. *Catalysis Today*. 2006;111(1-2):103-10.
111. He H, Hill JM. Carbon deposition on Ni/YSZ composites exposed to humidified methane. *Applied Catalysis A: General*. 2007;317(2):284-92.
112. Chen G, Guan G, Abliz S, Kasai Y, Abudula A. Rapid degradation phenomenon of NiCu-Ce_{0.8}Gd_{0.2}O_{1.9} anode at high p(H₂O) in different concentrations of dry methane. *Electrochimica Acta*. 2011;56(27):9868-74.
113. Sumi H, Puengjinda P, Muroyama H, Matsui T, Eguchi K. Effects of crystal Structure of yttria- and scandia-stabilized zirconia in nickel-based SOFC anodes on carbon deposition and oxidation behavior. *Journal of Power Sources*. 2011;196(15):6048-54.

114. Xu J, Froment GF. Methane steam reforming, methanation and water-gas shift: I. Intrinsic kinetics. *AIChE Journal*. 1989;35(1):88-96.
115. Zhang Y, Yang Z, Wang M. Understanding on the carbon deposition on the Nickel/Yttrium–Stabilized Zirconia anode caused by the CO containing fuels. *Journal of Power Sources*. 2015;279:759-65.
116. Koh J-H, Yoo Y-S, Park J-W, Lim HC. Carbon deposition and cell performance of Ni-YSZ anode support SOFC with methane fuel. *Solid State Ionics*. 2002;149(3–4):157-66.
117. Yan M, Zeng M, Chen Q, Wang Q. Numerical study on carbon deposition of SOFC with unsteady state variation of porosity. *Applied Energy*. 2012;97(0):754-62.
118. Xu H, Dang Z. Lattice Boltzmann modeling of carbon deposition in porous anode of a solid oxide fuel cell with internal reforming. *Applied Energy*. 2016;178:294-307.
119. Sasaki K, Teraoka Y. Equilibria in Fuel Cell Gases: II. The C-H-O Ternary Diagrams. *Journal of The Electrochemical Society*. 2003;150(7):A885-A8.
120. Sasaki K, Teraoka Y. Equilibria in Fuel Cell Gases: I. Equilibrium Compositions and Reforming Conditions. *Journal of The Electrochemical Society*. 2003;150(7):A878-A84.
121. Laosiripojana N, Assabumrungrat S. Catalytic steam reforming of methane, methanol, and ethanol over Ni/YSZ: The possible use of these fuels in internal reforming SOFC. *Journal of Power Sources*. 2007;163(2):943-51.
122. Singh D, Hernández-Pacheco E, Hutton PN, Patel N, Mann MD. Carbon deposition in an SOFC fueled by tar-laden biomass gas: a thermodynamic analysis. *Journal of Power Sources*. 2005;142(1–2):194-9.
123. Nikooyeh K, Clemmer R, Alzate-Restrepo V, Hill JM. Effect of hydrogen on carbon formation on Ni/YSZ composites exposed to methane. *Applied Catalysis A: General*. 2008;347(1):106-11.
124. Wang W, Ran R, Su C, Guo Y, Farrusseng D, Shao Z. Ammonia-mediated suppression of coke formation in direct-methane solid oxide fuel cells with nickel-based anodes. *Journal of Power Sources*. 2013;240:232-40.
125. Kim H, Park S, Vohs JM, Gorte RJ. Direct Oxidation of Liquid Fuels in a Solid Oxide Fuel Cell. *Journal of The Electrochemical Society*. 2001;148(7):A693-A5.

126. Takeguchi T, Kani Y, Yano T, Kikuchi R, Eguchi K, Tsujimoto K, et al. Study on steam reforming of CH₄ and C₂ hydrocarbons and carbon deposition on Ni-YSZ cermets. *Journal of Power Sources*. 2002;112(2):588-95.
127. Maček J, Novosel B, Marinšek M. Ni-YSZ SOFC anodes—Minimization of carbon deposition. *Journal of the European Ceramic Society*. 2007;27(2–3):487-91.
128. Jiao Y, Zhang L, An W, Zhou W, Sha Y, Shao Z, et al. Controlled deposition and utilization of carbon on Ni-YSZ anodes of SOFCs operating on dry methane. *Energy*. 2016;113:432-43.
129. Lin Y, Zhan Z, Liu J, Barnett SA. Direct operation of solid oxide fuel cells with methane fuel. *Solid State Ionics*. 2005;176(23):1827-35.
130. Horita T, Yamaji K, Kato T, Kishimoto H, Xiong Y, Sakai N, et al. Imaging of CH₄ decomposition around the Ni/YSZ interfaces under anodic polarization. *Journal of Power Sources*. 2005;145(2):133-8.
131. Giddey S, Badwal SPS, Kulkarni A, Munnings C. A comprehensive review of direct carbon fuel cell technology. *Progress in Energy and Combustion Science*. 2012;38(3):360-99.
132. Li C, Shi Y, Cai N. Mechanism for carbon direct electrochemical reactions in a solid oxide electrolyte direct carbon fuel cell. *Journal of Power Sources*. 2011;196(2):754-63.
133. Chen T, Wang WG, Miao H, Li T, Xu C. Evaluation of carbon deposition behavior on the nickel/yttrium-stabilized zirconia anode-supported fuel cell fueled with simulated syngas. *Journal of Power Sources*. 2011;196(5):2461-8.
134. Alzate-Restrepo V, Hill JM. Carbon deposition on Ni/YSZ anodes exposed to CO/H₂ feeds. *Journal of Power Sources*. 2010;195(5):1344-51.
135. Lu X, Tjaden B, Bertei A, Li T, Li K, Brett D, et al. 3D Characterization of Diffusivities and Its Impact on Mass Flux and Concentration Overpotential in SOFC Anode. *Journal of The Electrochemical Society*. 2017;164(4):F188-F95.
136. Chan SH, Khor KA, Xia ZT. A complete polarization model of a solid oxide fuel cell and its sensitivity to the change of cell component thickness. *Journal of Power Sources*. 2001;93(1–2):130-40.
137. Hussain MM, Li X, Dincer I. Mathematical modeling of transport phenomena in porous SOFC anodes. *International Journal of Thermal Sciences*. 2007;46(1):48-56.

138. Paradis H, Andersson M, Sundén B. Modeling of mass and charge transport in a solid oxide fuel cell anode structure by a 3D lattice Boltzmann approach. *Heat and Mass Transfer*. 2016;52(8):1529-40.
139. Joshi AS, Grew KN, Peracchio AA, Chiu WKS. Lattice Boltzmann modeling of 2D gas transport in a solid oxide fuel cell anode. *Journal of Power Sources*. 2007;164(2):631-8.
140. Chiu WKS, Joshi AS, Grew KN. Lattice Boltzmann model for multi-component mass transfer in a solid oxide fuel cell anode with heterogeneous internal reformation and electrochemistry. *The European Physical Journal Special Topics*. 2009;171(1):159-65.
141. Guo P, Guan Y, Liu G, Liang Z, Liu J, Zhang X, et al. Modeling of gas transport with electrochemical reaction in nickel-yttria-stabilized zirconia anode during thermal cycling by Lattice Boltzmann method. *Journal of Power Sources*. 2016;327:127-34.
142. Espinoza-Andaluz M, Andersson M, Sundén B. Modeling of a Gradient Porosity SOFC Anode using the Lattice Boltzmann Method. *Energy Procedia*. 2017;105:1332-8.
143. Autissier N, Larrain D, Van herle J, Favrat D. CFD simulation tool for solid oxide fuel cells. *Journal of Power Sources*. 2004;131(1–2):313-9.
144. Janardhanan VM, Deutschmann O. CFD analysis of a solid oxide fuel cell with internal reforming: Coupled interactions of transport, heterogeneous catalysis and electrochemical processes. *Journal of Power Sources*. 2006;162(2):1192-202.
145. Danilov VA, Tade MO. A CFD-based model of a planar SOFC for anode flow field design. *International Journal of Hydrogen Energy*. 2009;34(21):8998-9006.
146. Qu Z, Aravind PV, Boksteen SZ, Dekker NJJ, Janssen AHH, Woudstra N, et al. Three-dimensional computational fluid dynamics modeling of anode-supported planar SOFC. *International Journal of Hydrogen Energy*. 2011;36(16):10209-20.
147. Razbani O, Assadi M, Andersson M. Three dimensional CFD modeling and experimental validation of an electrolyte supported solid oxide fuel cell fed with methane-free biogas. *International Journal of Hydrogen Energy*. 2013;38(24):10068-80.

148. Pianko-Oprych P, Zinko T, Jaworski Z. Three-Dimensional Computational Fluid Dynamics Modelling for a Planar Solid Oxide Fuel Cell of a New Design. *ECS Transactions*. 2015;68(1):3013-23.
149. Ni M. Modeling and parametric simulations of solid oxide fuel cells with methane carbon dioxide reforming. *Energy Conversion and Management*. 2013;70:116-29.
150. Hosseini S, Ahmed K, Tadé MO. CFD model of a methane fuelled single cell SOFC stack for analysing the combined effects of macro/micro structural parameters. *Journal of Power Sources*. 2013;234(0):180-96.
151. Shri Prakash B, Senthil Kumar S, Aruna ST. Properties and development of Ni/YSZ as an anode material in solid oxide fuel cell: A review. *Renewable and Sustainable Energy Reviews*. 2014;36(0):149-79.
152. Zhu WZ, Deevi SC. A review on the status of anode materials for solid oxide fuel cells. *Materials Science and Engineering: A*. 2003;362(1–2):228-39.
153. Pihlatie M, Kaiser A, Larsen PH, Mogensen M. Dimensional Behavior of Ni–YSZ Composites during Redox Cycling. *Journal of The Electrochemical Society*. 2009;156(3):B322-B9.
154. Kong J, Sun K, Zhou D, Zhang N, Mu J, Qiao J. Ni–YSZ gradient anodes for anode-supported SOFCs. *Journal of Power Sources*. 2007;166(2):337-42.
155. Primdahl S, Sørensen BF, Mogensen M. Effect of Nickel Oxide/Yttria-Stabilized Zirconia Anode Precursor Sintering Temperature on the Properties of Solid Oxide Fuel Cells. *Journal of the American Ceramic Society*. 2000;83(3):489-94.
156. Fukui T, Ohara S, Naito M, Nogi K. Performance and stability of SOFC anode fabricated from NiO–YSZ composite particles. *Journal of Power Sources*. 2002;110(1):91-5.
157. Schindelin J, Arganda-Carreras I, Frise E, Kaynig V, Longair M, Pietzsch T, et al. Fiji: an open-source platform for biological-image analysis. *Nat Meth*. 2012;9(7):676-82.
158. Russ JC, Neal FB. *Image Processing Handbook, Sixth Edition* 2011.
159. Ignacio Arganda-Carreras VK, Curtis Rueden, Kevin W. Eliceiri, Johannes Schindelin, Albert Cardona, H. Sebastian Seung. Trainable Weka Segmentation: a machine learning tool for microscopy pixel classification. *Bioinformatics*. 2017;btx180.

160. Joos J, Ender M, Rotscholl I, Menzler NH, Ivers-Tiffée E. Quantification of double-layer Ni/YSZ fuel cell anodes from focused ion beam tomography data. *Journal of Power Sources*. 2014;246:819-30.
161. Wang Y, Lin CL, Miller JD. Improved 3D image segmentation for X-ray tomographic analysis of packed particle beds. *Minerals Engineering*. 2015;83:185-91.
162. Joos J, Carraro T, Weber A, Ivers-Tiffée E. Reconstruction of porous electrodes by FIB/SEM for detailed microstructure modeling. *Journal of Power Sources*. 2011;196(17):7302-7.
163. G. B, H. I, Y. O, M. S, H. Y, S. SJ. Local Evolution of Triple Phase Boundary in Solid Oxide Fuel Cell Stack After Long-term Operation. *Fuel Cells*. 2015;15(3):545-8.
164. Mújica-Vargas D, Gallegos-Funes FJ, Rosales-Silva AJ. A fuzzy clustering algorithm with spatial robust estimation constraint for noisy color image segmentation. *Pattern Recognition Letters*. 2013;34(4):400-13.
165. Underwood EE. Quantitative Stereology for Microstructural Analysis. In: McCall JL, Mueller WM, editors. *Microstructural Analysis: Tools and Techniques*. Boston, MA: Springer US; 1973. p. 35-66.
166. Doube M, Klosowski MM, Arganda-Carreras I, Cordelières FP, Dougherty RP, Jackson JS, et al. BoneJ: Free and extensible bone image analysis in ImageJ. *Bone*. 2010;47(6):1076-9.
167. Hildebrand T, Rüegsegger P. A new method for the model-independent assessment of thickness in three-dimensional images. *Journal of Microscopy*. 1997;185(1):67-75.
168. Francus P, Pirard E. Testing for Sources of Errors in Quantitative Image Analysis. In: Francus P, editor. *Image Analysis, Sediments and Paleoenvironments*. Dordrecht: Springer Netherlands; 2004. p. 87-102.
169. Mukhtar NZF, Borhan Z, Rusop M, Abdullah S. Effect of Milling Time on Particle Size and Surface Morphology of Commercial Zeolite by Planetary Ball Mill 2013. 711-5 p.
170. Kano J, Saito F. Correlation of powder characteristics of talc during Planetary Ball Milling with the impact energy of the balls simulated by the Particle Element Method. *Powder Technology*. 1998;98(2):166-70.

171. Xue Q. The influence of particle shape and size on electric conductivity of metal–polymer composites. *European Polymer Journal*. 2004;40(2):323-7.
172. Yu JH, Park GW, Lee S, Woo SK. Microstructural effects on the electrical and mechanical properties of Ni–YSZ cermet for SOFC anode. *Journal of Power Sources*. 2007;163(2):926-32.
173. He WD, Zou J, Wang B, Vilayurganapathy S, Zhou M, Lin X, et al. Gas transport in porous electrodes of solid oxide fuel cells: A review on diffusion and diffusivity measurement. *Journal of Power Sources*. 2013;237:64-73.
174. Lanzini A, Guerra C, Leone P, Santarelli M, Smeacetto F, Fiorilli S, et al. Influence of the microstructure on the catalytic properties of SOFC anodes under dry reforming of methane. *Materials Letters*. 2016;164:312-5.
175. Wilson JR, Cronin JS, Barnett SA. Linking the microstructure, performance and durability of Ni-yttria-stabilized zirconia solid oxide fuel cell anodes using three-dimensional focused ion beam–scanning electron microscopy imaging. *Scripta Materialia*. 2011;65(2):67-72.
176. Holzer L, Iwanschitz B, Hocker T, Münch B, Prestat M, Wiedenmann D, et al. Microstructure degradation of cermet anodes for solid oxide fuel cells: Quantification of nickel grain growth in dry and in humid atmospheres. *Journal of Power Sources*. 2011;196(3):1279-94.
177. Merk HJ. The macroscopic equations for simultaneous heat and mass transfer in isotropic, continuous and closed systems. *Applied Scientific Research, Section A*. 1959;8(1):73-99.
178. Fuller EN, Schettler PD, Giddings JC. New method for prediction of binary gas phase diffusion coefficients. *Industrial & Engineering Chemistry*. 1966;58(5):18-27.
179. Ahmed K, Foger K. Kinetics of internal steam reforming of methane on Ni/YSZ-based anodes for solid oxide fuel cells. *Catalysis Today*. 2000;63(2–4):479-87.
180. Haberman BA, Young JB. Three-dimensional simulation of chemically reacting gas flows in the porous support structure of an integrated-planar solid oxide fuel cell. *International Journal of Heat and Mass Transfer*. 2004;47(17):3617-29.
181. Akhtar N, Decent SP, Kendall K. Numerical modelling of methane-powered micro-tubular, single-chamber solid oxide fuel cell. *Journal of Power Sources*. 2010;195(23):7796-807.

182. Zavarukhin SG, Kuvshinov GG. The kinetic model of formation of nanofibrous carbon from CH₄-H₂ mixture over a high-loaded nickel catalyst with consideration for the catalyst deactivation. *Applied Catalysis A: General*. 2004;272(1):219-27.

183. Snoeck JW, Froment GF, Fowles M. Steam/CO₂ Reforming of Methane. Carbon Filament Formation by the Boudouard Reaction and Gasification by CO₂, by H₂, and by Steam: Kinetic Study. *Industrial & Engineering Chemistry Research*. 2002;41(17):4252-65.

Every reasonable effort has been made to acknowledge the owners of copyright material. I would be pleased to hear from any copyright owner who has been omitted or incorrectly acknowledged.

Appendices

Appendix A

Permission of reproduction from the copyright owner

12/14/2017

RightsLink Printable License

AMERICAN PHYSICAL SOCIETY LICENSE TERMS AND CONDITIONS

Dec 14, 2017

This Agreement between Shambhu Singh Rathore ("You") and American Physical Society ("American Physical Society") consists of your license details and the terms and conditions provided by American Physical Society and Copyright Clearance Center.

License Number	4247680364770
License date	Dec 14, 2017
Licensed Content Publisher	American Physical Society
Licensed Content Publication	Physical Review E
Licensed Content Title	Determination of the effective gas diffusivity of a porous composite medium from the three-dimensional reconstruction of its microstructure
Licensed Content Author	Arganthaël Berson, Hae-Won Choi, and Jon G. Pharoah
Licensed Content Date	Feb 24, 2011
Licensed Content Volume	83
Type of Use	Thesis/Dissertation
Requestor type	Student
Format	Print, Electronic
Portion	chart/graph/table/figure
Number of charts/graphs/tables/figures	1
Portion description	FIG. 1
Rights for	Main product
Duration of use	Life of Current Edition
Creation of copies for the disabled	no
With minor editing privileges	no
For distribution to	Worldwide
In the following language(s)	Original language of publication
With incidental promotional use	no
The lifetime unit quantity of new product	0 to 499
The requesting person/organization is:	Shambhu Singh Rathore
Order reference number	
Title of your thesis / dissertation	Investigation of microstructural and carbon deposition effects in SOFC anodes through modeling and experiments
Expected completion date	Jan 2018
Expected size (number of pages)	160
Requestor Location	Shambhu Singh Rathore 1/9 CallanClose, Waterford Western Australia Perth, WA 6152

<https://s100.copyright.com/AppDispatchServlet>

1/3

**ELSEVIER LICENSE
TERMS AND CONDITIONS**

Dec 14, 2017

This Agreement between Shambhu Singh Rathore ("You") and Elsevier ("Elsevier") consists of your license details and the terms and conditions provided by Elsevier and Copyright Clearance Center.

License Number	4247690980360
License date	Dec 14, 2017
Licensed Content Publisher	Elsevier
Licensed Content Publication	Journal of Power Sources
Licensed Content Title	Viable image analyzing method to characterize the microstructure and the properties of the Ni/YSZ cermet anode of SOFC
Licensed Content Author	K.-R. Lee,S.H. Choi,J. Kim,H.-W. Lee,J.-H. Lee
Licensed Content Date	Feb 2, 2005
Licensed Content Volume	140
Licensed Content Issue	2
Licensed Content Pages	9
Start Page	226
End Page	234
Type of Use	reuse in a thesis/dissertation
Intended publisher of new work	other
Portion	figures/tables/illustrations
Number of figures/tables/illustrations	1
Format	both print and electronic
Are you the author of this Elsevier article?	No
Will you be translating?	No
Original figure numbers	Fig. 3
Title of your thesis/dissertation	Investigation of microstructural and carbon deposition effects in SOFC anodes through modeling and experiments
Expected completion date	Jan 2018
Estimated size (number of pages)	160
Requestor Location	Shambhu Singh Rathore 1/9 CallanClose, Waterford Western Australia Perth, WA 6152 Australia Attn:
Total	0.00 USD
Terms and Conditions	

INTRODUCTION

1. The publisher for this copyrighted material is Elsevier. By clicking "accept" in connection with completing this licensing transaction, you agree that the following terms and conditions

**ELSEVIER LICENSE
TERMS AND CONDITIONS**

Dec 06, 2017

This Agreement between Shambhu Singh Rathore ("You") and Elsevier ("Elsevier") consists of your license details and the terms and conditions provided by Elsevier and Copyright Clearance Center.

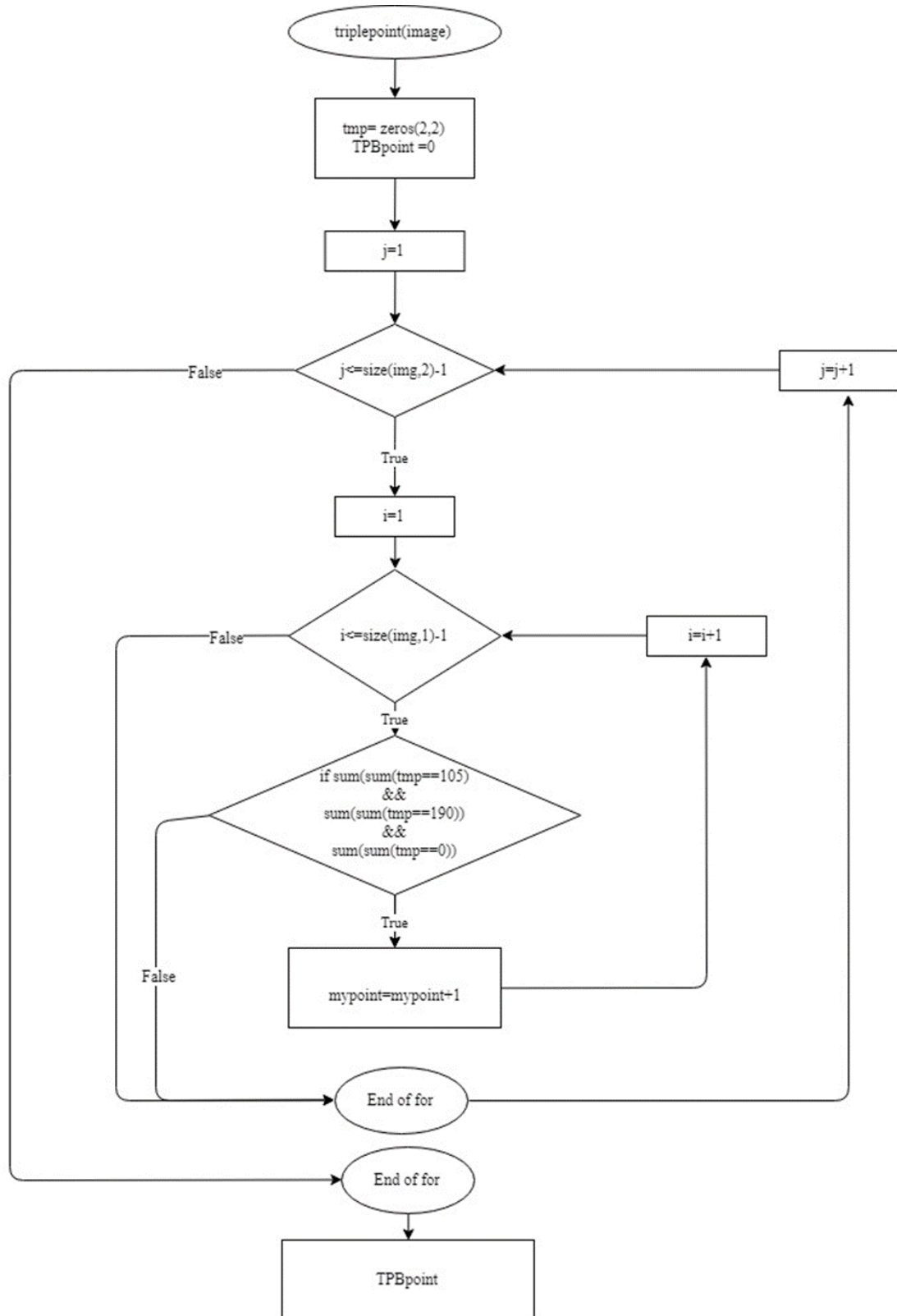
License Number	4243090747745
License date	Dec 06, 2017
Licensed Content Publisher	Elsevier
Licensed Content Publication	Journal of Power Sources
Licensed Content Title	Evaluation of carbon deposition behavior on the nickel/yttrium-stabilized zirconia anode-supported fuel cell fueled with simulated syngas
Licensed Content Author	Tao Chen,Wei Guo Wang,He Miao,Tingshuai Li,Cheng Xu
Licensed Content Date	Mar 1, 2011
Licensed Content Volume	196
Licensed Content Issue	5
Licensed Content Pages	8
Start Page	2461
End Page	2468
Type of Use	reuse in a thesis/dissertation
Portion	figures/tables/illustrations
Number of figures/tables/illustrations	1
Format	both print and electronic
Are you the author of this Elsevier article?	No
Will you be translating?	No
Original figure numbers	Figure 10
Title of your thesis/dissertation	Investigation of microstructural and carbon deposition effects in SOFC anodes through modeling and experiments
Expected completion date	Jan 2018
Estimated size (number of pages)	160
Requestor Location	Shambhu Singh Rathore 1/9 CallanClose, Waterford Western Australia Perth, WA 6152 Australia Attn:
Total	0.00 USD
Terms and Conditions	

INTRODUCTION

1. The publisher for this copyrighted material is Elsevier. By clicking "accept" in connection with completing this licensing transaction, you agree that the following terms and conditions apply to this transaction (along with the Billing and Payment terms and conditions

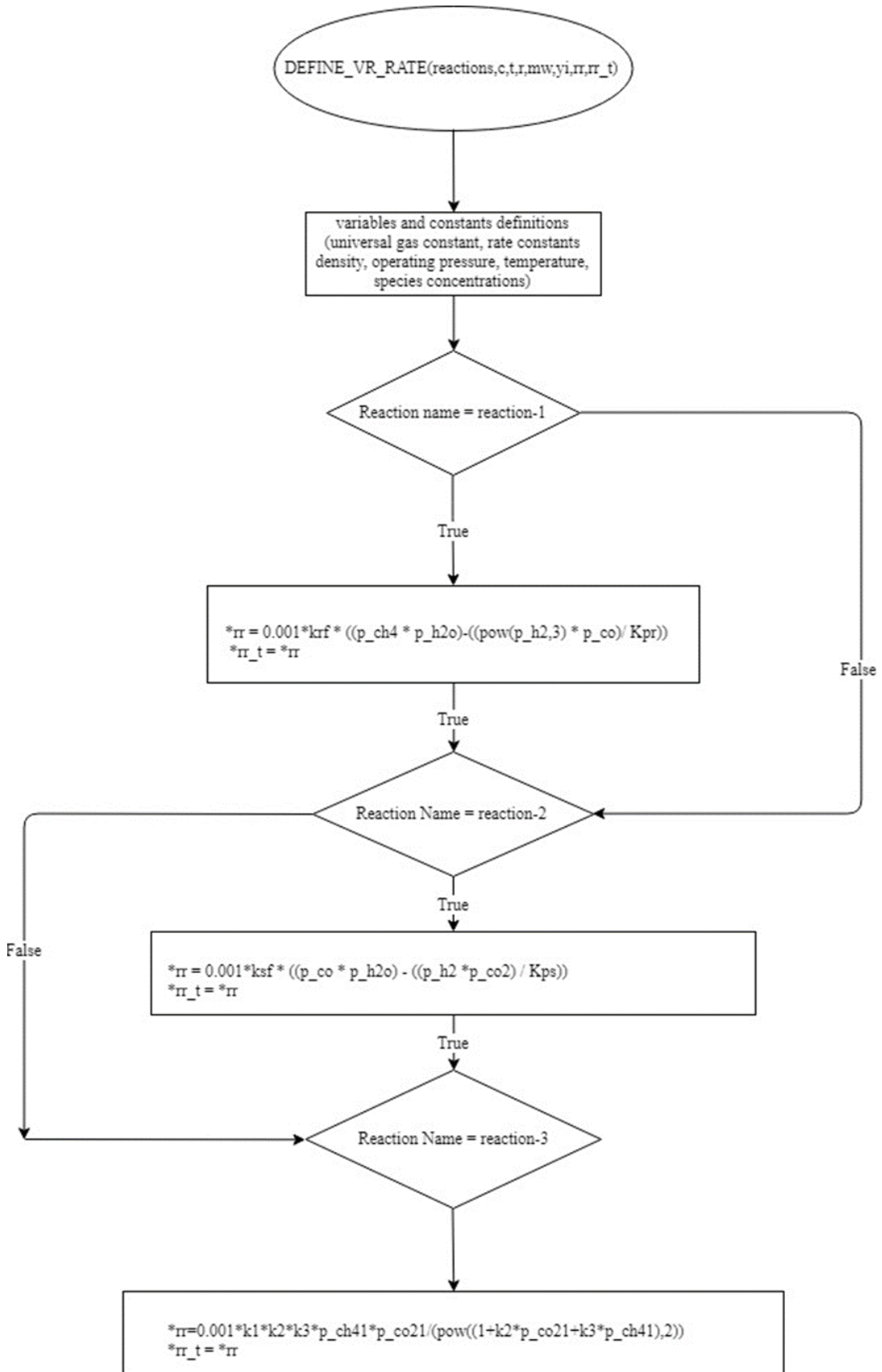
Appendix B

Flowchart for triple phase boundary points calculation code:



Appendix C

Flowchart for user-defined functions of volumetric reaction rates in Fluent:



Appendix D

Flowchart for user-defined functions of surface reaction rates in Fluent:

